Chapter 5

Tornadoes and Tornadic Storms

ROBERT DAVIES-JONES

National Severe Storms Laboratory, NOAA, Norman, Oklahoma

R. JEFFREY TRAPP

National Severe Storms Laboratory, NOAA, Norman, Oklahoma, and Cooperative Institute for Mesoscale Meteorological Studies, University of Oklahoma, Norman, Oklahoma

HOWARD B. BLUESTEIN

School of Meteorology, University of Oklahoma, Norman, Oklahoma

REVIEW PANEL: John T. Snow (Chair), Eugene W. McCaul Jr., Joseph H. Golden, Jean Dessens, Richard Peterson, and W. S. Lewellen

5.1. Introduction

a. Definitions

Tornadoes, with measured wind speeds of 125 m s^{-1} to perhaps 140 m s^{-1}, are the most violent of atmospheric storms (Fig. 5.1). A tornado is defined here as a violently rotating, narrow column of air, averaging about 100 m in diameter, that extends to the ground from the interior of a cumulonimbus (or occasionally a cumulus congestus) cloud and appears as a condensation funnel pendant from cloud base and/or as a swirling cloud of dust and debris rising from the ground. Significant damage can occur at the ground even when the condensation funnel does not reach the surface. A condensation funnel associated with a tornadic vortex that fails to contact the ground is called a *funnel cloud.* A waterspout is a tornado over a body of water.

Tornadoes can be divided into two types. A *type I* tornado forms within a mesocyclone, a larger-scale parent circulation. To a first approximation, the tangential winds in a mesocyclone may be modeled as a Rankine combined vortex, which consists of a core in solid-body rotation surrounded by a potential vortex where the tangential wind is inversely proportional to distance from the center of circulation. Core diameters vary from 3 to 9 km, with an average value around 5 km. The parent storm of a type I tornado can be an isolated supercell storm (Fig. 5.2), a supercell in a line of thunderstorms (Browning 1986), or a miniature supercell containing a small mesocyclone (Davies 1993b; Kennedy et al. 1993). Large and violent tornadoes almost invariably fall into this class. Tornadoes within minisupercells in rainbands of landfalling tropical cyclones (e.g., McCaul 1993; Novlan and Gray 1974) are also type I.

For the purposes of this review, a *supercell* is defined as a long-lived (> 1 h) thunderstorm with a high degree of spatial correlation between its mesocyclone and updraft. All supercells produce their overall most significant tornadoes under or very near the wall cloud (Moller 1978) (Fig. 5.3); other less significant tornadoes form along the rear-flank downdraft gust front. Supercell storms may be visually (and also by radar) generalized as follows, according to the position and extent of heavy rain relative to the storm's main updraft: low precipitation (LP), "classic" (or moderate precipitation), and high (or heavy) precipitation (HP) (Doswell and Burgess 1993; see also Rasmussen and Straka 1998). As can be inferred from the discussions in sections 5.2 and 5.3, the relatively higher propensity of a classic supercell to become tornadic is determined somewhat by the storm organization implied by this classification. Nevertheless, even LP supercells (Burgess and Davies-Jones 1979; Bluestein and Parks 1983; Bluestein and Woodall 1990) produce tornadoes (Bluestein and MacGorman 1998), even though it is not expected that there will be any significant evaporatively cooled pool of air near the ground (Fig. 5.4).

A *type II* tornado is not associated with a mesocirculation. It is generally a small and weak vortex that forms along a stationary or slowly moving windshift line, from the rolling-up of the associated vortex sheet into individual vortices (Barcilon and Drazin 1972; Davies-Jones and Kessler 1974). In the case of a "landspout" (Bluestein 1985a) for example, the wind-

FIG. 5.1. Tornado at Osnabrock, North Dakota, on 24 July 1978 as seen looking NE. The eastward-moving tornado passed one-half mile to the north of the photographer. Note the cloud band spiralling inward and cyclonically around the tornado from the east. Copyright photo by Edi Ann Otto, permission granted for scientific use.

shift line precedes the tornado's parent cloud. A "gustnado" (Bluestein 1980) is a type II vortex that forms along the storm's internally generated outflow boundary well away from any mesocyclone. Lack of a vigorous parent updraft superimposed over the outflow boundary usually precludes it from intensifying into a strong tornado. It is visible near the ground as a dust whirl and sometimes at cloud base as a small rotating eddy or a short condensation funnel. Cold-air funnels are spawned during daytime by high-based, low-topped, moderate thunderstorms that form in deep, cold-core synoptic-scale lows (Cooley 1978). These funnel clouds are long, slender, and ropelike. Occasionally they reach the ground and cause light damage. High-based funnels (e.g., Bluestein 1994) and vortices embedded within synoptic-scale fronts (Carbone 1983) can probably also be categorized as type II tornadoes.

b. Climatological distribution of tornadoes

Tornadoes occur worldwide, but are most prevalent in the Great Plains of the United States and in northeast India–Bangladesh, which are both areas that lie to the east of a mountain range and poleward of a warm ocean (see Fujita 1973). Based on data in the United States from 1921 to 1995 (see Grazulis 1993), the maximum in the mean number of days per century of F2 intensity (based on the Fujita scale; Fujita 1981) or greater tornado occurrence is located in southcentral Oklahoma (Fig. 5.5). This spatial distribution, in conjunction with an annual consistency in the seasonal distribution of such significant tornado occurrence, suggests a "Tornado Alley" that extends from north Texas northward into western Iowa (Concannon et al. 2000).

Over the past 50 years, the annual number of all tornadoes reported in the United States has increased from approximately 200 to 1200. This increase is unlikely to be physical; rather, it reflects an overall increase in population density, improved reporting procedures, and organized networks of "storm spotters," etc. (e.g., Doswell et al. 1999); there is currently no evidence to suggest that the threat from significant tornadoes is increasing due to global climate change (e.g., Concannon et al. 2000). Contemporary tornado verification data can still be problematic, though. Tornado formation times, in particular, may contain errors of as much as 1 h, for a variety of nonmeteorological reasons (Witt et al. 1998). The reported tornado inten-

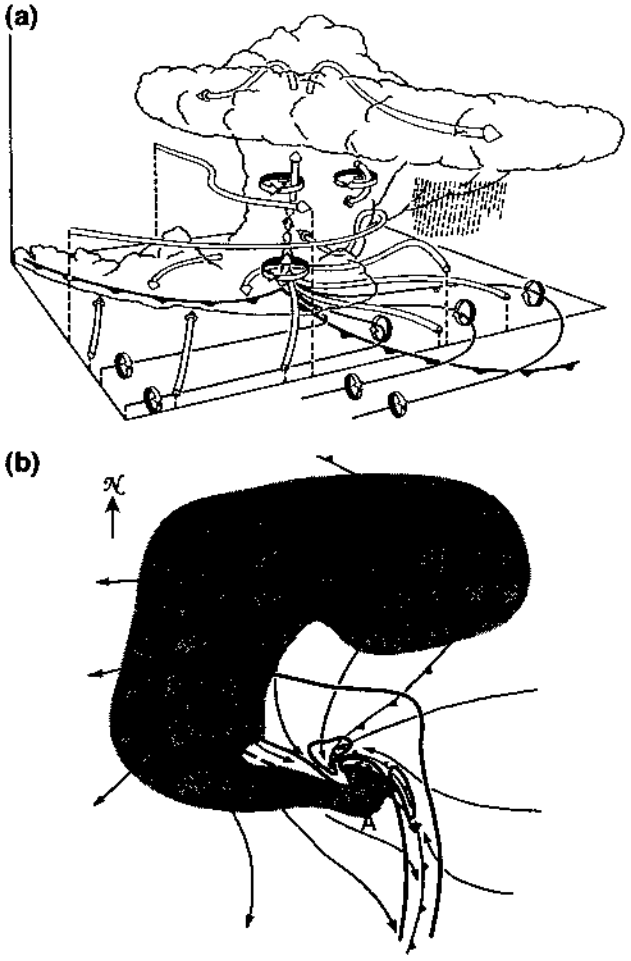

FIG. 5.2. (a) Three-dimensional schematic view from the southeast of a supercell thunderstorm in environmental winds that veer with height. The cylindrical arrows depict the flow in and around the storm. The thick lines show some of the vortex lines, with the sense of rotation indicated by the circular-ribbon arrows. The heavy barbed line marks the boundary of the cool-air outflow beneath the storm. From Klemp (1987; reprinted with permission). (b) Schematic flow field at 250 m above the ground in a tornadic supercell. The radar echo is indicated by the stippling. Vertical velocity is contoured at 2 m s^{-1} intervals with zero contour omitted and negative contour dashed. Note the storm-scale rear-flank downdraft west of the updraft and the occlusion downdraft near the vorticity maximum. The pseudo–cold front is drawn where the temperature is 1 K cooler than the environment. The flow arrows depict storm-relative surface streamlines. The T marks the location of the vertical vorticity maximum and cyclonic tornado, and A indicates where a rare anticyclonic tornado might occur. In time the secondary updraft maximum on the bulge in the gust front becomes dominant and a new mesocyclone forms in its vicinity as the storm-relative flow pattern shifts southward. From Klemp and Rotunno (1983).

sity is based primarily on a description of damage intensity as it appears to non-engineers. Each category (F0 to F5 in ascending order of severity) has been assigned a range of wind speeds without rigorous justification. Engineers can reliably estimate the minimum wind speeds required to account for observed damage only if structures of known structural integrity are damaged.

In contrast to the tornado-reporting trend, Fig. 5.6 shows that the annual, population-normalized death toll due to tornadoes in the United States has declined steadily since 1925 (Doswell et al. 1999). The decline since 1950 can be attributed to improved public awareness and education, the issuance of severe-weather warnings and watches, vast improvements in forecasting and dissemination of information to the public, and the identification of dangerous storms on radar and by trained spotters in the field. Operational use of the most current operational radar, the Weather Surveillance Radar-1988 Doppler (WSR-88D), can be linked to the current mean tornado-warning lead time of 13 min, a 5-min improvement over warnings issued prior to the installation of the WSR-88D network (Bieringer and Ray 1996). Better warnings and watches are of course also related to a greater scientific understanding of tornadoes and tornadic storms, the focus of the remainder of this chapter.

Since tornadoes and tornadic storms have been well reviewed in the past 30 years, we will not reiterate excellent descriptions that are available elsewhere. For background material the reader is referred to individual review articles by Morton (1966), Davies-Jones and Kessler (1974), Snow (1982, 1984), Rotunno (1986), Klemp (1987), and Davies-Jones (1995), and to many papers in the books edited by Peterson (1976), Kessler (1986), and Church et al. (1993). Other chapters in this monograph also touch on various aspects of tornadoes, particularly the one by Wilhelmson and Wicker on numerical simulations of severe storms.

Morton (1966) states that the "study of tornado vortices may be separated into two parts: mechanisms for the generation of an enhanced level of vorticity in some neighborhood of a thunderstorm, and the development of an actual vortex from this background." We believe that this statement is still generally valid and so reflect it in the organization of sections 5.2 and 5.3. We then examine, in sections 5.4–5.6, the observed and modeled flow structure of tornadoes to show how these vortices, once well established, are stable and intense. The chapter concludes with comments on some of the unsolved problems/unanswered questions and technological needs of this field of study. Our discussions hereafter apply to Northern Hemisphere storms, but carry over to Southern Hemisphere ones with the appropriate modifications (interchange left and right, north and south, clockwise and counterclockwise).

5.2. Midlevel and near-ground mesocyclogenesis

We separate our discussions of midlevel (5-km altitude, nominally) and near-ground mesocyclogenesis according to the respective processes by which vertical vorticity on the mesocyclone scale is generated. At midlevels, the mesocyclone develops initially

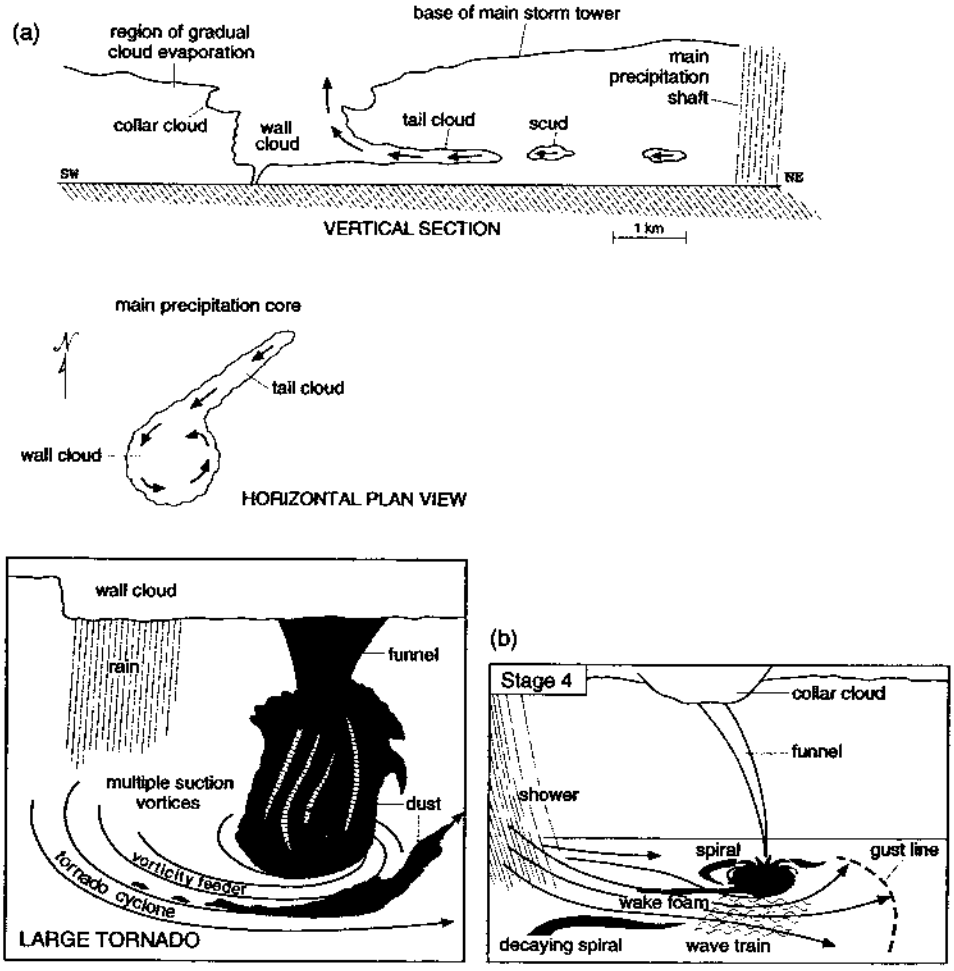

FIG. 5.3. Diagrams showing relationship of nearby rain shaft and cloud features to (a) tornado (based on Fujita 1959 and from Fujita et al. 1976), and (b) waterspout (based on Golden 1974a).

from the tilting of the horizontal vorticity associated with the vertical shear of the environmental winds. The theoretical basis for this statement is derived below from the linearized and then fully nonlinear equations of motion. Near the ground, the mesocyclone may form due to the tilting of horizontal vorticity generated within low-level density gradients. Barotropic processes may also play a role in near-ground mesocyclogenesis, and hence they are also treated below. Before venturing into this and other explanations, however, we will first review the observations of mesocyclones, which motivate the theory.

a. Mesocyclone observations

The mesocyclone observations presented below result in some way from informal and formally organized storm-intercept endeavors (e.g., Browning 1964; Donaldson and Lamkin 1964; Agee 1969, 1970; Golden and Morgan 1972; Moller et al. 1974; Golden and Purcell 1978b; Moller 1978; Bluestein 1980; Davies-Jones 1983; Bluestein 1984; Bluestein 1985a; Bluestein 1986; Bluestein and Golden 1993; Rasmussen et al. 1994; Bluestein 1996; Bluestein 1999a,b).

Visual evidence of rotation in the updraft portion (labeled "main storm tower" in Fig. 5.4) of cumulonimbus clouds is given particularly well by time-lapse photography. Complementary evidence is provided by Doppler radar data, which represent mesocyclones as range-constant and azimuthally adjacent regions of inbound and outbound Doppler velocities (in the direction of the radar beam, the speed of precipitation particles and other radar targets), whose peaks are azimuthally separated. Objective mesocyclone identification criteria, first established by Donaldson (1970) (who is also responsible for the first observation of a mesocyclone by Doppler radar; see Donaldson 1990), consist now in U.S. National Weather Service (NWS) operations of Doppler velocity shear ≥ 6 m s^{-1} km^{-1} and a differential velocity ≥ 30 m s^{-1} (both applicable within ranges ≤ 100 km, and thereafter reduced by

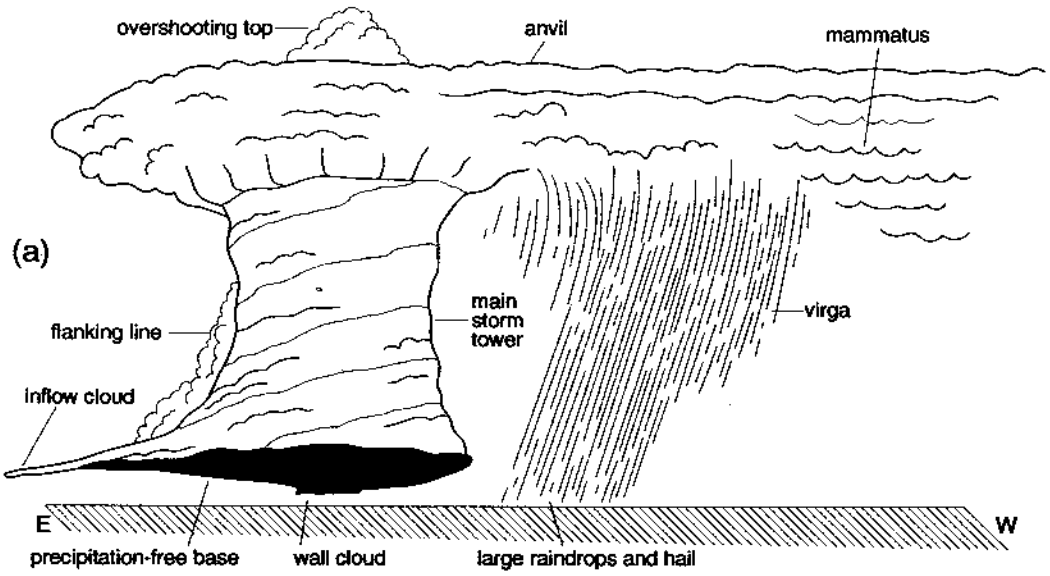

(b)

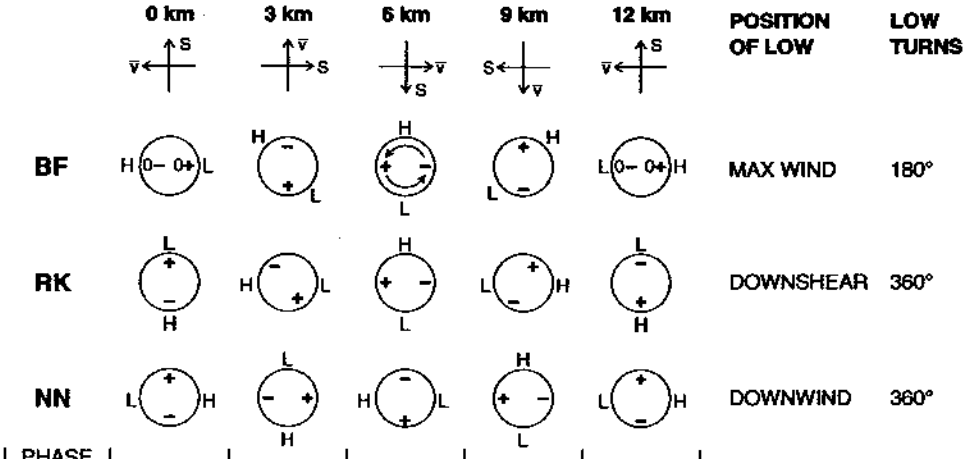

PHASE DIFF						
RKBF	90°	45°	0°	45°	90°	+ CORRELATION
NNBF	180°	135°	90°	45°	0°	NO CORRELATION

BF - Beltrami Flow
RK - Rotunno and Klemp (1982)
NN - Newton and Newton (1959)

FIG. 5.4. (a) Depiction of how a low-precipitation supercell storm might look in an environment with a circle hodograph. The entire updraft rotates in this case. (b) Schematic showing the positions of the high (H) and lows (L) of the linear pressure and of the associated maximum upward (+) and downward (−) VPPGF, as functions of height from the surface (0 km) to storm top (12 km) according to the exact Beltrami flow solution (BF) and to the Rotunno and Klemp (RK) and Newton and Newton (NN) models. The circle depicts axisymmetric updraft, which is rotating as a whole at midlevels (curved arrows). Outlined H and L (in RK) and 0+ and 0− (in BF) indicate positions of extrema just inside the domain in cases where the quantity vanishes on the boundary. Arrows give environmental wind and shear at each level. Also tabulated for each model are the phase errors, position of the low relative to wind features, and the angle through which the low turns. The nonlinear pressure has only one low in this case and it is at the midpoint of the updraft. From Davies-Jones (1985, 1996b).

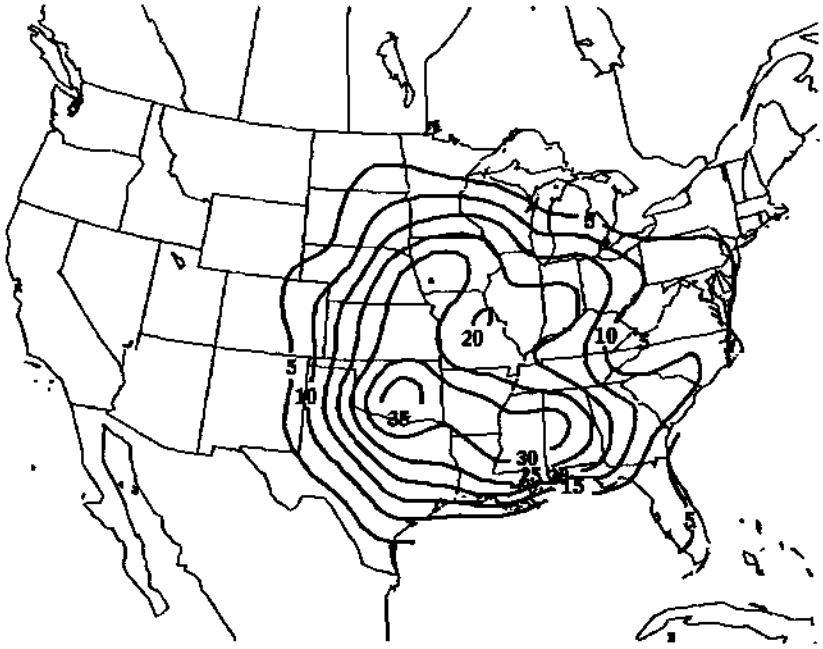

FIG. 5.5. Based on data from 1921 to 1995, the mean number of days per century of F2 intensity or greater tornado occurrence within 40km of a point in the United States (Concannon et al. 2000). Contour interval is 5 days, with minimum level equal to 5.

some percentage), met over a depth $\geq$ 3 km and with a base at altitudes $\leq$ 5 km above radar level, and persisting longer than 5–6 min (more than one radar volume scan). Some form of these criteria—with complementary visual observations and poststorm surveys—has been used to establish the oft-cited statistic that only 50% (or 25%, based on more recent work) of all objectively defined mesocyclones are associated with tornadoes (e.g., Burgess and Lemon 1990). The implication here—that mesocyclone detection leads to only a modest probability of tornado detection—serves as the impetus for the continued work on automated algorithmic identification of specific attributes of those mesocyclones most likely to spawn tornadoes (e.g., Stumpf et al. 1998).

Dual- or multiple-Doppler radar observations, from which the 3D wind may be retrieved, confirm the vortical structure of mesocyclones (the existence of a vortex may only be inferred from single Doppler radar). Analyses of such observations (Brandes 1977; Heymsfield 1978; Brandes 1978; Ray et al. 1980, 1981; Brandes 1981; 1984a,b; Hane and Ray 1985; Johnson et al. 1987; Brandes et al. 1988; Ray and Stephenson 1990; Wakimoto et al. 1996; Dowell et al. 1997; Dowell and Bluestein 1997; Bluestein et al. 1997; Wakimoto et al. 1998; Wakimoto and Liu 1998; Trapp 1999) additionally confirm/expand on kinematical relationships among the updraft, downdraft, and mesocyclone that are described below. Computed from the analyses is the mesocyclonic vertical vorticity scale of 0.01 s^{-1}, a benchmark value in many regards. The mesocyclonic vertical vorticity exhibits a vertical variability that depends on the stage in the supercell storm life cycle: Early (late) in the life of a supercell, the vertical vorticity is greatest aloft (near the ground). Indeed, we note the particularly relevant observation by Brandes (1984b) of a "low-level multiplicative growth of vertical vorticity" that coincides with the tornadic-stage transition; this characteristic motivates in part the consideration of different mechanisms for midlevel and near-ground mesocyclogenesis, which we are now ready to pursue.

b. Linear theory of initial midlevel rotation

The origins of the initial rotation of supercell updrafts at low to midlevels can be deduced from the linear Boussinesq equations for dry inviscid motion applied to an isolated growing convective cell in a sheared unstably stratified environment (Lilly 1982; Davies-Jones 1984). The cell is modeled as an exponentially amplifying disturbance with an axisymmetric buoyancy field or "thermal plume"; the linearity assumption in the governing equations is valid only when the disturbance amplitude is small. Perturbations owing to the disturbance are relative to a basic state that represents the undisturbed environment. A perturbation variable of key importance in the approach due to Davies-Jones (1984) is the vertical displacement $h'(x, y, z, t)$ of air parcels in the disturbance, which also describes the perturbed height of isentropic surfaces and vortex lines, which are horizontal initially at

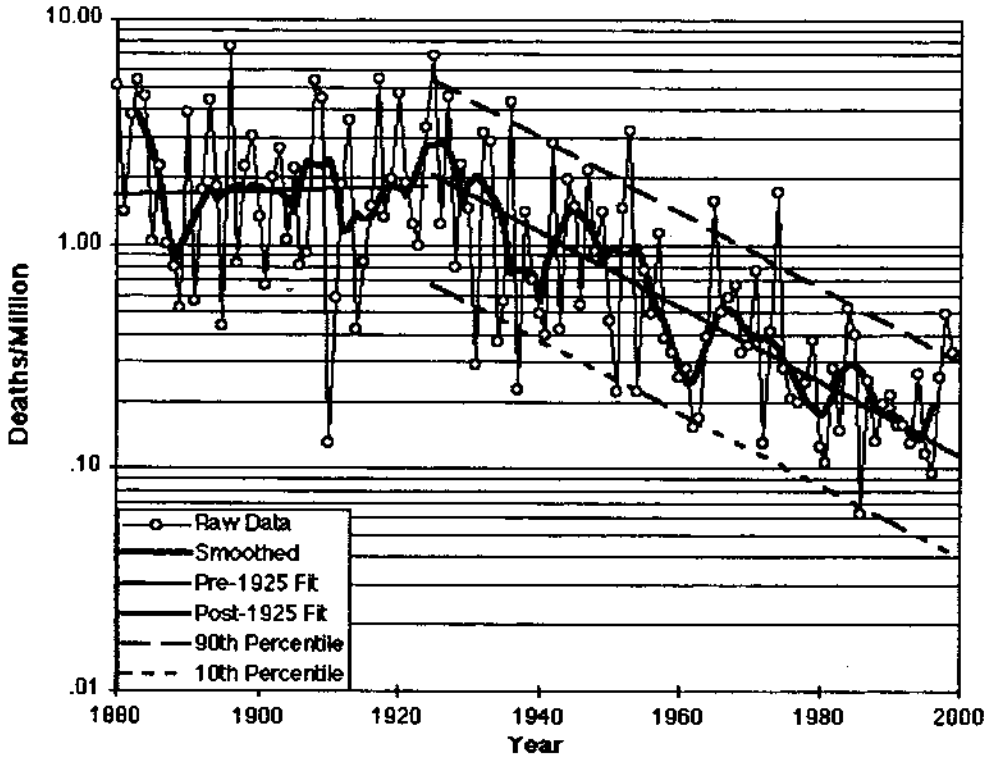

FIG. 5.6. Population-normalized annual death toll due to tornadoes in the United States (Doswell et al. 1999).

all levels (see below). The vertical displacement is important because it is proportional to buoyancy and is related to vertical velocity and vertical vorticity via simple expressions.

Since the horizontal vorticity associated with vertical shear is often 50 times greater than the large-scale background vertical vorticity associated with the earth's rotation and midlatitude cyclones, Coriolis terms can be safely omitted, and we can assume that the velocity and potential temperature of the environment (basic state) are of the form $\bar{\mathbf{v}}(z) \equiv (\bar{u}(z), \bar{v}(z), 0)$ and $\bar{\theta}(z)$ (where z is height). The environmental shear and vorticity are given by $\bar{\mathbf{S}}(z) \equiv (\bar{S}_1, \bar{S}_2) \equiv (\bar{u}_z, \bar{v}_z, 0)$ and $\bar{\boldsymbol{\omega}}(z) \equiv \nabla \times \bar{\mathbf{v}}(z) = (-\bar{v}_z, \bar{u}_z, 0)$. Note that the environmental vorticity has the same magnitude as the shear and is directed 90° to the left of it. Furthermore, the potential vorticity (PV), $\alpha\boldsymbol{\omega} \cdot \nabla\theta$, is zero in the environment. Since potential vorticity is conserved following a parcel in the absence of turbulent mixing and diabatic heating or cooling, the potential vorticity is constrained to remain zero throughout the flow.

According to the linear theory, vertical vorticity is generated solely via the upward tilting of environmental vorticity. Our interest here is in applying the theory to explain initiation of cyclonically rotating updrafts in sheared environmental flow, or, specifically, how perturbation vertical velocity (w') and vertical vorticity (ζ') become positively correlated through the tilting of environmental vortex lines. The concept of *streamwise* versus *crosswise* vorticity is indispensable for this purpose: The streamwise (crosswise) vorticity component is parallel (normal) to the local storm-relative velocity vector, and accounts for the storm-relative directional (speed) shear.

The derivation by Davies-Jones (1984) yields the following approximate formula for the theoretical correlation coefficient r between w' and ζ':

$$r = \frac{\langle \zeta' w' \rangle}{[\langle \zeta'^2 \rangle \langle w'^2 \rangle]^{1/2}} \approx \frac{|\bar{\mathbf{v}} - \mathbf{c}|}{\sqrt{\sigma^2 D^2 + |\bar{\mathbf{v}} - \mathbf{c}|^2}} \frac{\bar{\omega}_s}{|\bar{\boldsymbol{\omega}}|} \quad (5.1)$$

where angular brackets denote a surface integral, D (~3 km) is the length scale of the horizontal gradients associated with the disturbance, σ is the exponential growth rate of the disturbance (~3×10^{-3} s^{-1}), $\mathbf{c}$ is the disturbance- or "storm"-motion vector, and $\bar{\omega}_s$ denotes the streamwise component of the environmental vorticity vector. Equation (5.1) demonstrates that the correlation is high when the environmental vorticity is predominantly streamwise and storm-relative winds are of order σD (~10 m s^{-1}) or greater so that the advective timescale $D/|\bar{\mathbf{v}} - \mathbf{c}|$ is comparable to the growth timescale $1/\sigma$.

A qualitative explanation for the development of this correlation can be provided in terms of isentropic surfaces (Fig. 5.7). Since the potential vorticity remains zero, the vortex lines are embedded in these

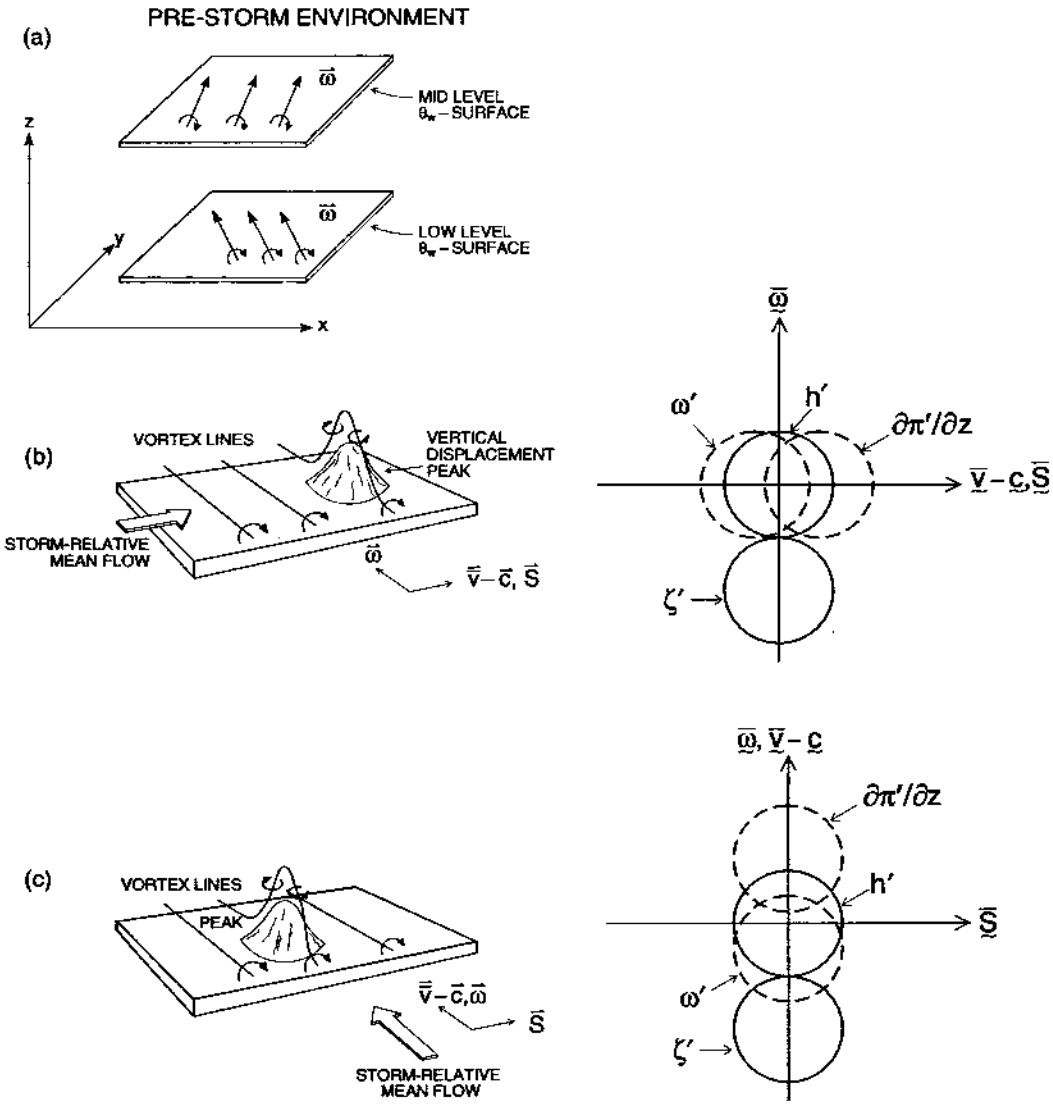

FIG. 5.7. Linear barotropic effect on vortex lines of a small, amplifying, isolated, axisymmetric peak (vertical displacement maximum) in an isentropic surface, as observed in a storm-relative reference frame (in which the peak does not translate and all winds are storm relative). In the horizontally homogeneous prestorm environment, depicted in (a), the isentropic surfaces and vorticity vectors are horizontal. The peak pulls up loops of vortex lines (shown slightly above, instead of in, the surface for clarity), giving rise to cyclonic (anticyclonic) vorticity on the right (left) side of the shear vector $\bar{\mathbf{S}}$ drawn through the peak. The environmental flow over the peak displaces the maximum updraft to the upstream side of the peak owing to the upslope flow there. In (b) the winds $\bar{\mathbf{v}} - \mathbf{c}$ increase with height without veering or backing so that the environmental vorticity $\bar{\boldsymbol{\omega}}$ is purely crosswise, i.e., perpendicular to the flow. In this case the cyclonic (anticyclonic) vortex is on the right (left) side of the flow, resulting in no net updraft rotation. In (c) the winds $\bar{\mathbf{v}} - \mathbf{c}$ veer with height without changing speed so that $\bar{\boldsymbol{\omega}}$ is purely streamwise, i.e., aligned with the flow. In this case, the cyclonic vortex is on the upslope side of the peak, resulting in positive correlation between vertical velocity and vertical vorticity. The schematic diagrams on the right illustrate the linear theory relationships among vertical displacement h', vertical velocity w', vertical vorticity ζ', and vertical perturbation pressure gradient $\partial\pi'/\partial z$ in the two extreme cases. The centers of the circles indicate the relative positions of the maxima. In all cases, the maximum updraft is on the upstream side of the peak in h', the maximum $\partial\pi'/\partial z$ is on the downstream side, and the cyclonic vorticity maximum is on the right side (relative to $\bar{\mathbf{S}}$). Overlapping, touching, or disjointed circles signify positive, zero, or negative correlation between the two variables involved. Note, however, that the correlation between w' and $\partial\pi'/\partial z$ becomes negative at high storm-relative wind speed. Adapted from Davies-Jones (1984).

surfaces. Let us consider a particular surface that is deformed from its initial flat shape by the convection. A developing isolated convective cell raises a growing peak in this surface. The storm-relative wind advects the vortex lines over the peak, and the resulting tilting of vortex lines produces a cyclonic (anticyclonic) vortex to the right (left) of the peak, looking downshear. If the vorticity is crosswise, the flow is upslope on the upshear side of the peak, so the updraft does not rotate as a whole. If the vorticity is streamwise, the relative flow is from right to left and the upslope side is the cyclonic side. The updraft rotates cyclonically as a whole because the vorticity is along the streamlines and is tilted upward as the air enters the updraft. The anticyclonic vortex on the downstream side of the peak is either in downdraft or in less intense updraft.

The relative locations of the maxima of h', w', ζ', and the vertical perturbation pressure-gradient force (VPPGF; $\partial\pi'/\partial z$) in a given level for a growing convective cell can be deduced from linear theory (Fig. 5.7). Recall that the h' field is coincident with the buoyancy field b'. Looking downshear, the cyclonic and anticyclonic vortices lie on the right and left side of the buoyancy peak, within buoyancy gradients (Figs. 5.7b,c), so that ζ' is uncorrelated with b' (Davies-Jones 1984; Kanak and Lilly 1996). In the storm's reference frame the maximum updraft is upstream of this peak because of the "upslope" flow along an isentropic surface; this effect has been observed in numerical simulations by Brooks and Wilhelmson (1993). Furthermore, the maximum VPPGF is upstream of the maximum updraft: Physically, there has to be an upward pressure-gradient force in this location to account for the upstream displacement of the updraft relative to the peak buoyancy, since the buoyancy force by itself would give rise to a downstream displacement.

Without using all the equations in the linearized set we have successfully identified streamwise vorticity as the origin of updraft rotation, as first suggested by Browning and Landry (1963) and Barnes (1970). Our task is not complete because the streamwise direction is a function of the as yet unknown storm motion. Storm motion can be determined as an eigenvalue of the solution of the governing equation in h' (see appendix of Davies-Jones 1984), or deduced qualitatively from the inferredVPPGF around an axisymmetric updraft (Rotunno and Klemp 1982; Davies-Jones 1996b). According to linear theory, $\mathbf{c}$ for an axisymmetric thermal plume lies on the concave side of a simple curved hodograph (one that does not intersect itself), and on the hodograph if it is straight. This implies that updrafts will rotate cyclonically (anticyclonically) if the hodograph curves clockwise (anticlockwise), and will not rotate if the hodograph is straight.

At this point, we have exhausted linear theory. It has served us well by revealing the basic mechanism that causes updrafts to rotate at midlevels. It fails to explain storm splitting and nonlinear updraft propagation (a component to the movement arising from nonlinear forcing of new updraft on one side and suppression of updraft on the opposite side). Thus, it does not account for the development of mirror-image right- and left-moving supercells when the hodograph is straight, and it underestimates the intensity of updraft rotation for storms that deviate to the right of the mean wind when the hodograph turns clockwise with height. These are nonlinear effects that we describe next.

c. *Nonlinear theory of midlevel rotation*

1) GENERAL REMARKS

Two important processes that generate vertical vorticity are missing in the above linear theory. The first is amplification of vertical vorticity by vertical stretching of vortex tubes. This is a second-order effect because vertical vorticity is generated by tilting of the horizontal environmental vorticity in the linear solution and subsequently stretched in a second-order solution. The second is the tilting (at second order) of horizontal vorticity that has been generated (at first order) by horizontal buoyancy gradients, a process that is often important for the generation of rotation near the ground (section 5.2d). We also have to consider the nonlinear forcing terms in the diagnostic pressure equation because the associated VPPGF may play important dynamical roles in storm propagation and splitting.

Nonlinear theory is further complicated by moist processes such as evaporative cooling and latent heat released by condensation, which can no longer be ignored. For moist adiabatic processes, moist specific entropy S_E and equivalent potential temperature θ_E tend to be conserved in lieu of the dry specific entropy S and θ. Even in inviscid and isentropic flow, moist potential vorticity MPV $\equiv \boldsymbol{\alpha\omega}\cdot\nabla S_E$ is not conserved exactly because S_E depends on vapor mixing ratio q in addition to two independent-state variables (say T and p). But MPV is conserved for processes for which $q = q(T, p)$, for example, dry/moist adiabatic ascent of a parcel in a horizontally homogeneous environment.

We first investigate how strong the shear has to be to organize thunderstorm structure and then to induce splitting. A rough answer to this problem is supplied by a scale analysis of the forcing terms in the diagnostic pressure equation (see, e.g., appendix of Rotunno and Klemp 1982). Since the vertical advection of vertical velocity is comparable to buoyancy, the scale of the vertical velocity $W \sim \sqrt{\text{CAPE}}$, where CAPE $\equiv g\int_{LFC}^{EL}\{[\rho_p(z) - \bar{\rho}(z)]/[\bar{\rho}(z)]\}dz$ is the buoyant or convective available potential energy (Weisman and Klemp 1982). Here $\rho_p(z)$ is the density of a representative near-surface parcel that is lifted dry and then

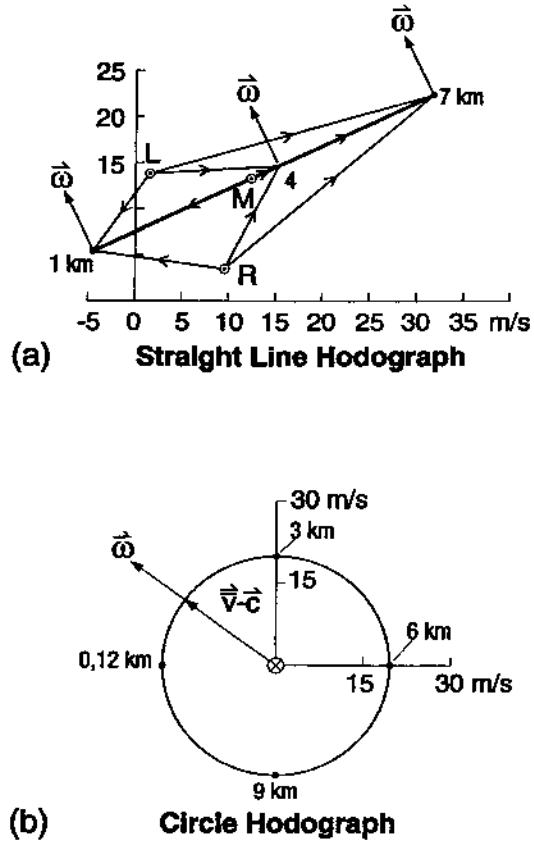

FIG. 5.8. Idealized (a) straight and (b) circle hodographs.

moist adiabatically. This parcel is buoyant from its level of free convection (LFC) to its equilibrium level (EL). From the conservation of (zero) moist potential vorticity, the vertical vorticity of a parcel is given by

$$\zeta = \boldsymbol{\omega} \cdot \nabla h , \tag{5.2}$$

where h is the finite vertical displacement of the parcel (Davies-Jones 1984; Rotunno and Klemp 1985). Thus, if S_0 is the scale of the low- to midlevel shear magnitude, D and H are the length scales for horizontal and vertical gradients, respectively, and $U_S \equiv S_0 H$, $\zeta \sim U_S/D$. Note that U_S can be interpreted as the length of the lower portion of a smooth hodograph (Weisman and Klemp 1982, 1984). For $D/H \sim 1/2$, the ratios of the forcing functions in the diagnostic pressure equation are

$$F_B : F_L : F_{NL} \sim \mathrm{Ri} : \sqrt{\mathrm{Ri}} : 1 , \tag{5.3}$$

where $\mathrm{Ri} \equiv \mathrm{CAPE}/U_S^2$ is a Richardson number, and F_B, F_L, F_{NL} are the forcing functions that involve buoyancy, linear dynamical terms, and nonlinear dynamical terms, respectively (Rotunno and Klemp 1982). Clearly, buoyancy effects dominate those of shear for $\sqrt{\mathrm{Ri}} \equiv W/U_S \gg 1$. As $\mathrm{Ri} \to 1$ from above, first the linear and then the nonlinear dynamic forcing become important, and storms should become more organized. Indeed, $\sqrt{\mathrm{Ri}}$ less than 2–2.5 is a general condition for supercells to form, at least in numerical simulations. Consistently, storm splitting in unidirectional shear occurs below a critical value of $\sqrt{\mathrm{Ri}}$ around 2–2.5. In mathematics, such a complete change in behavior at a critical value of a parameter is called a *bifurcation.*

Storms are affected by the shape of the hodograph as well as by its length. We now describe the behavior of supercell storms in two extreme environments, characterized by hodographs that are a straight line and a complete circle (Fig. 5.8). Nature occasionally produces hodographs that approximate one or other of these cases (Fig. 5.9). More importantly, by going from one extreme to the other we pass through a spectrum of different storm behaviors.

2) THE STRAIGHT-LINE HODOGRAPH

The rotational characteristics of convective storms growing in a unidirectionally sheared environment have been modeled analytically (Rotunno 1981) and numerically (e.g., Schlesinger 1978; Wilhelmson and

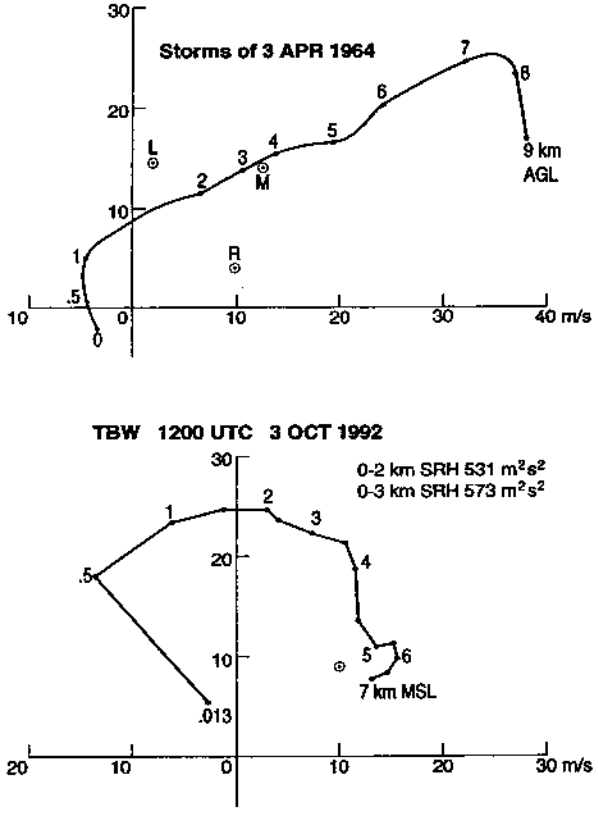

FIG. 5.9. Examples of actual hodographs that approximate (a) a straight hodograph, (b) a circle hodograph.

Klemp 1978). The results of the three-dimensional supercell simulations suffice to illustrate the nonlinear effects that lead to storm splitting, off-hodograph storm motion, and consequential updraft rotation.

For purposes of discussion, assume that the shear is westerly. If the earth's rotation is switched off, the numerical fields possess north–south symmetry or antisymmetry (depending on the variable) about a west–east vertical plane (the plane of symmetry). In agreement with linear theory, the storm moves initially with a velocity that lies on the hodograph and the updraft tilts the northward environmental vorticity, producing a vortex pair that is most intense at midlevels (e.g., Wilhelmson and Klemp 1978). Thus, the southern (northern) half of the updraft rotates cyclonically (anticyclonically), but the updraft does not rotate as a whole (Fig. 5.10).

At around 40 min into a simulation with strong shear, the initial storm splits along the plane of symmetry into two storms—a severe left-moving (SL) supercell and a severe right-moving (SR) supercell—that are mirror images of each other. The southern (northern) storm moves southeast (northeast), that is, off the hodograph to the right (left) of the shear vector. The initial updraft splits as a result of two nonlinear effects. First, precipitation accumulates in the center of the updraft and loads it down to such an extent that the updraft turns into a downdraft in the vicinity of the symmetry plane. Second, the midlevel vortices are centers of low pressure that induce new updraft growth on the flank. This new growth is enhanced by low-level convergence along the storm's gust front where cool, outflowing downdraft air converges with warm, moist inflow air. The southern (northern) storm propa-

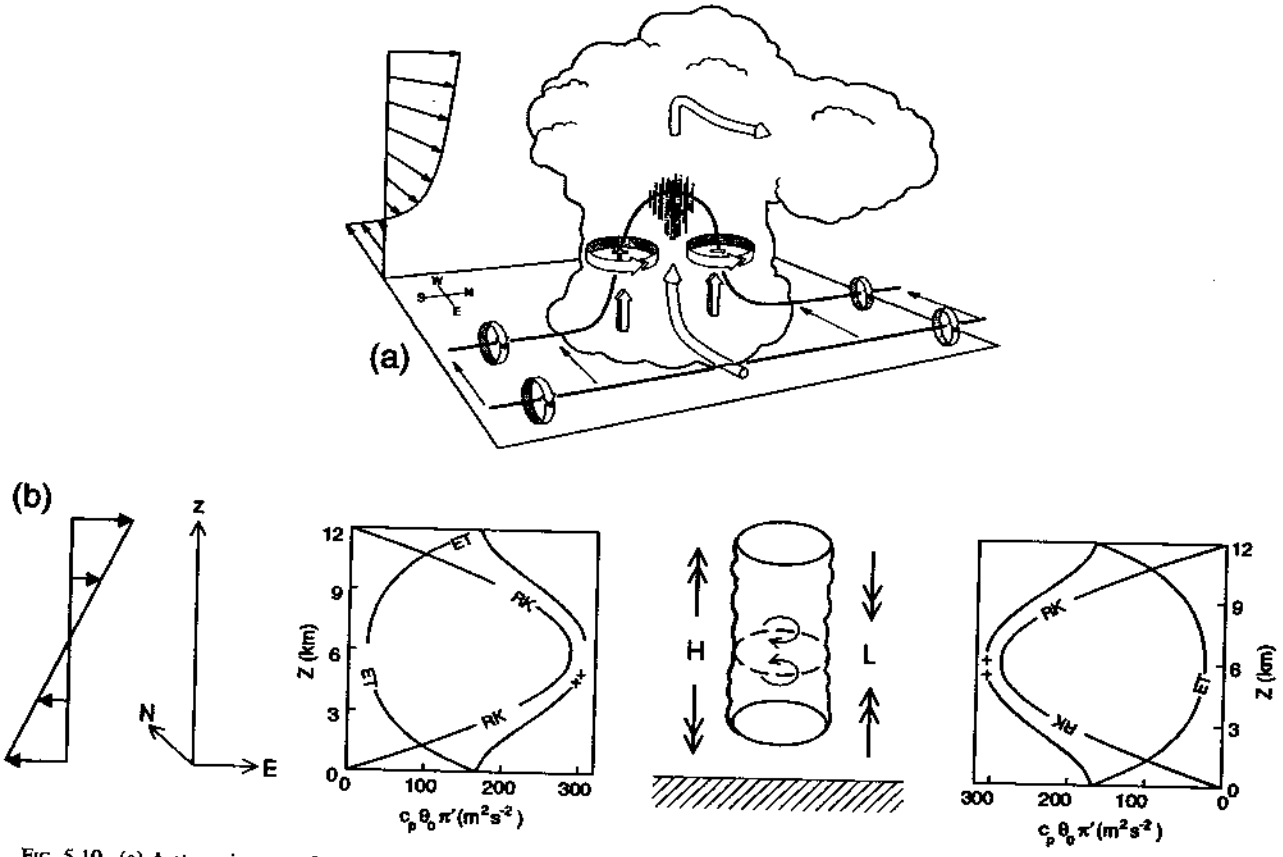

FIG. 5.10. (a) A storm in westerly shear prior to the onset of splitting. The cylindrical arrows depict the flow in the storm. The thick lines are vortex lines with the sense of rotation indicated by the circular-ribbon arrows. The shaded arrows give the direction of the VPPGF. From Klemp (1987; reprinted with permission). The updraft draws up loops of environmental vortex tubes, producing a cyclonic vortex on its right side and an anticyclonic vortex on its left side. (b) The linear pressure as a function of height on the upshear and downshear side of the updraft. The locations of the high and low are marked by H and L. The double arrows denote the direction of the VPPGF. The RK curves show the pressure according to Rotunno and Klemp's (1981) heuristic theory. The ++ curves include an extra term derived by Davies-Jones (1996b) to enable satisfaction of boundary conditions on pressure. ET is the extra term that has to be added to RK in order to satisfy the boundary conditions. The curved arrows depict the midlatitude vortices and associated lows of nonlinear pressure on the flanks of the updraft. From Davies-Jones (1996b).

gates to the right (left) of the shear vector as a result of updraft growth on its right (left) flank and decay on the opposite flank. By virtue of this propagation, the inflow into the right (left) mover has storm-relative streamwise (antistreamwise) vorticity. Thus, the right- (left-) moving updraft acquires overall cyclonic (anticyclonic) rotation as predicted by linear theory, given the "nonlinear storm motion," and the storms quickly become supercells. After the storms become widely separated, they may continue their leftward and rightward movement for several hours. The initial deviate motion from the split initiates overall updraft rotation, and the updraft rotation maintains the deviate motion that it needs for its own sustenance by the following mechanism. In the right- (left-) moving storm, the cyclonic (anticyclonic) vortex is the "leading vortex" because it is located close the the updraft maximum on its forward side, and the anticyclonic (cyclonic) vortex, which is in lesser updraft or even in downdraft above the cold pool on the storm's rear flank, is the "trailing vortex." Both midlevel vortices exert suction on the low-level air beneath them. However, the leading vortex has far more influence on updraft propagation because it is closer to the updraft maximum and because it lifts the more unstable air ahead of the updraft. Thus the updraft continues its deviate motion toward the leading vortex.

In nature perfect symmetry of SL and SR supercells is never realized because of Coriolis effects. First, amplification of the background vertical vorticity of the earth's rotation makes the southern updraft rotate slightly faster than the northern updraft. Second, frictional effects near the ground cause the hodograph to turn clockwise with height in the lowest 1 km (the Ekman layer), and this turning is enhanced by low-level warm advection. As evident in the veering of the near-surface winds relative to the left-moving storm in Fig. 5.9a, this can result in the "wrong" (i.e., streamwise) vorticity entering the left mover's updraft at very low levels. This may be the reason why left movers seldom produce tornadoes. The statistic that mesocyclones are about 50 times more frequent than mesoanticyclones (Davies-Jones 1986) indicates that nearly straight hodographs are comparatively rare.

3) THE CIRCLE HODOGRAPH

It is convenient to consider also the case of a circle hodograph, since in this case there is an exact steady-state solution of the inviscid, Boussinesq equations of motion[1] (Lilly 1982, 1983; Davies-Jones 1985). The solution represents a dry updraft in a neutrally stable environment. The governing equations are

$$\frac{\partial \mathbf{v}}{\partial t} + \nabla\left(\frac{\mathbf{v}\cdot\mathbf{v}}{2}\right) - \mathbf{v}\times\boldsymbol{\omega} = -\nabla\Pi - \nabla(gz), \quad (5.4)$$

$$\nabla\cdot(\mathbf{v}) = 0, \quad (5.5)$$

where $\Pi \equiv c_p\theta_0(p/p_0)^{\kappa}$, $\kappa \equiv R/c_p$, and θ_0 is the constant potential temperature of the dry adiabatic atmosphere. The price that one has to pay for the exact solution is the unrealistic absence of buoyancy. However, the exact solution is still useful because storms in environments with fairly low CAPE and quasi-circular hodographs with strong shear will strive toward this steady state without ever quite reaching it.

The exact solution belongs to the Beltrami class of flows. In a Beltrami flow, vorticity is everywhere parallel to velocity, that is, the Lamb vector $\mathbf{v}\times\boldsymbol{\omega}$ vanishes and

$$\boldsymbol{\omega} \equiv \nabla\times\mathbf{v} = \lambda\mathbf{v}, \quad (5.6)$$

where λ is a scalar called the abnormality (Truesdell 1954). The superposition of two Beltrami flows is also a Beltrami flow if—and only if—the abnormalities are the same. In our case we will superpose one Beltrami flow, which represents the "perturbed flow" associated with a rotating updraft, on another Beltrami flow, which represents a steady-state, horizontally homogeneous environment. The abnormality becomes the rate at which the storm-relative winds veer with height. Vorticity is divergence-free, so λ must satisfy the constraint

$$\nabla\cdot(\lambda\mathbf{v}) = 0. \quad (5.7)$$

Hence when (5.5) holds, λ must be a constant. The vector vorticity equation reduces simply to

$$\partial\boldsymbol{\omega}/\partial t = 0, \quad (5.8)$$

which implies that the solution we are seeking is steady. The vorticity tendency is zero because in the vector vorticity equation the solenoid and diffusion terms are zero and the advection term is exactly canceled by the stretching and tilting term.

As shown by Davies-Jones (1985), a Beltrami solution exists for an axisymmetric, rotating updraft within a Beltrami-flow-modeled environment that is characterized by an arc-shaped hodograph that turns more than 180°. A hodograph in the form of a clockwise-turning complete circle with center at the origin and a radius of 20 m s^{-1} is chosen here because Lilly (1982) found reasonable agreement in this case between the

[1] An exact solution also exists if the anelastic approximation is made in the continuity equation. We wish only to reveal the basic properties of the flow. Hence, the Boussinesq approximation is made, which simplifies the solutions. Strictly, the Boussinesq approximation is valid only for shallow convection. However, the solutions for deep convection are qualitatively similar.

nonbuoyant Beltrami solution and a numerically simulated storm in a moderately unstable environment. For instance, the simulated storm was quasi-steady and nearly stationary, and it had a strongly rotating updraft. Furthermore, the ratio of maximum vertical vorticity to maximum vertical velocity in the simulation agreed with the theoretical value to within 20%.

For a circle hodograph and values of W_0 (30 m s^{-1}) and H (12 km) characteristic of severe storms, where W_0 is a constant equal to the maximum vertical velocity and H is the depth of the updraft, the central flow consists of a rotating updraft that resembles a midlevel mesocyclone in structure, diameter, and intensity. Since the flow is Beltrami and steady, the streamlines, trajectories, and vortex lines all coincide. The trajectory through the midpoint of the updraft $(r, z) = (0, H/2)$ turns anticyclonically, even though the updraft is rotating cyclonically, because the effect of environmental wind veering overcomes that of cyclonic circulation (Klemp et al. 1981; Lilly 1983). Such trajectories have been observed in Doppler radar analyses and numerical simulations of rotating storms. The trajectories and vortex lines near the ground are almost horizontal; thus parcels entering the updraft do not develop significant cyclonic spin until they ascend above $H/6$.

For a steady Beltrami flow, Eq. (5.4) dictates that the pressure obeys the universal Bernoulli relationship

$$\begin{matrix} \Pi & + & gz \\ \text{specific [enthalpy} & + & \text{potential energy} \end{matrix}$$

$$\begin{matrix} + & \mathbf{v}\cdot\mathbf{v}/2 & = & C, \\ + \text{ kinetic energy]} & & = & \text{constant}, \end{matrix} \quad (5.9)$$

a consequence of the Lamb vector being zero. We now use the perturbed and environmental wind solutions in this relationship to obtain the pressure. The solution for pressure can be decomposed into a hydrostatic environmental part $\bar{\Pi}$, a linear part due to the storm-environment interaction Π'_L, and a nonlinear part due to intrastorm interactions Π'_{NL} where

$$\bar{\Pi} = -gz + C - M^2/2,$$

$$\Pi'_L = -\bar{\mathbf{v}}\cdot\mathbf{v}',$$

$$\Pi'_{NL} = -\mathbf{v}'\cdot\mathbf{v}'/2. \quad (5.10)$$

The pressure field has some surprising features. The flow is not in cyclostrophic balance. The nonlinear pressure is axisymmetric and so does not contribute to storm propagation. On the axis, it is proportional to W_0^2 with a spin-forced deficit of $H/2$ of 3 mb when $W_0 = 30$ m s^{-1}. There is no axial pressure deficit at the ground and no axial pressure excess at the top of the updraft. In contrast to the straight-hodograph case, the nonlinear pressure does not feature two lows on opposite flanks of the updraft, because the cyclonic vortex is now coincident with the updraft and the anticyclonic vorticity is in the ring of downdraft that surrounds the updraft. Consequently, the storm-splitting mechanism is absent here. Instead, the low at the updraft's midpoint exerts a suction on air beneath it, thus enhancing the updraft at low levels (Lilly 1986). Brooks and Wilhelmson (1993) demonstrated this effect by showing that updraft speed increases with hodograph curvature in simulated supercells.

The linear pressure is asymmetric and is proportional to MW_0, where M is the environmental wind speed. For $M = 20$ m s^{-1} it is comparable in magnitude to the axisymmetric component. At each level the linear pressure is low on the flank of the updraft where the deviation wind is in the same direction as the environmental wind, and high on the opposite flank (Fig. 5.4). Consequently, the highs and lows twist 180° around the rotating updraft from the ground to the top. Only at the midlevel is the linear horizontal pressure gradient in the direction of the shear vector (Rotunno and Klemp 1982). At the top, the pressure field resembles that predicted by the "flow around an obstacle" model of Newton and Newton (1959). At other levels the updraft is rather porous. It is evident from the asymmetric part of the vertical equation of motion,

$$-\frac{\partial \Pi'}{\partial z} = (\bar{U} + U')\frac{\partial w'}{\partial r} + w'\frac{\partial w'}{\partial z}, \quad (5.11)$$

that the maximum VPPGF is located on the upwind side of the updraft, as in linear theory. The whole updraft does not propagate toward this side because, in the absence of buoyancy, the asymmetric part of the VPPGF is exactly balanced by the advection of vertical velocity by the environmental wind, $-\bar{U}\partial w'/\partial r$. This simple analytical solution, and a companion numerical simulation of a supercell in a moderately unstable environment with the same hodograph (Lilly 1982, 1983), demonstrate that updrafts do not have to propagate relative to the mean wind in order to rotate, and that rotating updrafts do not necessarily propagate.

The Beltrami model offers an explanation of why, in surface observations of mesocyclones, the mesolow is often several kilometers ahead of the circulation center (Barnes 1978). This phenomenon is also apparent in many tornado pressure traces where the mesolow precedes the abrupt V-shaped fall associated with the tornado (which, based on Doppler radar data, is usually near the circulation center) by several minutes. In the storm's inflow the environmental and storm-induced winds are aligned, giving rise to an "inflow low" with a pressure deficit of a few millibars through the Bernoulli effect (Davies-Jones 1985; Brooks et al. 1993). The presence of the inflow low, along with lower hydrostatic pressure in the inflow, separates the mesolow center from the circulation center. The inflow

low is the location of the severe weather in our example, surface winds of 30 m s^{-1}. Stronger winds are present at the midlevel owing to the tangential and vertical components of the perturbation wind being greater than the radial component.

4) INTERMEDIATE CASES

Traditionally, supercells in general environments have been viewed as modifications of ones in unidirectional shear (e.g., Klemp 1987). The effect of clockwise turning of the shear vector with height has been viewed as enhancing (suppressing) the right- (left-) moving storm. This is a valid viewpoint for slightly curved hodographs, but does not seem appropriate for environments with strong hodograph curvature in which initial updrafts rotate and storm splitting either does not occur or is dynamically insignificant (Lilly 1983; Klemp 1987). An alternative viewpoint consists of recognizing the two idealized extremes (straight-line and circle hodographs). With increasing clockwise hodograph curvature, splitting disappears, the cyclonic vortex moves closer to the center of the updraft, linear effects gain in importance, and updraft rotation becomes increasingly disassociated from deviate updraft motion (Table 5.1).

d. Theory of rotation near the ground

As mentioned, rotation within the storm in roughly the lowest kilometer above the ground seems to develop from a separate mechanism than the one described in sections 5.2b and 5.2c. Although meso- or synoptic-scale vertical vorticity that preexists the storm has apparently been linked to near-ground mesocyclogenesis (e.g., Wakimoto et al. 1998), we limit the following discussion to near-ground mesocyclogenesis mechanisms involving storm-scale processes, since these have drawn most of the attention in the recent literature.

Significant near-ground rotation does not develop in the numerical simulations of Rotunno and Klemp (1985) and Davies-Jones and Brooks (1993) when the production of hydrometeors is turned off. This result was predicted by Davies-Jones (1982), who argued that, in a sheared environment with negligible background vertical vorticity, an "in, up, and out" type circulation driven by forces primarily aloft would fail to produce rotation close to the ground because vertical vorticity is generated in rising air. A strong updraft that is rotating only aloft may draw strong inflow from below, but its strongest winds are still high in the clouds; it seldom produces damaging winds at the ground without an accompanying downdraft. Rotation can be produced near the ground if the streamlines and vortex lines turned upward abruptly, instead of gradually, as in the Beltrami model. One way this could occur is by the steep uplifting of streamwise vortex lines by a gust front. The effect is not important in published numerical simulations, however, since it is not resolved by most numerical models and yet the models reproduce low-level mesocyclogenesis. The only other obvious way requires intense low pressure at the ground beneath the updraft, which in turn requires near-ground rotation! The dynamic pipe effect (DPE), which builds some tornadoes down to the ground via a type of bootstrap process, could lead to such a situation. However, the Beltrami mesocyclone is not in cyclostrophic balance, so that the DPE probably does not apply to mesocyclones in nature. Thus, streamwise vorticity in air flowing along the ground cannot cause a mesocyclone to make contact with the ground although it could, in principle, help to maintain an already established near-ground mesocyclone.

TABLE 5.1. Comparison of the properties of supercell storms in environments with nearly straight hodographs and with strongly curved hodographs that turn clockwise with height.

Property	(Nearly) straight hodograph	Strongly curved hodograph
Left/right symmetry	For straight hodograph & $\Omega = 0$	None
Net updraft rotation in initial storm	No	Yes
Cyclonic vortex in initial storm	On right side of updraft	In strong updraft
Anticyclonic vortex in initial storm	On left side of updraft	In downdraft or weak updraft
Storm splitting	Highly significant	Insignificant or absent
Deviate motion	Essential for mesocyclone (meso.)	Not needed for meso. formation
Time to first mesocyclone (meso.)	Slower	Faster
Low and midlevel meso. intensity	Generally less intense	Generally more intense
Mesoanticyclone	In left mover	Generally absent
Updraft strength in right mover (RM)	Weaker	Stronger, esp. at low $\sqrt{\text{Ri}}$
RM strength vs $\sqrt{\text{Ri}}$	Maximum at $\sqrt{\text{Ri}} \approx 1.7$	Increases with decreasing $\sqrt{\text{Ri}}$
Near-ground ζ vs $\sqrt{\text{Ri}}$	Maximum at $\sqrt{\text{Ri}} \approx 1.7$	Increases with decreasing $\sqrt{\text{Ri}}$
Barotropic and baroclinic vorticity	In opposite directions	In same direction
Violent tornado possible?	Yes	Yes
Tornado outbreak	Rare	More likely
Rotational dynamics	Highly nonlinear	More linear

Consistent with the numerical simulations, field observations confirm that tornadoes do not generally occur in the absence of rainy downdrafts. Water-loaded and/or rain-cooled downdrafts can cause strong surface winds and/or generate vertical vorticity by several mechanisms. First, in contrast to a nonbuoyant jet that slows down considerably as it approaches a boundary, a negatively buoyant downdraft can impact the ground with considerable force and spread out rapidly (Fujita 1985). Second, a downdraft may transport high-momentum air down to the surface. This may take the form of downward transport of horizontal momentum, which is associated with tilting of existing horizontal vorticity toward the vertical (Wiin-Nielsen 1973; Walko 1993) or of transport, within a mesocyclone, of angular momentum downward and inward toward the mesocyclone center. Finally, a cool downdraft affords the baroclinic generation of horizontal vorticity in the form of a toroidal circulation around the downdraft perimeter. This vorticity may also be tilted by differential vertical velocity.

1) Baroclinic mechanism

Klemp and Rotunno (1983) and Rotunno and Klemp (1985) showed that air entering the mesocyclone near the ground had traveled in the forward flank region of their simulated storm, along a strong baroclinic zone with warmer (cooler) air to its left (right), and acquired a large amount of streamwise vorticity generated by the associated buoyancy torque. As this advancing, moderately chilled air is ingested into the updraft, its spin is tilted upward and amplified by vertical stretching, giving rise to slightly elevated rotation because the vertical spin develops as the air is rising. In some fortuitous encounters, the cool-air outflow may come from a neighboring storm instead of the storm's own downdraft. Davies-Jones and Brooks (1993) and Davies-Jones (1996a, 2000a) demonstrated that near-ground cyclonic vorticity develops first in the downdraft on the left side of its centerline (looking downwind). The passage of cyclonically spinning air from the downdraft into the updraft and subsequent vertical stretching of this air completes a cyclonic vortex column from very close to the ground to midaltitudes or higher. We now review the concepts of baroclinic and barotropic vorticity, and then apply these to theory that explains the baroclinic generation of vorticity in a downdraft.

Dutton (1976) showed from an integral of the vector vorticity equation that absolute vorticity in dry, inviscid, isentropic flows is the sum of barotropic and baroclinic components, that is,

$$(\xi, \eta, \zeta + f) \equiv \boldsymbol{\omega}(x, y, z, t) = \boldsymbol{\omega}_{BT}(x, y, z, t) + \boldsymbol{\omega}_{BC}(x, y, z, t), \quad (5.12)$$

where the components satisfy the initial conditions

$$\boldsymbol{\omega}_{BT}(x, y, z, 0) = \boldsymbol{\omega}(x, y, z, 0),$$
$$\boldsymbol{\omega}_{BC}(x, y, z, 0) = 0 \quad (5.13)$$

at some arbitrarily chosen initial time $t = 0$; $\boldsymbol{\omega} = \boldsymbol{\omega}_{BC}$ is a solution of the inviscid vector vorticity equation for isentropic flow and $\boldsymbol{\omega} = \boldsymbol{\omega}_{BT}$ satisfies the inviscid barotropic version of the same equation (without the solenoidal term), which is the necessary and sufficient condition for frozen vortex lines (Borisenko and Tarpov 1979).

Physically, the barotropic vorticity at time t is the vorticity that would develop from the amplification and reorientation of initial relative vorticity and the earth's vorticity if there were no baroclinic generation of vorticity. Barotropic vortex lines are "frozen" into the fluid and behave like elastic strings that the flow moves, stretches, and reorients. Thus, the barotropic vorticity of a parcel depends on initial vorticity, and the initial and current positions of the parcel and its neighbors along the vortex line through the parcel, but not on the parcel positions at intermediate times. The baroclinic vorticity of a parcel, given by

$$\boldsymbol{\omega}_{BC} = \nabla\Lambda \times \nabla S, \quad (5.14)$$

where $\Lambda \equiv \int_0^t T d\tau$ following a parcel, T is temperature, and S is entropy, depends on its cumulative temperature since $t = 0$ (Dutton 1976); the vorticity is subsequently affected by vortex-tube stretching and tilting. The baroclinic vortex lines lie in isentropic surfaces; hence the baroclinic component does not contribute to potential vorticity.

A modification of Eq. (5.14) is used in a Lagrangian model by Davies-Jones (2000a) to deduce analytically that cyclonic (anticyclonic) vertical vorticity forms from baroclinic vorticity on the left (right) side of a downdraft. He showed that the baroclinic vorticity can be expressed as

$$\boldsymbol{\omega}_{BC} = (\xi, \eta, \zeta)_{BC} = N^2\left(-\frac{\partial H}{\partial y}, \frac{\partial H}{\partial x}, \frac{\partial H}{\partial x}\frac{\partial h}{\partial y} - \frac{\partial H}{\partial y}\frac{\partial h}{\partial x}\right), \quad (5.15a)$$

where $N^2 \equiv (g/c_p)\partial S/\partial z$ is the local static stability or the square of the Brunt–Väisälä frequency ($N^2 < 0$ for unstable stratification); $h(x, y, S, t)$ is the height of an isentropic surface of entropy S, which has height $h_{-\infty}$ at upstream infinity; $h'(x, y, s, t) \equiv h(x, y, S, t) - h_{-\infty}$ is the "perturbation" height of a point on an isentropic surface, relative to the height of the surface at upstream infinity; and

$$H(x, y, S, t) \equiv \int_0^t h'(X, Y, S, \tau) d\tau$$

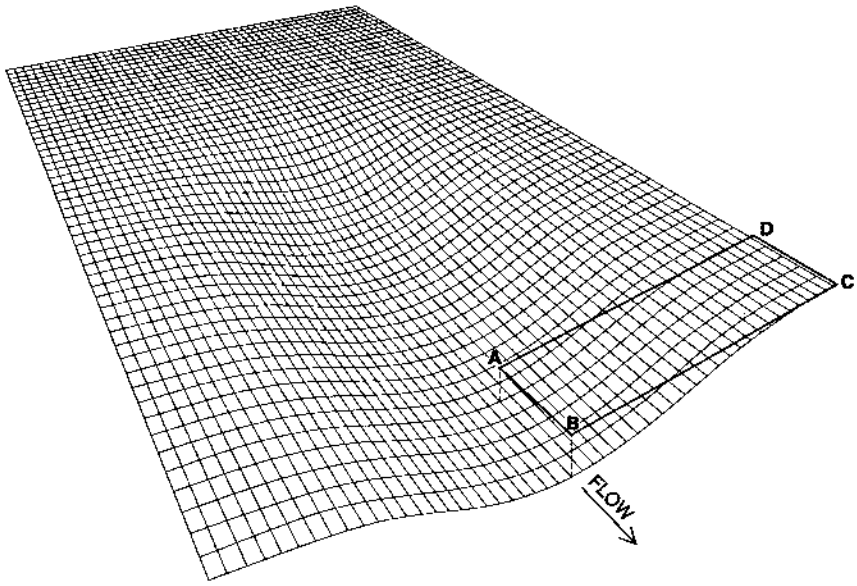

FIG. 5.11. Example of an isentropic surface in a horizontally homogeneous upstream environment. The isentropic surface has the shape of a semi-infinite valley extending downstream. ABCD is a material area, which far downstream is rectangular, and level at time t. Side CD is in the surface, but AB, which lies along the x axis, is in a higher isentropic surface. The baroclinic term in the vorticity equation continually generates vorticity within the surface in the shape of hairpins.

is the cumulative height perturbation, computed following the parcel initially located in isotropic coordinates at (X, Y, S). Note from Eq. (5.15a) that

$$\zeta_{BC} = \xi_{BC}\frac{\partial h}{\partial x} + \eta_{BC}\frac{\partial h}{\partial y}. \qquad (5.15b)$$

The vorticity field described by (5.15) has the following properties. The quantity N^2H is the "streamfunction" of the horizontal vorticity field (Figs. 5.11, 5.12). In other words, the horizontal projections of the vortex lines are also contours of H, the magnitude of horizontal vorticity is proportional to the spacing of the H contours and the local static stability, and the direction is given by the rule that historically warmer (cooler) air is located to the left (right) side of an observer looking along the local horizontal vorticity vector. Because the vortex lines lie in the isentropic surface (zero potential vorticity), the vertical vorticity is cyclonic (anticyclonic) where the horizontal vorticity vector points across the height contours toward higher (lower) values (Fig. 5.12). Height contours coincide with contours of baroclinic generation of vorticity and also with isotherms. The magnitude of the vertical vorticity is proportional to N^2 and the number of solenoids of H and h per unit area. If $|\nabla h| \ll 1$, the vertical vorticity is much smaller than the horizontal vorticity.

As with the linear theory of midlevel rotation, we again illustrate the vortex dynamics using isentropic surfaces that are deformed in some simple way. The isentropic surface height field can be provided as in Davies-Jones (2000a) through a three-dimensional potential-flow solution of the inviscid momentum and continuity equations in the absence of stratification and shear; the solution constitutes the primary flow, in a primary-flow–secondary-flow approach (Taylor 1972; Scorer 1978). The secondary flow is the first-order correction arising from the inclusion of stratification and vertical shear as functions of the height ($h_{-\infty}$) in a horizontally homogeneous upstream environment. The secondary vorticity is determined via Eq. (5.15) by the environmental stratification and shear and by the primary flow; it does not modify the primary flow and, hence, acts as a passive vector, an obvious limitation of the model.

Consider the flow under an axisymmetric fairing, placed in a uniform stream $U\mathbf{i}$ (Batchelor 1967) (Figs. 5.11, 5.13). This primary-flow case of Davies-Jones (2000a) illustrates the danger that may be latent in narrow currents of descending, rain-cooled air. Assuming unstable stratification, the air that sinks adiabatically is cooler than its surroundings and the baroclinic term continually generates vorticity in the isentropic surfaces (Fig. 5.11). Mesocyclonic-scale cyclonic (anticyclonic) vertical vorticity originates from cumulative tilting of baroclinically generated crosswise vorticity [the $\eta\partial h/\partial y$ term in (5.15b)] on the north (south) side of the depression in the isentropic

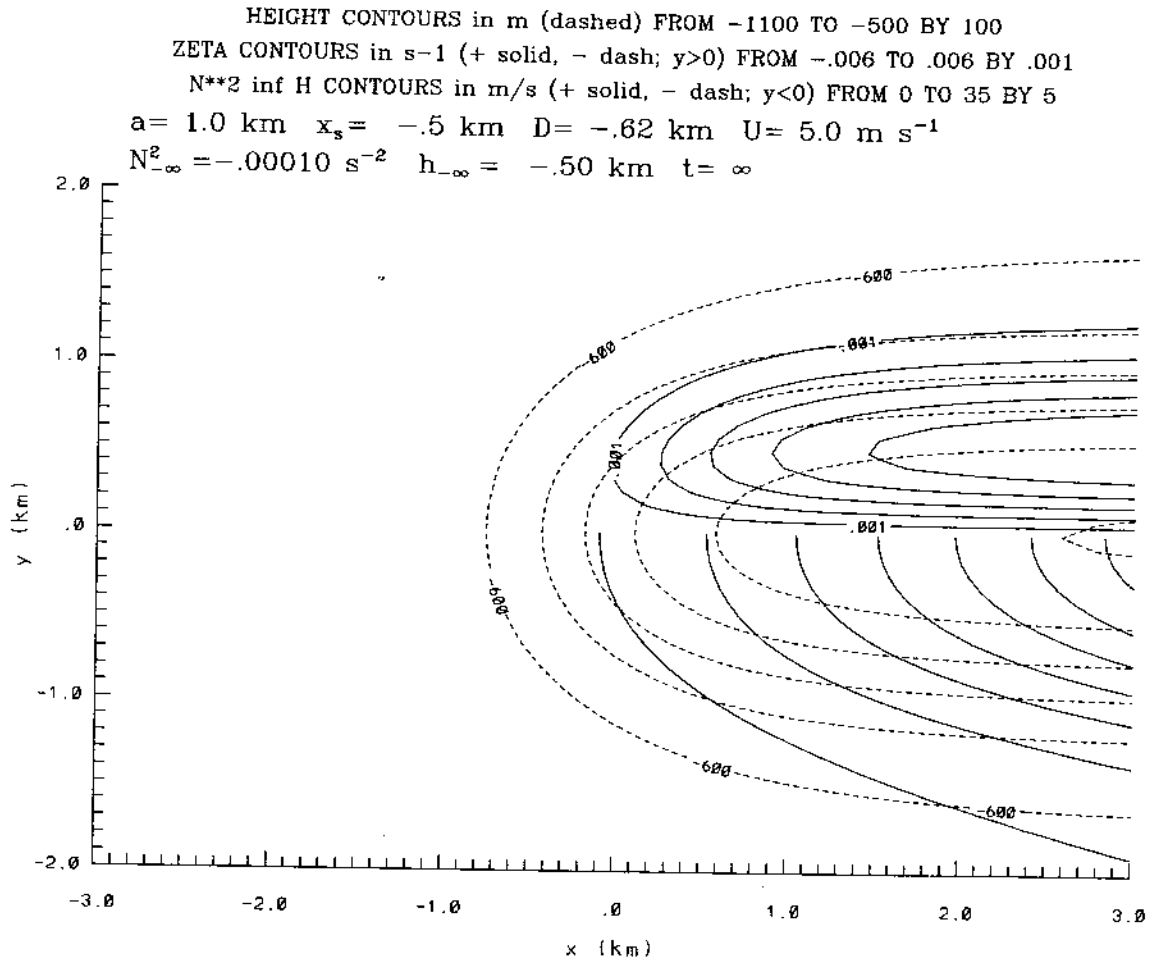

FIG. 5.12. Height contours (dashed) of the isentropic surface depicted in Fig. 5.11, contours of cumulative height (solid, drawn only for $y \leq 0$), and contours of vertical vorticity (solid, drawn only for $y > 0$). The accumulated height and vertical vorticity fields are symmetric and antisymmetric, respectively, about $y = 0$. In the surface, temperature contours and contours of baroclinic generation of vorticity both coincide with the height contours, and cumulative temperature and vortex lines both coincide with the cumulative height contours.

surfaces (Fig. 5.12). Cumulative tilting of baroclinically generated streamwise vorticity, $\xi \partial h/\partial x$, produces vertical vorticity of the opposite sign during the descent and vanishes at downstream infinity.

We can also explain the development of rotation about a vertical axis in terms of circulation Γ instead of vorticity. The origin of the circulation can be determined by advecting the material area ABCD (Figs. 5.11, 5.14)—which is far downstream, rectangular, and level at time t—backward in time. The side AB lies on the axis and lies in the trough of a surface of constant entropy, say, S_1. The side CD on the left side of the flow lies in a surface of higher constant entropy, say, $S_2 > S_1$ because the stratification is unstable. At an earlier time the back edge DA is higher than the leading edge BC so that the mean temperature along side DA, $\bar{T}_{DA}$, is lower than $\bar{T}_{BC}$. From Bjerknes's circulation theorem (Dutton 1976),

$$\frac{d\Gamma}{dt} = \oint_{ABCD} T dS$$

$$\approx (S_2 - S_1)\bar{T}_{BC} + (S_1 - S_2)\bar{T}_{DA} > 0, \quad (5.16)$$

so positive circulation around the material circuit is generated in the downdraft. The contour and its circulation evolve in a similar way to those in diagnostic studies of the origins of near-ground rotation in numerical simulations (Rotunno and Klemp 1985; Davies-Jones and Brooks 1993; Trapp and Fiedler 1995). Thus, the essential physics of rotation near the ground seems to be contained in the analytical model.

A scale analysis of Eq. (5.15) (Davies-Jones 2000a) indicates that long, narrow, deep downdrafts with moderate flow through them in highly unstable envi-

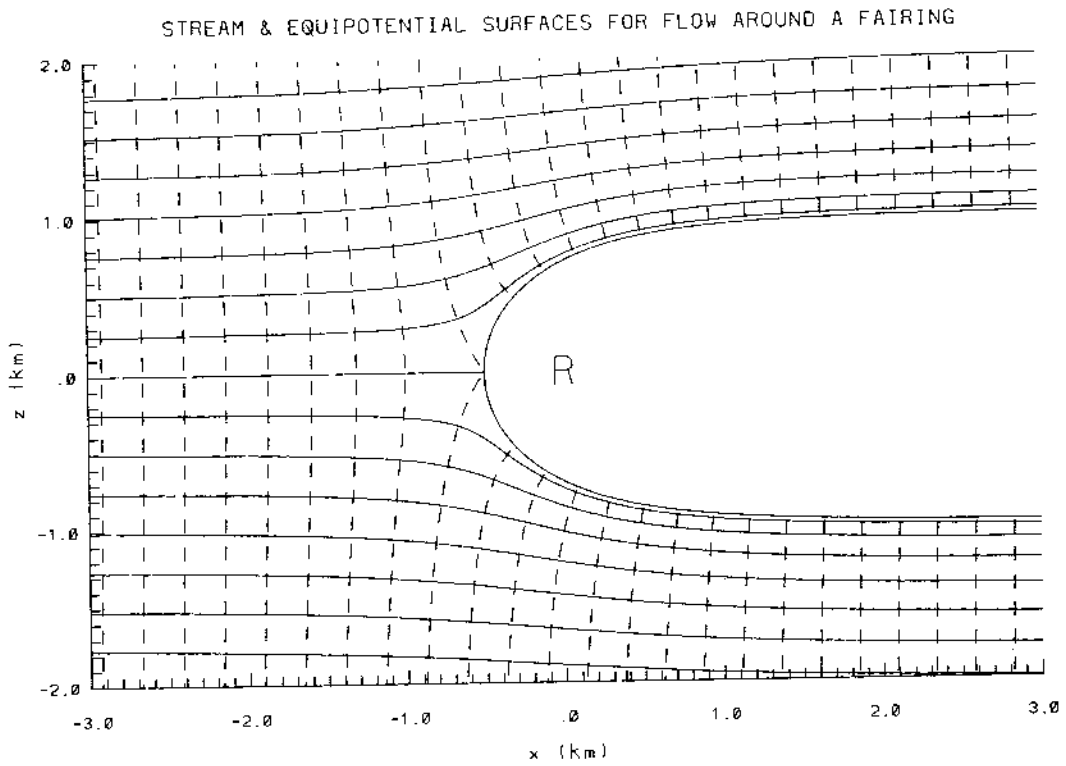

FIG. 5.13. The stream (solid) and equipotential (dashed) lines in the $y = 0$ plane for three-dimensional irrotational flow around an axisymmetric semi-infinite fairing of 2-km maximum width. The flow is in the positive x direction and is uniform at upstream infinity. The stream surfaces are the surfaces of revolution obtained by revolving the streamlines about the x axis. R is the location of the source that when placed in the uniform stream gives rise to the flow as shown. The isentropic surface in Fig. 5.11 is the material surface of this flow that consists of the union of all streamlines with the same height, −0.5 km, at upstream infinity. The thickly drawn streamline is the intersection of the isentropic surface with the $y = 0$ plane.

ronments produce the most vorticity in a moderate time (the vorticity forms on the advective timescale). This scale analysis, and also the analysis of Klemp and Rotunno (1983, p. 365), indicates additionally that the baroclinic vorticity is proportional to U^{-1}, where U is an advective velocity scale. Hence if the flow is too strong the parcels pass through the baroclinic zone too quickly to acquire appreciable baroclinic vorticity. On the other hand, if the flow is too weak, the parcels take too long to pass through the zone and the process becomes vulnerable to disruption by other events such as the cool air spreading out and undercutting the main updraft.

We note that the ultimate result of a near-ground mesocyclone may be influenced positively or negatively by barotropic vorticity (which, again, depends on the initial vorticity), as demonstrated by the model simulations of Davies-Jones and Brooks (1993) and Walko (1993). Consider, for example, the case when the initial vorticity is purely positive (negative) crosswise: Tilting of barotropic vorticity produces cyclonic (anticyclonic) vertical vorticity on the left side of the downdraft and the opposite sign of vorticity on the right side of the downdraft. When the initial vorticity is purely streamwise (antistreamwise), tilting gives rise to anticyclonic (cyclonic) vorticity during descent but the vertical component vanishes where the streamlines bottom out. As the air reascends, tilting of barotropic vorticity imparts cyclonic (anticyclonic) vorticity to the updraft.

Synthesizing the results of Davies-Jones (2000a), Davies-Jones and Brooks (1993), and Rotunno and Klemp (1985), among others, we can conceptualize an answer to the question of how near-ground rotation forms baroclinically in a supercell: Initially, the supercell's main updraft has strong cyclonic rotation aloft as a result of tilting of streamwise vorticity associated with the storm-relative environmental winds veering with height. There is little rotation near the ground at this stage because the cyclonic vorticity is being generated in rising air. The mesocyclonic rotation draws a thin curtain of rain around the rear side of the mesocyclone, where it falls into dry air that is overtaking the storm and is diverted around the updraft. As it enters and flows through the precipitation region, the dry air is cooled and moistened by evaporating rain, becomes negatively buoyant, and descends to near the ground. If the air flow is cyclonically curved instead of

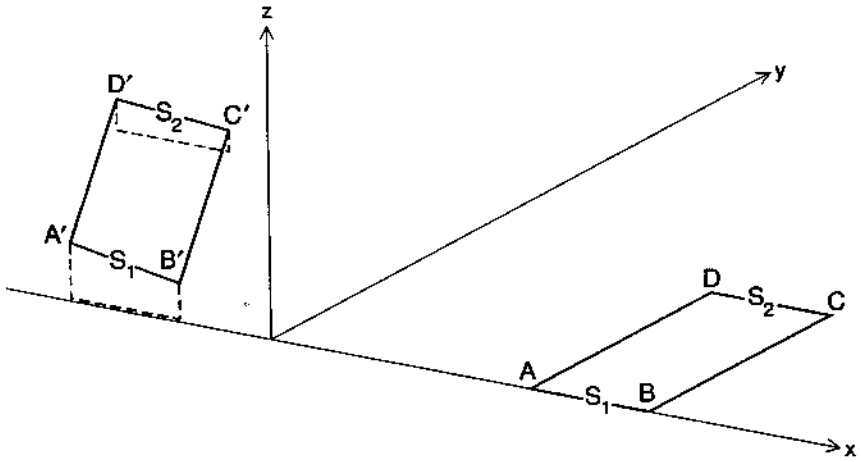

FIG. 5.14. Schematic showing the material circuit in Fig. 5.11 at time t (ABCD) and at an earlier time when it was farther upstream (A′B′C′D′). The side A′D′ is higher and cooler on average than the side B′C′. The material lines AB and CD lie in the surfaces of constant entropy S_1 and S_2, respectively. In unstable stratification $S_1 < S_2$ and the circuit acquires positive circulation according to Bjerknes's circulation theorem.

straight as in the analytical model, crosswise vorticity will be converted into streamwise vorticity by the "river-bend effect" (Fig. 5.15; Shapiro 1972; Scorer 1978; Adlerman et al. 1999). Horizontal vorticity is generated solenoidally at the entrance and along the sides of the downdraft (Fig. 5.12). The vortex lines are tilted upward in the downdraft as described above, producing cyclonic (anticyclonic) vorticity on the left (right) side of the downdraft. The air then exits the downdraft and flows along the ground. The storm's main updraft, which is rotating strongly aloft, lies ahead and to the left of the advancing air (Fig. 5.3), a location that breaks the left–right symmetry that the analytical model is forced to have for the sake of an easy solution. The main rotating updraft sucks up cyclonically rotating, almost saturated, rain-cooled air (through the suction effect described in section 5.3) and stretches it vertically, thus amplifying the vertical vorticity close to the ground and creating a rapidly rotating wall cloud in the process (Rotunno and Klemp 1985). As this air rises, its streamwise vorticity is tilted upward and the resulting vertical vorticity is stretched, a process that adds to its already cyclonic spin. Although the mesocyclone consists simply of a cyclonically rotating updraft at midlevels, near the ground it is composed of both rotating updraft and downdraft (hence the term *divided mesocyclone;* Lemon and Doswell 1979) with the vertical vorticity maximum lying just on the updraft side of the interface between the updraft and a downdraft on the storm's rear flank. The ingestion into the right rear side of the updraft of cyclonically spinning air that has passed through the left side of the downdraft completes a huge vortex column that extends from the ground to 12 km in extreme cases. The rain curtain is seen on a nearby radar as a hook-shaped appendage (henceforth called a hook) extending from the storm's echo (Fig. 5.16). Surface observations (Fujita 1958; Rasmussen and Straka 1996) reveal a zone of high pressure and divergent flow at the surface beneath the hook. In the above scenario, Davies-Jones has theorized that the rain curtain/hook is not simply a passive indication of near-ground mesocyclonic rotation, but the instigator of it, and the link between rotation aloft and near the ground.

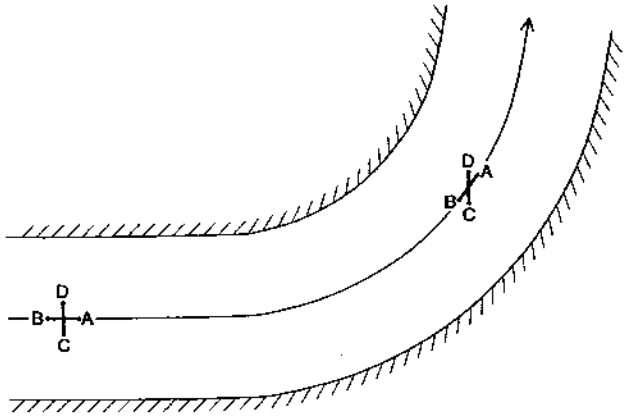

FIG. 5.15. Diagram of flow around a river bend, demonstrating the development of streamwise vorticity. Upstream of the bend the flow is parallel with speed shear (crosswise vorticity) owing to friction at the river bottom. Consider the fluid cross ABCD with arm AB along a streamline and CD along a vortex line. Since flow around the bend generates no vertical vorticity to a first approximation, the arms of the cross must rotate in opposite directions. Thus the vortex line CD turns toward the streamwise direction AB.

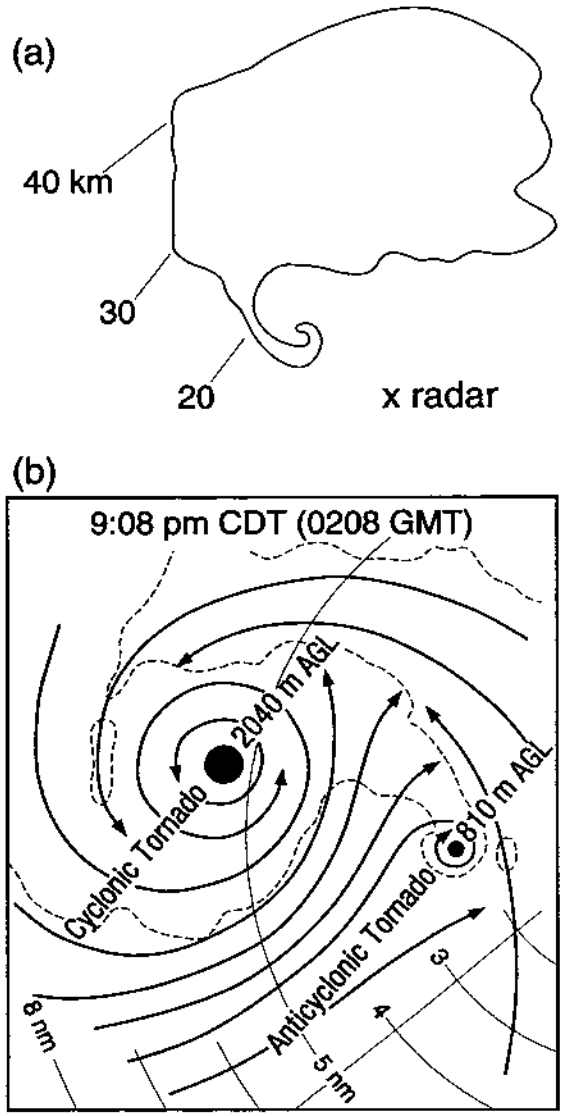

FIG. 5.16. (a) A cyclonic hook (from Garrett and Rockney 1962). (b) Surface flow (arrows) and radar echo (dashed) associated with simultaneous cyclonic and anticyclonic tornadoes at Grand Island, Nebraska, 3 June 1980. (From Fujita and Wakimoto 1982.) Note the wrapped-up cyclonic hook with a central eye and the anticyclonic hook to its ESE.

What happens to the anticyclonic vortex on the right side of the downdraft? In some cases it may be entrained into an updraft in the flanking line of convective towers that extend outward from the right rear of the main updraft. This gives rise to a low-level mesoanticyclone and occasionally anticyclonic tornadoes (Fig. 5.16; Brown and Knupp 1980; Fujita and Wakimoto 1982). The mesoanticyclone is generally weaker than the mesocyclone because the baroclinic streamwise vorticity is antistreamwise, that is, in the opposite direction to the streamwise vorticity generally present in the environment. This makes an intense, deep, mesoanticyclone unlikely. Instead, the weaker mesoanticyclone will tend to revolve partly around the stronger mesocyclone to its north.

The near-ground mesocyclone should form more slowly and be less intense if the barotropic vorticity opposes the baroclinic vorticity and hence retards and weakens the developing baroclinic circulation (e.g., Wicker 1996). This seems to be the case when the shear is unidirectional, as in Rotunno and Klemp's (1985) simulation where the circulation around a fluid circuit encompassing the near-surface vorticity maximum becomes negative when the circuit is traced back 20 min in time. As it is taken backward in time, the circuit starts climbing the plane of symmetry. It is evident in their Figs. 11 and 13 that around the elevated portion of the circuit at the earlier time the circulation around the circuit associated with the mean flow is opposed to the thermal circulation. In Walko's (1993) simulation, the vortex formed as a result of tilting of barotropic vorticity in the downdraft with the solenoidal effects acting to weaken the circulation. This finding may be a result of the imbalance in his initial conditions. The cold pool is present initially without any of the vorticity that would be generated naturally by buoyancy torques as the cold pool formed.

2) BAROTROPIC MECHANISMS

Brandes (1984a) retrieved buoyancy from dual-Doppler wind fields of a tornadic supercell to investigate the hypothesized role in mesocyclogenesis of horizontal buoyancy gradients and attendant baroclinic vorticity generation. His analyses suggested little contribution of horizontal baroclinic vorticity to mesocyclone intensification and subsequent tornadogenesis, although cautions were raised about uncertainties in the retrieved buoyancy. Recent surface measurements are consistent, however, with this apparent lack of baroclinity: During the Verification of the Origins of Rotation in Tornadoes Experiment (VORTEX; Rasmussen et al. 1994) and its follow-on experiments, the "mobile mesonet" (see Straka et al. 1996) detected cool temperatures and moist entropies at 3 m AGL beneath a few of the tornadic hook echoes observed at close range on (airborne and/or mobile) Doppler radars, but found negligible surface temperature and entropy perturbations in hook echoes that were associated with the stronger tornadoes (Markowski 2000). In the clear slot south of the hook, temperatures were warmer and moist entropies lower than ambient, consistent with forced unsaturated descent of air in a potentially unstable environment. One must conclude that there is (i) baroclinity of the correct sense near the ground that was not sampled by the mobile mesonet (which is limited by existence of adequate roads and by the relatively small number of sensors that comprise the mesonet), (ii) baroclinity of the correct sense aloft that is not revealed by observations at 3 m AGL, or (iii) a barotropic mechanism for near-ground mesocyclogenesis in addition to the baroclinic one. Parcels descending in a counter-

clockwise direction around the updraft would travel along an appropriate baroclinic zone aloft if the updraft were warmer than the environment at low levels (E. N. Rasmussen and K. A. Browning 1999, personal communication). This would require a low level of free convection. Some support for this hypothesis is found in the extensive analyses by Rasmussen of the VORTEX data collected near the Dimmitt, Texas, tornado on 2 June 1995. However, the analyzed fields are consistent also with a barotropic mechanism. We now explore the possibility of such a barotropic mechanism.

As already discussed, the vortex in Walko's (1993) idealized simulation formed from barotropic vorticity. Rothfusz and Lilly (1989) showed how near-ground rotation and even a tornado might be generated from a helical environment without baroclinic effects via theoretical analysis and a modified Ward tornado simulator (section 5.4). The simulator was changed so as to provide an inflow that veered with height without net circulation. Their theoretical analysis and that of Brooks et al. (1993) show that, as the inflow accelerated into the center of the apparatus, the streamwise vortex lines were stretched, generating a roll-type circulation with ascent on the left side and descent on the right side of the inflow at each level (Fig. 5.17). The vortex is produced by vertical eddy transport of angular momentum in the secondary helical flow. The positive angular momentum on the right side of the inflow remains at low levels until it reaches small radii, while the negative angular momentum on the left side is transported upward at large radii. A vortex forms near the center as a result of this process.

Davies-Jones (2000b) has constructed a simplified axisymmetric numerical model to demonstrate how rotation can be lowered to the ground by a barotropic mechanism. The model's initial condition consists of a central axisymmetric nonbuoyant updraft that rotates cyclonically at midlevels (a midlevel mesocyclone) surrounded by a concentric anticyclonic downdraft in which the angular momentum is still positive. The initial state is perturbed by adding potential energy through the introduction of a prescribed distribution of hydrometeors with constant fall velocity at the top boundary, a procedure used by Eskridge and Das (1976) and Proctor (1988). The rain falls in a curtain near the updraft–downdraft interface and most of it reaches the ground without being recirculated in the updraft. The model excludes conventional buoyancy forces associated with temperature differences to avoid the occurrence in the closed domain of unrealistic buoyancy recirculations or oscillations. The descent of the liquid water represents a conversion of potential energy into meridional kinetic energy.

Preliminary results indicate that the associated drag force intensifies the downdraft and causes a downward transport of angular momentum. Part of the outflow from the downdraft is directed inward, thus transporting high-angular-momentum air and increasing convergence into the central updraft's lower regions. From a vorticity perspective the low-level spinup is a result of upward tilting of inward radial barotropic vorticity and stretching of cyclonic vertical barotropic

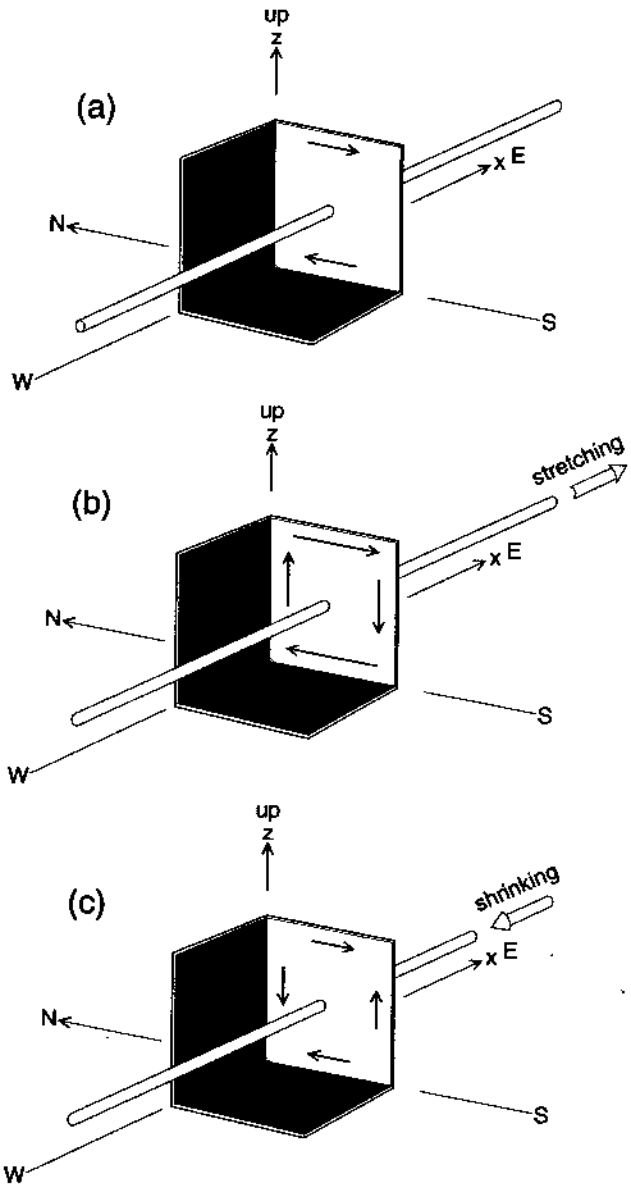

FIG. 5.17. Generation of vertical motion by longitudinal stretching or shrinking of streamwise vorticity. The length of the flow arrows is proportional to wind speed. (a) Conditions in the far upstream environment. Here there is vertical shear transverse to the wind associated with the streamwise vorticity, but no vertical motion. (b) Local stretching of the vortex lines in accelerating flow. The transverse shear intensifies and upward (downward) motion develops on the left (right) side of the flow. (c) Local shrinking of the vortex lines in decelerating flow. The transverse shear weakens and downward (upward) motion develops on the left (right) side of the flow.

vorticity. Baroclinic vorticity is generated as azimuthal vorticity by horizontal torques associated with radial gradients of the drag force, but it remains in this component because the axisymmetry prohibits tilting of azimuthal vorticity. Since angular momentum is nearly conserved owing to relatively slow diffusion at large Reynolds number, the maximum tangential velocity intensifies as parcels move downward and inward. Simultaneously the pressure low deepens and travels down the axis from its initial midlevel position. The associated pressure-gradient forces cause the low-level streamlines to slope downward (analogous to a rear-flank downdraft/clear slot) before turning sharply upward into the contracting central vortex. This penetration of the anticyclonic downdraft toward the axis surrounds the vortex with anticyclonic vorticity, resulting in a surface pressure profile $p(r)$ with a steeper than expected slope near the radius of maximum winds and a flatter than expected slope at larger radii (as in the tornadic pressure trace obtained by Winn et al. 1999). Far aloft, the top of the updraft turns to downdraft (a collapsing top) in response to a downward axial pressure-gradient force. The near-ground rotation clearly originates from inward and downward transport of angular momentum associated with the initial mesocyclone aloft, not from a baroclinic mechanism.

e. Forecast parameters

We can now interpret various forecast parameters in the light of the above paradigms of mesocyclone formation. The properties of three modern parameters, each of which contain some, but not all, of the important physics, are summarized in Table 5.2.

The dimensionless bulk Richardson number (BRN; Weisman and Klemp 1982, 1984) has been quite successful in predicting the conditions under which storms will split and supercells will form. It is defined by BRN ≡ CAPE/BRNKE. Here CAPE is the buoyant energy defined in section 5.2c and BRNKE ≡ $(\Delta\bar{U})^2/2$, where $\Delta\bar{U} \equiv |\bar{\mathbf{v}}_{0-6} - \bar{\mathbf{v}}_{0-.5}|$ and $\bar{\mathbf{v}}_{0-6}$ and $\bar{\mathbf{v}}_{0-.5}$ are the density-weighted mean winds in the lowest 6 and 0.5 km, respectively. The maximum updraft velocity is $\sqrt{2\,\text{CAPE}}$ according to parcel theory. The denominator, BRNKE, is the kinetic energy of the mean wind in the lowest 500 m in a reference frame moving with the mean wind in the lowest 6 km. If the latter is viewed as an estimate of storm motion, then BRNKE is simply the storm-relative kinetic energy of the inflow in the lowest 500 m. Alternatively, one can interpret $\Delta\bar{U}$ as a measure of the environmental shear in the lowest 6 km, with large $\Delta\bar{U}$ being the condition for the formation of strong midlevel vortices. In theory, supercell storms will not develop at large BRN

TABLE 5.2. Comparison of the properties of three forecast parameters (ignoring dependence of BRN on CAPE because other two parameters may be nondimensionalized by CAPE and $\sqrt{\text{CAPE}}$ if desired).

Property	SRH	BRN	Length of HODO.
Predictor of	Net updraft rotation (including sign)	Supercells, splitting storms	Tornadic storms, mesocyclones
Physics contained	Potential for midlevel updraft rotation	Buoyant energy/inflow kinetic energy	Mean magnitude of shear in 0–4-km layer
Geometric interpretation on hodograph diagram	$-2\times$ signed area swept out by storm-relative wind between 0 and 3 km	BRNKE $\equiv (\Delta\bar{U})^2/2$ $\Delta\bar{U} \equiv \lvert\bar{\mathbf{v}}_{0-6} - \bar{\mathbf{v}}_{0-.5}\rvert$	Arc length
Dependence on hodograph shape	Highly dependent	Less dependent	Independent
Function of storm motion c?	Linear function of observed (or forecast) c	No	No
Sensitivity to c (nearly straight hodographs)	Highly sensitive	None	None
Sensitivity to c (highly curved hodographs)	Insensitive. Substituting mean wind for c gives good estimate of helicity	None	None
Differentiates storms in same environment by their motion?	Yes, may warn on storm that deviates to right (e.g., along a boundary)	No	No
Mirror image storms	Opposite signs	Same value	Same value
Sensitivity to surface-inflow wind	Moderate	High (important for supercell vs multicell)	Low
Volatility with respect to hodograph changes	More volatile	Less volatile	Less volatile
Galilean invariant?	Yes (no if estimate of c is not invariant)	Yes	Yes
Winds included	0–2 or 3 km explicitly but higher winds affect c	0–6 km	0–4 km
Sensitive to fractal hodographs	No	No	Yes, needs prescription for smoothing hodographs

(greater than 50) because the storm-relative inflow kinetic energy is too small to prevent the cold-air outflow from undercutting the updraft and surging far ahead of the storm, the dynamic pressure-gradient forces associated with the midlevel vortices are too weak to promote storm splitting, and the updraft will not rotate as a whole because the storm-relative environmental winds are too weak in comparison to storm-induced winds.

Another parameter for forecasting storm type is the mean shear (Rasmussen and Wilhelmson 1983) or, equivalently, the arc length U_{S4} (m s^{-1}) of the hodograph curve between 0 and 4 km. (The mean shear is simply $U_{S4}/4000$ m.) Except for the 0–4-km restriction, U_{S4} is the parameter U_S introduced by Weisman and Klemp (1982, 1984) to characterize the shear magnitudes of the analytical hodographs, which they used in their sets of comparative simulations. As shown in section 5.2c, effects of shear are weak when $U_S \ll \sqrt{\text{CAPE}}$. Storms are forecast to be tornadic if the CAPE and mean shear are large. The mean shear suffers in practice because it is ill-defined for real-life (fractal) hodographs, it is independent of hodograph shape, and it can be large when the storm-relative surface wind is weak (Droegemeier et al. 1993).

Given observed or predicted storm motions, storm-relative helicity (SRH; Davies-Jones et al. 1990; Droegemeier et al. 1993) is a useful parameter for predicting whether updrafts will rotate cyclonically or anticyclonically as a whole. The helicity hierarchy (in a column of unit cross-sectional area) of the inflow layer of a storm translating with velocity $\mathbf{c}$ in a horizontally homogeneous nonrotating environment can be defined as $\bar{H}_{mn}(\mathbf{c}, h) \equiv \int_0^h [\nabla \times]^m[\bar{\mathbf{v}}(z) - \mathbf{c}] \cdot [\nabla \times]^n[\bar{\mathbf{v}}(z) - \mathbf{c}]dz$, where h is the nominal depth of the layer (usually chosen arbitrarily to be 3 or 2 km). Note that $\bar{H}_{01}(\mathbf{c}, h)$ is the storm-relative helicity; $\bar{H}_{00}(\mathbf{c}, h)/2h$ is the mean storm-relative kinetic energy per unit mass of the environment in the inflow layer and is related to BRNKE by BRNKE $= \frac{1}{2}\bar{H}_{00}(\bar{\mathbf{v}}_{0-6}, 0.5$ km). For a straight hodograph, $\bar{H}_{00}$ is symmetric, that is, it is the same for the severe left- and right-moving products of the split, while $\bar{H}_{01}$ is antisymmetric (the SRH of the SL storm is the negative of that of the SR storm). A mean-wind-relative helicity (MWRH) can be defined by substituting $\bar{\mathbf{v}}_{0-6}$ for $\mathbf{c}$. For a straight hodograph, MWRH is zero, which applies to the initial storm (no net updraft rotation), but not to the SR and SL storms individually. For highly curved hodographs, MWRH underestimates SRH only slightly. SRH is a linear function of both $\mathbf{c}$ and h. For fixed h, the contours of SRH as a function of $\mathbf{c}$ on a hodograph diagram are straight lines parallel to the shear vector from 0 to h. Thus the effect of different storm motions on SRH are readily apparent to a forecaster. For given $\mathbf{c}$, the variation of SRH from layer to layer can be found from a plot of $\bar{H}_{01}(\mathbf{c}, h)$ versus h. The biggest threat for tornadoes is associated with large environmental helicities in the lowest 1 km (Markowski et al. 1998a) because such helicities are converted into large vertical helicity densities at quite low altitudes within storm updrafts.

A nondimensional number similar to BRN can be obtained by dividing CAPE by SRH. High values of this number imply that the storm-relative environmental winds are negligible compared to the storm-induced winds. CAPE/SRH is not used in practice because CAPE can vary widely in proximity to storms, and violent tornadoes occur occasionally in warm-season, high-CAPE, low-shear (high BRN) environments. In fact, a threshold value of the energy-helicity index (EHI $\propto$ CAPE $\times$ SRH) fits the data (scatter diagrams of proximity values of CAPE and SRH for strong and violent tornadoes) far better than a threshold value of CAPE/SRH (Davies 1993a). How warm-season tornadic storms develop is not well understood because they are rarely observed in field projects and they have not yet been simulated successfully by computer models. It would seem that the large amounts of precipitable water in the highly unstable environment would result in heavy precipitation, excessive water loading, substantial evaporative cooling, and outflow-dominated storms. This often occurs, but not always. High CAPE could favor supercell formation in some cases. For instance, low-level inflow winds induced by intense updrafts may be sufficient to prevent the outflow from propagating ahead of the storm. Tilting and stretching of relatively weak environmental horizontal vorticity by a high-speed updraft may still result in a strong mesocyclone aloft. The high instability may give rise to an intense baroclinic zone just behind the gust front. The updraft can remain buoyant even after ingesting a large amount of rain-cooled air, allowing occluded mesocyclones to live longer than usual and to have more time to become tornadic.

All of the predictors that we have considered so far only predict the formation of supercells or mesocyclones aloft. Predicting a persistent low-level mesocyclone, the next step toward tornadogenesis, is more difficult because it involves forecasting the distribution of precipitation and rain-cooled air within the storm (Brooks et al. 1994b). If the mid- and upper-level storm-relative winds are weak, precipitation falls too near the updraft and rain-cooled air rapidly undercuts the updraft and occludes the mesocyclone. If, on the other hand, the mid- and upper-level winds are very strong, the precipitation falls too far downstream of the rotating updraft to be drawn around to the rear of the mesocyclone. Brooks et al. (1994a) went a step forward in considering a balance among midtropospheric storm-relative winds, SRH, and low-level mixing ratio. Another factor that also affects the inflow-outflow balance is the dryness of midlevel air, which is included only in the DCAPE (downdraft CAPE; Emanuel 1994, p. 172; Gilmore and Wicker 1998).

According to parcel theory, $\sqrt{2\,\mathrm{DCAPE}}$ is the maximum downward velocity that can occur in a given environment via evaporative cooling at constant pressure of relatively dry midlevel air to its wet-bulb temperature and then descent along a pseudoadiabat with just enough evaporation to keep the air saturated.

5.3. Tornadogenesis, maintenance, and decay

a. Mesocyclonic or type I tornadoes

We now are ready to address tornadogenesis, the stage that follows the development of near-ground rotation on the mesocyclone scale. Given now a complete vortex column in the updraft and strong low-level convergence that persists without interruption for, say, 10–15 min, a concentrated vortex (i.e., a tornado) should form as in a tornado simulator. The convergence associated with the updraft is enhanced by convergence in the swirling boundary layer of the mesocyclone; the boundary layer also provides an important feed of vorticity for vortex sustenance (section 5.4). Since "seed" vertical vorticity is already present near the ground, analysis of the vertical-vorticity equation always shows the dominance of the convergence term in a bull's-eye around the incipient tornado. Sometimes this is misinterpreted as evidence that the origin of the tornado's rotation is simply preexisting vertical vorticity.

The significance of strong low-level convergence to tornado formation is apparent from the following simple problem. Assume that uniform horizontal convergence $C = 5 \times 10^{-3}$ s^{-1} stretches an initial vortex of radius $R_0 = 1$ km with maximum tangential wind $V_0 = 10$ m s^{-1} into a tornado of radius $R_1 = 100$ m with maximum tangential wind $V_1 = 100$ m s^{-1} without any loss of angular momentum. What is the timescale τ for tornado formation? From the kinematic formula for divergence, $2d\ \ln R/dt = -C$, which has the solution $\tau = 2/C\ \ln R_0/R_1 = 920$ s $= 15$ min. Doubling the convergence to 10^{-2} s^{-1} reduces the time to 8 min.

The embryonic or fully developed tornadic vortex is detected on Doppler radar as a tornadic vortex signature (TVS; Brown et al. 1978), a region of large cyclonic shear between azimuthally adjacent sampling volumes in the field of Doppler velocities. The first TVS observed was that of an embryonic tornado initially detected at 3–4 km above the ground, near Union City, Oklahoma, on 24 May 1973 (see also Lemon et al. 1978). Over the course of 30 min, the TVS slowly extended downward, reaching near the ground coincident with tornado touchdown, and upward, reaching a height of 12 km. With only a few cases from research radars available to them, observationalists believed for several years that almost all large tornadoes formed first in the clouds in this way—labeled mode I tornadogenesis (Figs. 5.18a,b) by Trapp and Davies-Jones (1997)—enabling warnings to be issued roughly 20 min prior to their touchdown. Theoreticians, on the other hand, thought that tornadoes should build from the ground up (mode II tornadogenesis of Trapp and Davies-Jones 1997; Fig. 5.18c) because air with high angular momentum would approach the axis of rotation faster in the mesocyclone's boundary layer than above it (Rotunno 1986). Since the installation of the WSR-88D network across the United States, it is now realized that ~50% of tornadoes apparently form either very close to the ground or almost simultaneously in a column in the lowest 2 km, within 5–10 min (Trapp et al. 1999). Since the WSR-88Ds take 5 min to complete a volume scan, these mode II resultant tornadoes often develop with little advance warning. There is little difference between the mean intensities of mode I and mode II tornadoes.

Trapp and Davies-Jones utilized numerical and analytical models of an idealized mesocyclone to provide simple explanations for both modes of tornadogenesis. A time-dependent version of the Burgers–Rott vortex due to Rott (1958), in which the circulation at infinity and the convergence are both constant with height, provides an example of the mode II genesis. High-angular-momentum air approaches the axis at the ground and aloft simultaneously. The vortex in this case forms as a cylindrical column that is independent of height. If neither the radial inflow nor the circulation increases with height, and one or both of them has a maximum at the ground, the vortex will form from the ground up. If the radial inflow and the circulation are both nondecreasing, and one of these parameters increases with height, the high-angular-momentum air arrives near the axis first aloft and mode I genesis ensues. If the low-level rotation is insufficient, the vortex remains aloft (Smith and Leslie 1978). Otherwise the vortex develops downward via a bootstrap process called the dynamic pipe effect (Leslie 1971; Smith and Leslie 1979). As demonstrated in section 5.4d, the vortex core is in cyclostrophic balance and is stable to radial displacements so that air is prevented from entering the vortex through its sides. In this respect the vortex acts like a suction tube with solid walls. As air is drawn into the lower end of the vortex, it spins faster, centrifugal forces increase and balance the inward pressure-gradient force. This air then becomes part of the dynamic pipe. The vortex builds itself down by this process until it makes contact with the ground.

The mechanisms just described do not explain those tornadoes that develop outside the mesocyclone's central axis, that is, tornadogenesis within two-celled mesocyclones. A two-celled vortex is characterized by downflow along the central axis, terminating in low-level radial outflow that turns vertical in an annular updraft at an outer radius (see section 5.4). Radar observations of two-celled mesocyclones have been

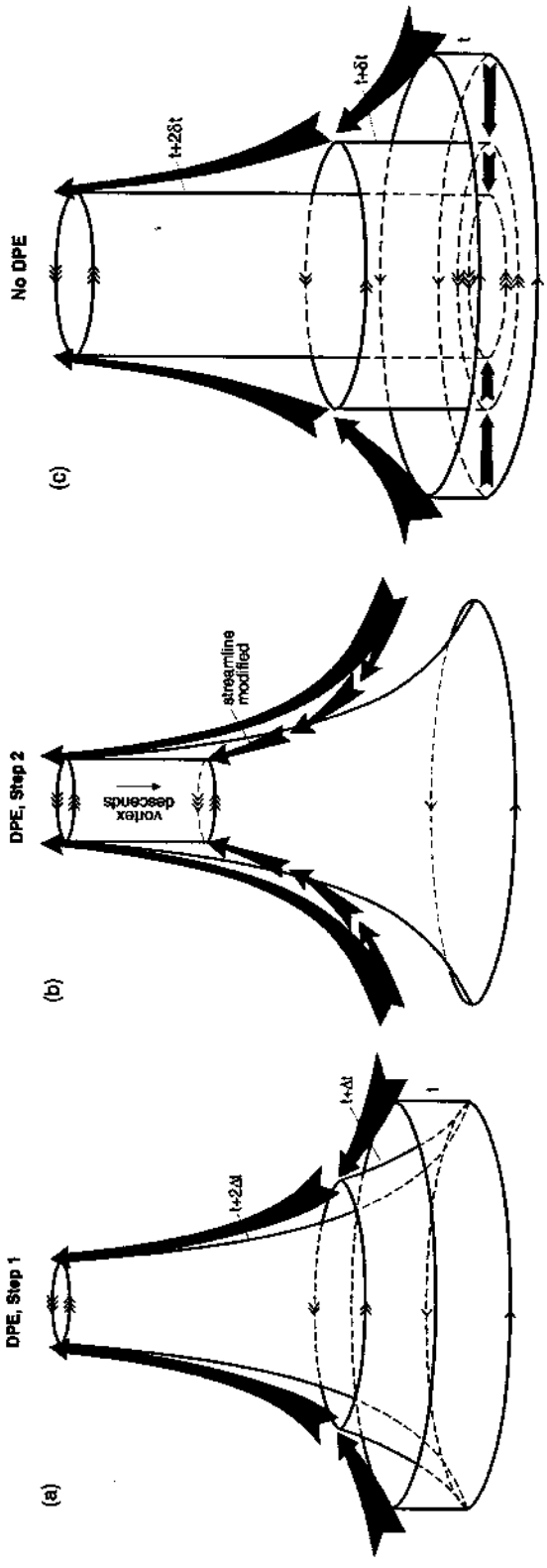

FIG. 5.18. Idealization of two modes of vortex formation within a rotating updraft (Trapp and Davies-Jones 1997). (a) and (b) illustrate the dynamic pipe effect. In (a) the radial inflow increases with height so an initial cylindrical vortex tube is stretched into a cone and a funnel cloud forms aloft first. In (b) the vortex pipe builds downward by increasing the radial inflow into its lower end through a suction effect as described in the text. The vortex descends to the ground relatively slowly. In (c) the radial inflow is constant with height so the DPE is absent. The initial cylindrical vortex tube remains cylindrical as it is stretched vertically so that the vortex spins up simultaneously at all heights, resulting in rapid tornado formation.

reported by Brandes (1978) and more recently by Wakimoto et al. (1998) and Trapp (1999); visual evidence is provided in Bluestein (1985b). Brandes (1984a) confirmed observationally that the VPPGF may become negative in the vicinity of tornadic mesocyclones as the vertical vorticity in the low-level mesocyclone exceeds that in the midlevel mesocyclone. As also demonstrated in a numerically simulated storm by Klemp and Rotunno [(1983); and in subsequent storm observations with airborne Doppler radar, by Wakimoto et al. (1998)], adverse pressure-gradient forces cause downward motion in what has become known as an "occlusion downdraft," which often (though not always; Wakimoto and Cai 2000) precedes tornado formation.

The two-celled vortex is susceptible to a cylindrical vortex-sheet instability (Rotunno 1984). In analogy with the formation of satellite vortices around large tornadoes, the release of this instability in the parent mesocyclonic vortex leads to the formation of submesocyclone-scale vortices outside the central downdraft, in an annular region where both vertical velocity and its radial gradient are positive (Fig. 11 of Rotunno 1984). Tornadogenesis occurs if one or more of these smaller-scale vortices interacts with the ground and consequently contracts into tornadoes (Rotunno 1986). It is unclear how often such a mechanism may be active, however: The percentage of all tornadoes that develop out of two-celled mesocyclones is unknown, as is the percentage of all mesocyclones that become two-celled some time during their life cycle (Trapp 1999).

The genesis of type I tornadoes is often associated with the interaction of the parent supercell with a preexisting thermal boundary such as a storm outflow boundary or a warm or stationary front. A recent study suggests that 66% of the significant (F2 or greater) tornadoes in the VORTEX-95 domain occurred near some type of low-level boundary not associated with the parent storm itself (Markowski et al. 1998b; see also Rasmussen et al. 2000). Storm–boundary interactions may affect low-level rotation (and presumably tornadogenesis) as follows: (i) horizontal streamwise vorticity, baroclinically generated within the thermal boundary, is ingested by storms with inflows along the boundary, and subsequently is vertically tilted in the downdraft and updraft and stretched in the updraft (Markowski et al. 1998b; Atkins et al. 2000); and (ii) vertical vorticity owing to cross-boundary horizontal variations in the boundary layer wind profile is vertically stretched as the storm's updraft encounters the boundary (Maddox et al. 1980). Note that convergence along a boundary may also cause a deviant storm motion that in turn affects the updraft's rotation.

Before leaving the discussion of type I tornadogenesis we note that, according to airborne Doppler radar data collected during VORTEX, not all instances of a low-level mesocyclone with persistent, low-level convergence result in a tornado. Such lack of tornado formation, subjectively classified as "tornadogenesis failure" by Trapp (1999), may among other reasons have been due to a thin (tens of meters), surface-based, yet unobserved layer of low angular-momentum air imparted to the mesocyclone (Lewellen et al. 2000). Surface-layer inflow of low angular momentum air increases, for example, with an increase in effective surface roughness, or an increase in the translation speed of the mesocyclone. When a "local corner flow swirl ratio" (see section 5.4)—which is inversely proportional to such depletion of angular momentum air in the surface layer—is prescribed below some critical value in Lewellen et al.'s numerical model, only very little vortex intensification, well off the lower surface, occurs.

Long-lived tornadoes typically evolve through the following five stages. The tornado is first visible as dust swirling upward from the surface and a short funnel pendant from cloud base (the *dust whirl stage*). It then goes through an *organizing stage* where its funnel descends and it intensifies. In its *mature stage* it reaches maximum intensity and its funnel reaches its greatest width and is almost vertical. The baroclinic or barotropic mechanisms provide a constant feed of vorticity to the tornado, as does horizontal vorticity generation above the no-slip ground (e.g., Trapp and Fiedler 1995), which may explain how some tornadoes can remain in the mature stage for a considerable time. During its *shrinking stage,* it decreases in width and becomes more tilted. It may still be extremely damaging. In its *decay stage* the tornado dies as a result of its base being overtaken by a divergent cool downdraft and its circulation weakening. It is no longer able to resist the shear of the surrounding flow, and so becomes tilted over and greatly stretched into a rope shape as its top travels with the updraft and its base is moved in a different direction by the low-level outflow. Although its circulation has decreased significantly, its winds can still be high in a small area because its core radius is also much reduced. Thus the tornado can still be very destructive over a narrow path. The funnel finally undergoes wavelike contortions, with parts of it disappearing and reappearing, before it finally dissipates. This behavior suggests that the tornado decays by becoming unstable to sinusoidal long-wave displacement of its axis. A few intense tornadoes have tracks that widen at the end, suggesting that they decayed by spreading out and becoming diffuse as their parent updraft weakened abruptly (Agee et al. 1976).

A cyclic repetition of this tornado evolution within a single supercell has been documented on numerous occasions. Indeed, Fujita (1963) and Darkow (1971) noticed that roughly 20% of tornadic supercell storms spawned tornadoes periodically, thus producing "tornado families." The median interval between tornadoes was 45 min. Ward and Arnett (1963) observed

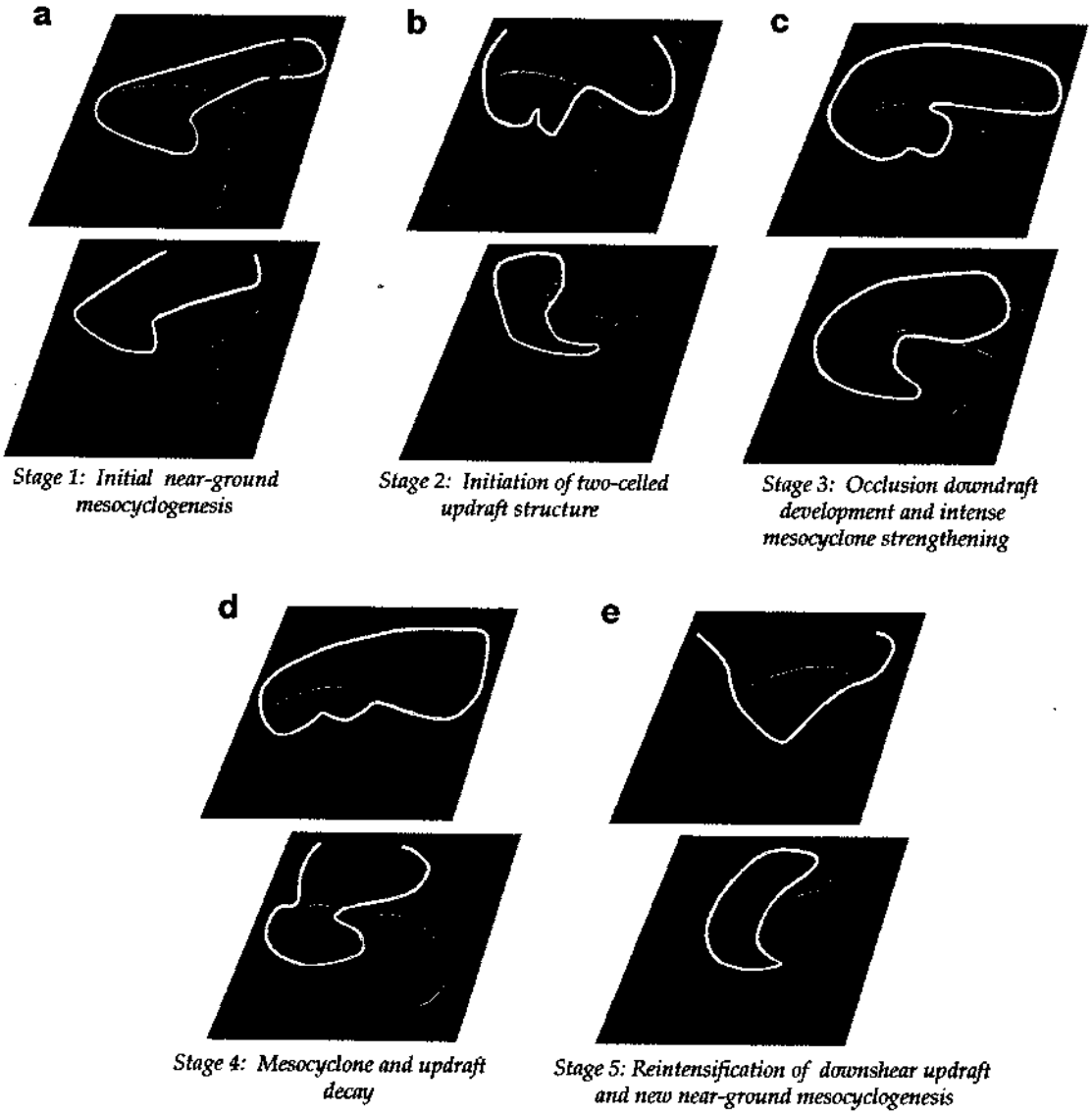

FIG. 5.19. Five-stage conceptual model of the cyclic genesis of mesocyclones. The surface cold-pool boundary is shown by the scalloped black line. Red marks vorticity maxima. Updraft and downdraft are shown in light and dark blue, respectively. The boundary of the rain area is outlined by the yellow contour (Adlerman et al. 1999).

that supercell storms generated periodic surges in outflow with an average cycle of 50 min. Forbes (1978) studied the hook echoes and tornado tracks associated with cyclic supercells during the massive tornado outbreak on 3 April 1974. Most of the tornadoes turned to the left before dissipating. Burgess et al. (1982) showed, from Doppler radar observations, that about one-quarter of supercells produced more than one mesocyclone with a roughly 40-min interval between successive formations.

The initial mesocyclone in a cyclic supercell is typically the longest lived (90 min). In numerical simulations (Fig. 5.19), this mesocyclone forms first at midlevels owing to the tilting of streamwise environmental vorticity, and then ~30 min later at low levels owing to tilting and stretching of baroclinic vorticity in the rear-flank downdraft and in the updraft (Adlerman et al. 1999; see section 5.2). The mature stage of the first cycle is marked by strong rotation through a large depth (from 0 to 7 km or higher), tangential velocities ~25 m s^{-1}, circulation ~5 × 10^5 m^2 s^{-1}, and low-level convergence ~5 × 10^{-3} s^{-1}, and lasts around 40 min. Subsequent mesocyclones are shorter lived (45 min) and have mature stages that last only 20 min. However, the near-ground rotation develops within 9 min of the beginning of the new cycle. According to Adlerman et al., the mechanism for subsequent near-ground mesocyclogenesis is identical

to that of the initial near-ground mesocyclogenesis; it simply proceeds more rapidly because cold air residual from the previous cycle lends to a buoyancy gradient orientation that is ideal for horizontal baroclinic vorticity generation. These mesocyclones typically decay in around 15 min as their height, radius, tangential winds, and circulation decrease, and the flow around them becomes divergent. Tornadoes touch down midway through the mature stage at a time when the downdraft is intensifying, and dissipate during the decay stage as the updraft is undercut near the surface by subsiding air. Burgess et al. proposed (and Adlerman et al. verified) that, as the previous mesocyclone and tornado are being occluded by cold outflow, a new mesocyclone and tornado develop on the gust front ahead of and to the right of the old mesocyclone. The old mesocyclone is weakened aloft since its associated updraft now draws air with lesser moist entropy, but it may still contain a tornado that is displaced by the new outflow to the rear side (instead of the base) of the main storm tower. Jensen et al. (1983) reported visual observations of a storm that corroborates this model.

A somewhat different evolution is revealed by a recent analysis of VORTEX data. Dowell and Bluestein (2000) used airborne Doppler radar to characterize as "inflow dominated" the cyclic supercell that produced a series of tornadoes (one of which was a long-lived F4 tornado) that formed in the Texas panhandle on 8 June 1995 (see Fig. 5.20). They concluded that individual tornadoes were not kinemat-

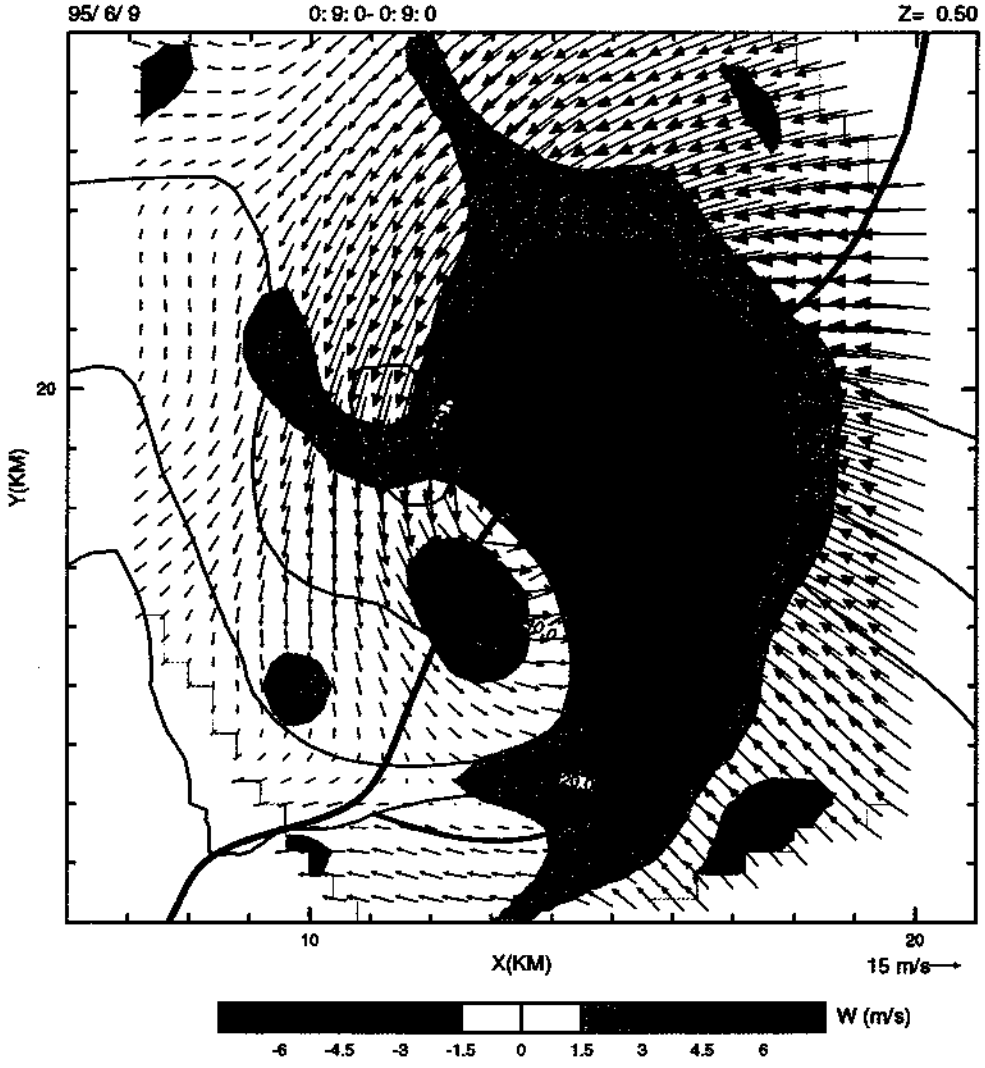

FIG. 5.20. Storm-relative horizontal wind vectors, vertical velocity (shaded), and radar reflectivity factor (contoured), derived from airborne Doppler radar data of the tornadic storm near McLean, Texas, at 0009 UTC 9 June 1995. The analysis level is 500 m AGL, and the domain is relative (in km) to McLean, Texas. The black line denotes the rear-flank gust front position, and the curvy line, the tornado track. "T4" is the location of the fourth tornado in the family of tornadoes observed on this date. Courtesy of D. Dowell.

ically occluded, as in the aforementioned "outflow-dominated" model, but rather were advected rearward, away from the updraft, by strong, low-level, front-to-rear storm-relative inflow.

These conceptual models explain why the damage tracks of tornadoes in a family are often a series of parallel arcs that are staggered to the right as one track ends and the next one in the series begins. The cyclic process does not always conform to these models, however. For instance, the old and new mesocyclones revolve partly around each other if they are close together, because of the velocity induced on each vortex by the other one (Brown et al. 1973). A film of the Hesston, Kansas, tornadic storm of 13 March 1990 showed the Hesston tornado in its rope stage moving into the condensation funnel of a newly formed large tornado.

b. Nonmesocyclonic or type II tornadoes

As stated in the introduction, a type II tornado forms along a stationary or slowly moving front or windshift line apparently from the rolling-up of the associated quasi-vertical vortex sheet into individual vortices; these vortices, which at times may be classified as "misocyclones"—for our purposes tornado-parent vortices that by definition have diameters < 4 km (Fujita 1981)—then are vertically stretched by convective updrafts under which the vortices move or over which they develop (Fig. 5.21). The horizontal shearing instability mechanism has been proposed to explain the formation of lines of dust devils, by Barcilon and Drazin (1972); waterspouts in cloud lines along the sea-breeze front and weak tornadoes in flanking lines, by Davies-Jones and Kessler (1974) and Davies-Jones (1986); and landspouts, by Brady and Szoke (1989) and Wakimoto and Wilson (1989). According to Lee and Wilhelmson (1997), the release of the horizontal shearing instability leads to first-generation vortices that interact and merge to create the misocyclones within which landspouts ultimately develop. We note that the presence of a spiral rain curtain (or hook echo on radar) close to waterspouts (Golden 1974a,b) and landspouts (Wakimoto and Wilson 1989; Wilczak et al. 1992; Wakimoto and Martner 1992) suggests that the vorticity of type II tornadoes may be augmented by the baroclinic process that plays an important role in type I tornadogenesis (see section 5.2). Indeed, Wilczak et al. (1992) provided evidence that the vertical tilting of baroclinically generated, streamwise horizontal vorticity was important in the generation of the low-level rotation of a nonmesocyclone tornado on 2 July 1987 in northeastern Colorado. In this regard, the proximity of a nontornadic storm to an apparent type II tornado may muddle the mechanisms responsible for the tornado as well as the characterization of the tornado type itself. This statement is illustrated in the dissimilar discussions by Wakimoto and Atkins (1996) and later by Ziegler et al. (2001) of the origin and nature of the F3 tornado observed during VORTEX on 29 May 1994.

Waterspouts and landspouts are generally cyclonic because the vorticity of the preexisting windshift line is usually cyclonic owing to the earth's rotation. They typically have circulations of 2×10^3 to 10^4 m^2 s^{-1}. Consider, for example, a straight boundary or front within which resides an infinite number of vertical vortices that are spaced 3 km apart. If the vortices are associated with a cross-front difference in the along-front wind component of $\Delta u = 6$ m s^{-1}, the circulation available to each vortex is $\Gamma \equiv \oint_c \mathbf{u} \cdot \mathbf{ds} \cong \Delta u \Delta s \approx 2 \times 10^4$ m^2 s^{-1}, where $\Delta s = 3$ km is the along-front length of the circuit around one of the vortices; the cross-front wind component (relative to the vortex sheet) does not contribute to circulation. This value is small compared to the circulation of the average mesocyclone (say, 5×10^4 m^2 s^{-1}), but the merger of several misovortices could lead to a sizable circulation.

In some instances the tornado forms from a cumulonimbus that develops rapidly above a convergence zone associated with two colliding boundaries (such as an outflow boundary emanating from another storm and a sea-breeze front; Holle and Maier 1980). Note,

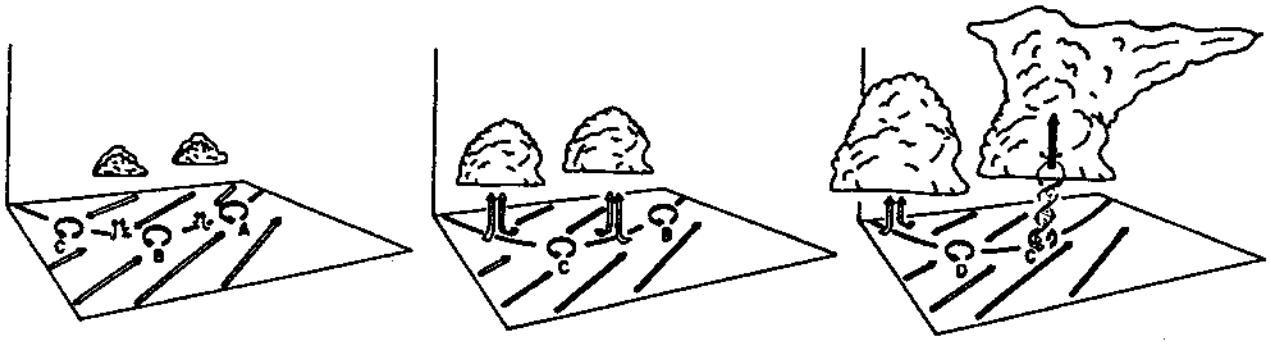

FIG. 5.21. Diagram showing genesis of a nonmesocyclone tornado (Wakimoto and Wilson 1989). Misoscale vortices (identified by letters) form along a windshift line (black line) as a result of shearing instability. A tornado results from one of these vortices (C) being stretched by overhead convection.

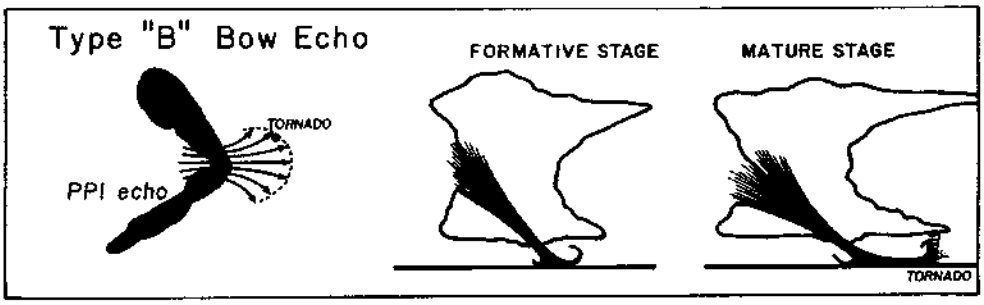

FIG. 5.22. Tornado formation within a bow echo according to Fujita (1985). Note the location of the tornado on the left side of the strong outflow.

however, that colliding outflows are far more common than tornadoes, implying that type II tornadoes require either a fortuitous or a physically intentional coincidence of maxima in vertical velocity and vertical vorticity. Regarding the latter, incipient type II tornadoes may form at the intersections of the windshift line and the ascending branches of the circulations of boundary layer rolls. In this case, coincidence of vortex and convective updraft is established immediately since convective initiation tends also to be favored at line–roll intersections (Wilson et al. 1992). Alternatively, the "locational relationship" between the incipient tornado and the updraft may be due to the influence of the vortex itself on the low-level convective forcing, which, therefore, precludes the need for a line–roll intersection (Lee and Wilhelmson 1997).

Squall-line tornadoes occur in lines devoid of supercells as well as in supercells within lines. The nonsupercell variety quite frequently form in conjunction with high straight-line winds in short lines or line segments with bow-shaped radar echoes. As indicated in Fig. 5.22, cyclonic tornadoes may occur on the cyclonic side of the jet of strong outflow winds. Assuming that the environmental shear is westerly, the cyclonic (anticyclonic) vorticity on the north (south) side of the jet probably originates from a combination of the baroclinic mechanism described in section 5.2 and downward momentum transport (or, equivalently, tilting of horizontal barotropic vorticity). Tornadoes may also occur anywhere along a still quasi-linear convective system, apparently via the vertical vortex sheet roll-up mechanism, and within the system's cyclonic "bookend" vortex (Pfost and Gerard 1997; Trapp et al. 1999).

5.4. Tornado structure

Investigations of the tornadic vortex itself—particularly via laboratory simulators or numerical models thereof—typically idealize it as a nontranslating vortex in an axisymmetric near environment extending out to about 1 km from the axis (Lewellen 1993); analyses of tornado observations often employ azimuthal averaging techniques yielding comparable idealizations. Within this axisymmetric setting, the tornado may be asymmetric in three-dimensional models if it has a multivortex structure. In actuality, even a single-vortex tornado is asymmetric because it moves across the ground in response to a steering current, because its inflow—when visible in blowing dust/patterns on a water surface or observed by radar—appears to be concentrated in a spiral band (Fig. 5.23; see also Bluestein and Pazmany 2000), and because it tilts with height. Even though a mature tornado may be quite erect near the ground, the TVS on radar generally has an overall tilt of about 25° toward the left forward side of the storm (Brown et al. 1978).

The idealized axisymmetric tornado is conveniently divided into five strongly interacting regions (Fig. 5.24): the vortex core (Ia), the outer flow at radii outside the core (Ib), the boundary layer (II), the corner region where inflow in the boundary layer turns the corner and enters the core from below (III), and the flow aloft that caps the vortex within the parent cloud (IV) (Lewellen 1976, 1993; Snow 1982; Davies-Jones 1986). Prior to describing these regions and their inherent dynamics, we provide critical comments on a representative sample of the different means with which tornado structure has been deduced: by laboratory simulations, numerical simulations, and direct and remotely sensed observations. Thereafter, the dependence of tornadic vortex behavior and structure on flow parameters is discussed, as are some of the more significant measurements made in tornado simulators.

a. Comments on laboratory simulations of tornadoes

Although their use has declined significantly in recent years due mostly to cost (see Doswell and Grazulis 1998), tornado simulators have provided a wealth of information about tornado structure (see reviews by Davies-Jones 1976, 1986; Maxworthy 1982; Wilkins 1988; Church and Snow 1993). The Ward-type vortex generator (Fig. 5.25) replicates a wide range of tornadic vortices and reproduces observed surface pressure profiles of tornadoes (Ward

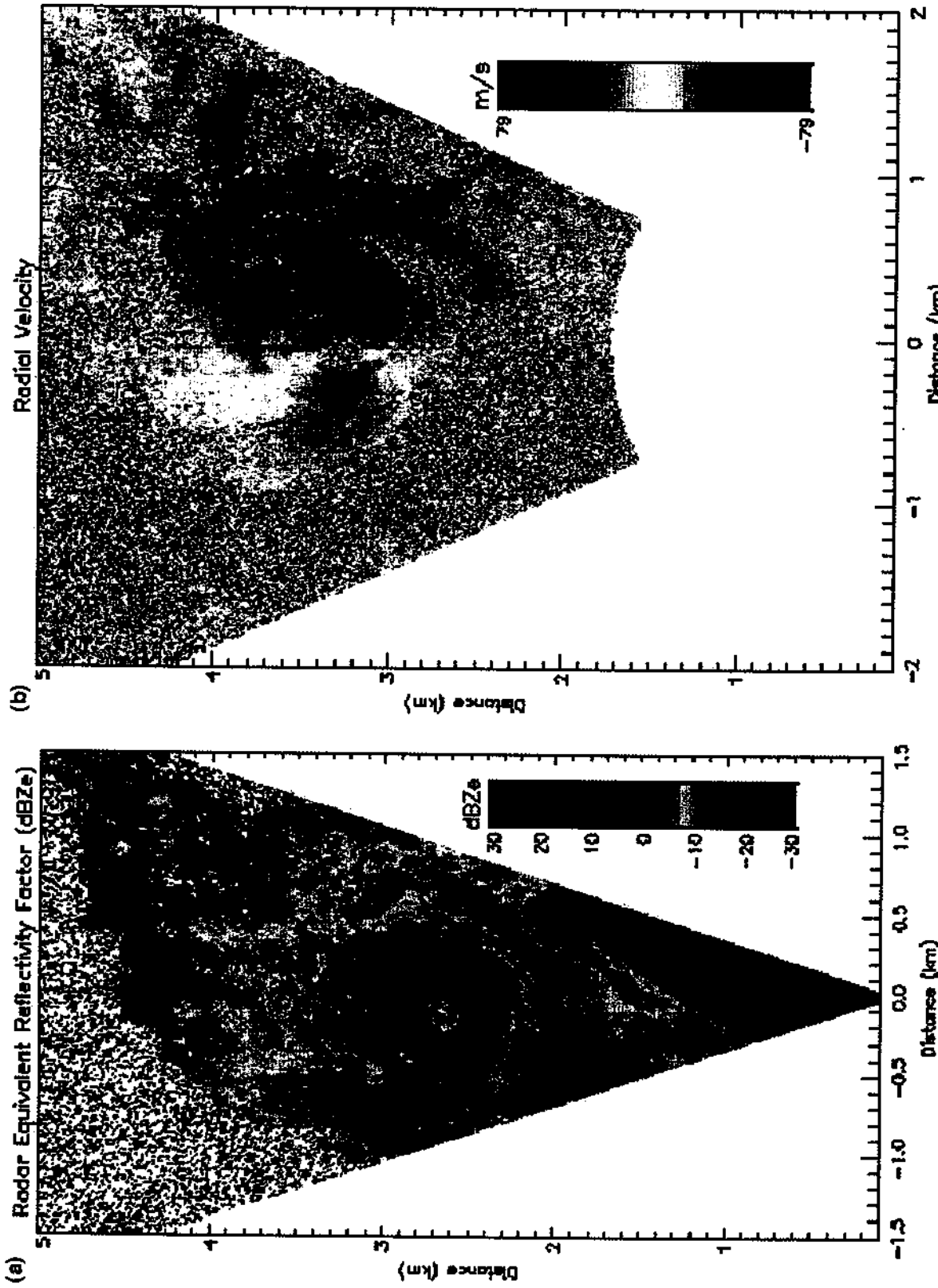

FIG. 5.23. Data collected by the University of Massachusetts, Amherst, 3-mm wavelength radar of an F-3 tornado near Verden, Oklahoma, on 3 May 1999. (a) Radar reflectivity factor, at 2254:57 UTC. (b) Doppler velocity, at 2255:53 UTC. Courtesy of A. Pazmany and H. Bluestein.

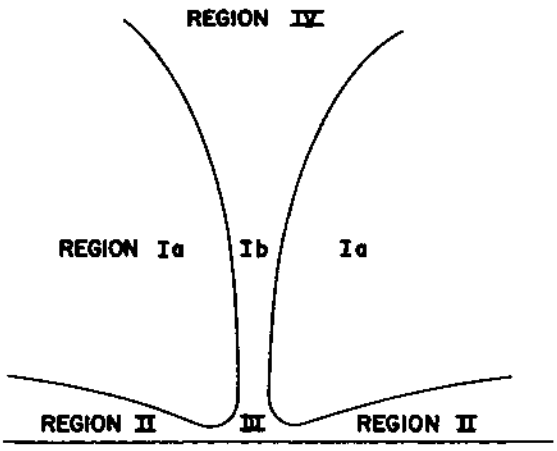

FIG. 5.24. Different flow regions of a tornado (adapted from Lewellen 1976). Region Ib is the core, II is the boundary layer, Ia is the region above the boundary layer outside the core, III is the corner region, and IV is the termination region within the parent storm at mid- or high altitudes.

1972; Church et al. 1977; Church and Snow 1993). The Ward model is more relevant to tornadoes than most other vortex chambers because it allows descent of initially nonrotating fluid in the core and because it is geometrically and dynamically similar to tornado-producing flows. In particular it has an aspect ratio, $a \equiv h/r_0$, where r_0 is the radius of the updraft hole and h is the height of the inflow to the updraft, that is of order 1, which is characteristic of tornadic thunderstorms; many other simulators have high aspect ratios. The flow in the apparatus is governed to a considerable extent by a single parameter, the swirl ratio, defined by $S \equiv r_0 M/2Q$ where $2\pi M$ is the circulation at the edge of the updraft ($M = vr$) and $2\pi Q$ is the volume flow rate of the updraft ($Q = \int_0^r wr'dr'$) (Davies-Jones 1973, 1976). The swirl ratio can also be expressed by $S \equiv v_0/\bar{w}$, where v_0 is the tangential velocity at the edge of the updraft and $\bar{w}$ is the mean vertical velocity through the updraft hole. It is tempting to scale up measurements made in the Ward-type simulator to obtain estimates of tornado wind speeds and pressure drops. These estimates must be treated with some skepticism, however, because the updraft radius in the simulator is artificially constrained instead of being able to adjust to increases in circulation (Maxworthy 1982); the vortex is terminated aloft artificially by the honeycomb baffle, which can have a large effect on vortex size and structure (Smith 1987); the stagnation pressure of the air that descends along

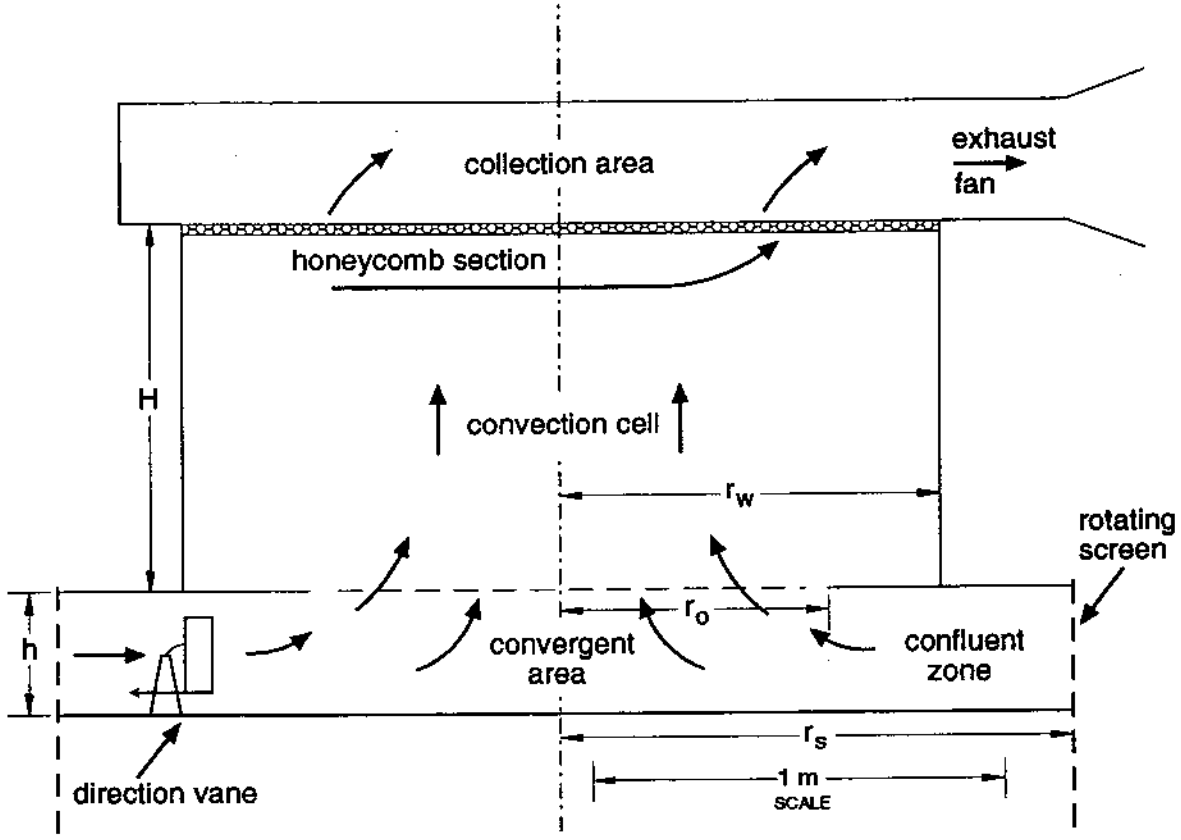

FIG. 5.25. Ward's tornado simulator.

the axis from above the baffle is unknown; the flow is driven mechanically instead of by buoyancy; there is no warming in the core when subsidence occurs there; and the Reynolds number is low compared to atmospheric values, resulting in flows that are partly laminar at some settings of the external parameters.

b. *Comments on numerical simulations of tornadoes*

Although three-dimensional cloud models have not yet been used successfully to routinely simulate actual storms, they do reproduce many of the features of tornadic storms and even generate "tornado-like vortices" (e.g., Wicker and Wilhelmson 1995; Grasso and Cotton 1995). The origins of these vortices can be revealed by diagnoses of the numerical results. To produce a bona fide tornado, the cloud-model characteristics must include an innermost grid with a grid-point spacing of 10 m or less in the horizontal and the same in the vertical near the ground; realistic two-way interaction between the grids; lower boundary conditions that are representative of the interaction of the turbulent flow with the ground; and a realistic turbulence parameterization that includes effects of rotational damping. Because these requirements are rather daunting (see Wilhelmson and Wicker's chapter in this volume), many investigators have turned their attention to numerical models either of the tornado simulators or of a tornado in an axisymmetric setting; our subsequent discussion focuses on such models.

With the exception of the Lewellen and Sheng (1980) turbulent model of the Purdue University simulator, all known models of tornado simulators have assumed laminar flow and simplified the geometry of the simulator to a cylinder. The main difficulty with modeling the tornado simulator lies in formulating an appropriate top boundary condition for representing the influence of the honeycomb baffle on the flow; the other boundary conditions are well established. The obvious choices for the lower boundary are either a no-slip or a free-slip solid surface (e.g., Rotunno 1977, 1979). Symmetry conditions are imposed at the axis if the flow is axisymmetric; for asymmetric flow in a three-dimensional model it is convenient to place around the axis a narrow impervious free-slip cylindrical inner boundary (Rotunno 1984). The outer cylindrical boundary is open as an inlet up to the height h of the top of the inflow layer, above which the outer boundary is impermeable and free slip. The radial and tangential velocities of the swirling inflow entering through this boundary are typically assumed to be constant with height. Rotunno (1977) realized that the largely irrotational flow observed in the simulator was reproduced better when the third inlet condition was zero azimuthal vorticity, $\eta \equiv \partial u/\partial z - \partial w/\partial r$, rather than zero vertical velocity as imposed by Harlow and Stein (1974).

As mentioned, the top boundary is problematic. In none of the known models is the baffle explicitly incorporated into the computer model domain. Therefore, the top boundary must correspond to the lower surface of the baffle, which we define to be at $z = H$. Assuming that it completely removes the radial and swirling components from the flow and has negligible resistance to vertical flow, the baffle has two effects. First, fluid reenters the apparatus from above with no initial rotation so an appropriate inflow boundary condition at the top is $v = 0$. Second, the radial distribution of pressure on the upper side of the baffle is quite uniform over the outflow portion because of the removal of the horizontal components from the flow. Making the simulator's convection cell deep simplifies the formulation of the top boundary conditions because the throughflow is practically vertical by the time it reaches the top and the baffle. The baffle's role of eliminating the radial flow is then redundant and we can make the first boundary condition $u = 0$ at the top. This implies from continuity that $\partial w/\partial z = 0$ at $z = H$, which is not an independent condition. In some simulations, $v = 0$ or $p =$ constant has been applied across the entire top. These boundary conditions clearly do not apply to the underside of the baffle. Since $u = \partial w/\partial z = 0$ at $z = H$, imposing zero radial viscous force, that is, $\partial \eta/\partial z = 0$, seems a reasonable choice for the second condition, especially since it is equivalent to imposing cyclostrophic balance there. It is also equivalent to $\partial^2 u/\partial z^2 = 0$ since $\partial^2 w/\partial r \partial z = 0$ from the first condition. A third independent condition is $v = 0$ for inflow, as reasoned above, and $\partial v/\partial z = 0$ for outflow, which is consistent with vertical throughflow and near conservation of angular momentum along streamlines below the top. These are close to the conditions used by Rotunno (1977, 1979), who did not distinguish inflow from outflow and so did not impose zero rotation on inflow through the top. Therefore his model is probably the most relevant to flow in the simulator.

In open boundary, limited-domain models of the tornado itself (e.g., Smith and Leslie 1979; Howells et al. 1988; Walko 1988; Lewellen et al. 1997), the effects of the larger-scale flow are represented through the lateral boundary conditions, where swirling inflow is imposed, and also through the top boundary conditions if the model height does not extend into the stratosphere. Apparently, all such models have at least one of the following artificial features: porous lids at low heights with dubious boundary conditions imposed, prescribed eddy viscosity, homogeneous fluids with fixed body forces in lieu of buoyancy forces, parameterized subsidence warming in lieu of a reservoir of overlying potentially warm air that the vortex can draw downward, and the anelastic assumption. Eliminating all these constraints even in an axisymmetric model would require a large amount of computing resources.

Lewellen et al. (1997) have developed a sophisticated three-dimensional large-eddy simulation model (the subgrid model of which now includes the effects of rotational damping; see Lewellen et al. 2000) with open boundaries to investigate the turbulent interaction of the tornado vortex with the surface. The Lewellen et al. model has been successful in improving the quantification of the processes in the corner region that yield the largest tangential velocities in the flow (Lewellen et al. 2000). It has a rather limited domain size of 1 km × 1 km × 2 km in the x, y, z directions, respectively, to allow resolution of the large turbulent eddies. Gridpoint spacings of 1.5 m in the vertical and 2.5 m in the horizontal are attained by grid stretching; Lewellen et al. (1997) conclude that such resolution in their model is sufficient so that the time-averaged velocity and pressure distributions in the turbulent corner region show little sensitivity to either finer resolution or a modified subgrid turbulence model. A 1-km diameter, uniform upward vertical velocity (one of a number of possible conditions) is prescribed at 2 km above the ground. Hence, although axial downdrafts can still occur, they are severely limited in extent.

Lewellen et al.'s model design restrains the interaction of the vortex with the "storm" to be one way. Fiedler's (1995) valid criticism of such open boundary, limited-domain modeling is as follows: The vortex is not allowed to adjust as a result of axial downdrafts developing in response to the surface low. For example, a vortex breakdown might enter the domain from above, descend to the surface, and eliminate the supercritical vortex (see section 5.4d) altogether. Fiedler's (1993, 1994) remedy to this problem has been a closed-domain modeling approach. This approach is not without its own limitations, however. He imposes in his model a body force that has maximum strength at the midpoint of the axis and is supposed to simulate buoyancy in the parent updraft, in lieu of or in addition to an entropy equation with advection and diffusion terms. Since the body force is unrealistically immutable, a mutual interaction between buoyancy field and the vortex is precluded. Also unrealistic is the instant loss of parcel "warmth" as a parcel leaves the fixed region of the body force. The domain is a closed rotating rank of radius r_0 that is large enough so that it is effectively infinite (i.e., the results have become insensitive to r_0). Since the flow is closed, the kinetic energy would increase without bound in the nonrotating, inviscid limit owing to production of kinetic energy each time parcels cycled through the body force region. The viscosity near the top of the tank is increased by an order of magnitude so that the vertical velocity at steady state is less than $(2\ \mathrm{CAPE})^{1/2}$, which is the vertical velocity a parcel would acquire, if there were no VPPGF, in proceeding upward along the axis once through the body force region. In the inviscid limit with rotation, there is an exact solution consisting of a vortex in hydrostatic and gradient-wind balance with no meridional motion. For a body force like Fiedler's that for all practical purposes does not extend to the boundaries, this solution satisfies free-slip boundary conditions at top and bottom. Hence, the free-slip viscous solution tends to a steady state consisting of a wide vortex in gradient-wind and hydrostatic balance and an outer region of weak meridional flow that largely avoids the region of the body force altogether.

In both types of models, a critical effect of the lower boundary condition on the vortex structure is exhibited, as has been demonstrated by Rotunno (1977), Howells et al. (1988), Fiedler (1993), and others. Indeed, the use of a frictional lower boundary affords the development of a rotating boundary layer, the existence of which (at sufficiently high Reynolds number and swirl ratio) has implications on high tornadic wind speeds (see section 5.5).

As mentioned, a limited-area model of a tornado should include a realistic updraft driven by buoyancy forces associated with latent heat release in a conditionally unstable atmosphere. It should also extend into the stratosphere so that the vortex can terminate naturally in radially divergent flow and is exposed to overlying potentially warm air, which could be drawn down into the core and undergo compressional warming. One such model exists (Walko 1988), but the size of the domain is too large to permit a large-eddy simulation. He used a prescribed eddy viscosity instead. He showed that subsidence in the core of an intense tornado can extend practically to the ground. Unfortunately the model is anelastic, meaning that variations in density, ρ', from ambient density, $\rho_a(z)$, are neglected in all terms except when multiplied by the gravitational acceleration (i.e., $\rho' g$ is retained). In the region of high tangential winds in a tornado, the centrifugal acceleration, v^2/r, is many times g. For example, $v^2/rg \approx 10$ for $v = 100$ m s^{-1}, $r = 100$ m. For a potential vortex the ratio of accelerations decreases as r^{-3} so the "radial buoyancy acceleration" $(\rho'/\rho_a)v^2/r$ is significant compared to the normal vertical acceleration due to buoyancy, $-\rho' g/\rho_a$, out to a distance of 350 m from the axis in the above example. The "radial buoyancy" effect, which enhances the stability of the vortex, is not included in an anelastic model, which therefore may not simulate accurately the trajectories of air parcels in and near the core.

c. *Comments on tornado observations*

Photogrammetry, aerial surveys of tornado damage, in situ measuring devices, and remote-sensing techniques comprise the means by which vortex structure has been deduced from tornadoes observed in nature. Consider aerial damage surveys, a practice pioneered by Fujita. These have been used to determine if the damaging winds were straight-line or vortical, and if

multiple vortices were present (Fujita and Smith 1993; Fujita 1993); the existence of suction vortices that attend some tornadoes was suggested on the basis of such surveys. As inherent also in F-scale determination (see section 5.1), information from aerial surveys is necessarily limited by the type of ground cover and structures in the tornado's path.

Portable devices have been designed to make in situ measurements of tornado properties typically near the ground only. These devices are placed in the projected path of a tornado; their success is bound by the potentially complicated and hazardous deployment logistics. TOTO (totable tornado observatory; Bedard and Ramzy 1983; Bluestein 1983a,b; Burgess et al. 1985), equipped with wind and thermodynamic property sensors, was used only during the early and mid-1980s. Data were collected in mesocyclones, but unfortunately never in a mature tornado: Deployment logistics were complicated further when it was determined that unless TOTO were staked down, it could tip over at F1 wind speeds. "Turtles" (Brock et al. 1987) consist only of temperature and pressure sensors encapsulated in heavy concave shells; as the instrument name implies, the aerodynamic design of turtles allows them to withstand higher wind speeds. The strategy during VORTEX was to deploy an array of several turtles across the projected tornado path, thus increasing the likelihood of a direct measurement (Rasmussen 1995). Successful measurements were made by two turtlelike instruments (also known as "E-turtles," since these also measured electric field) in an F4 tornado on 8 June 1995 near Allison, Texas (Fig. 5.26; Winn et al. 1999): Pressure deficits as high as 55–60 mb were found at a distance of approximately 660 m from the center of the tornado.

Variously configured Doppler radars can remotely sense tornado airflow characteristics, distribution of airborne debris and precipitation scatterers in and around the tornado core (using radar reflectivity factor), and turbulence (with certain assumptions, using spectrum width data; see Istok and Doviak 1986). Consider the recent development of mobile radars. Obviously, unlike their fixed-site counterparts, mobile radars can be brought very close (within a distance of a few kilometers) to the tornado, providing for the high spatial resolution and also for radar scans at very low altitudes above radar level. The mobility, however, restricts the radar dish size, which in turn limits the antenna beamwidth (hence, effective resolution), given a specific wavelength choice. Moreover, the wavelength is inversely related to the signal attenuation, limiting the type of weather conditions (i.e., the storm-relative tornado-viewing position) under which the radar can effectively operate. Such attenuation is comparably more severe with the 3-mm wavelength, pulsed, mobile Doppler radar, designed and built by A. Pazmany and colleagues at the University of Massachusetts, Amherst (see Bluestein et al. 1995). How-

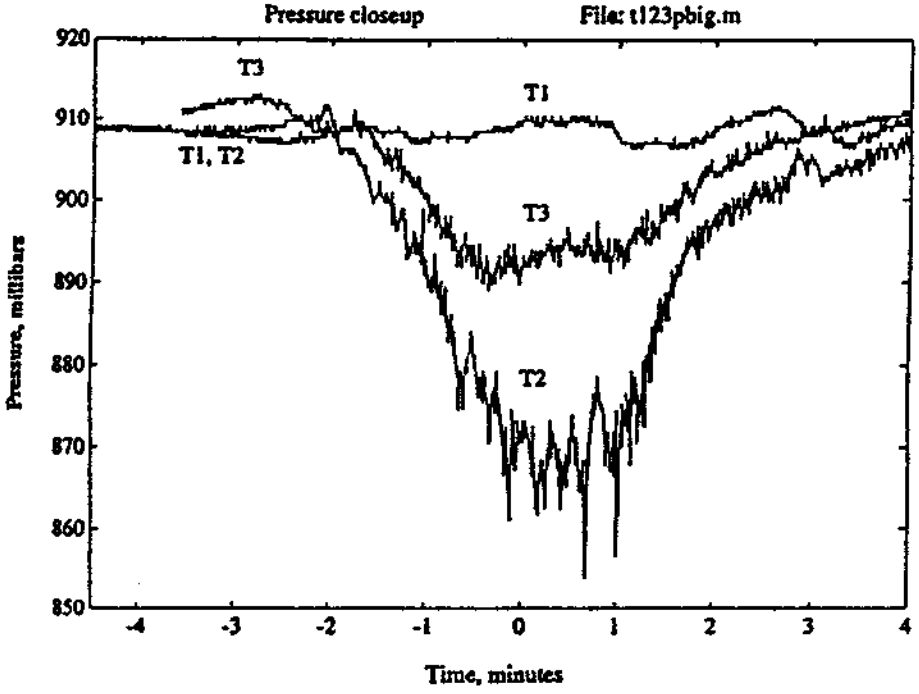

FIG. 5.26. Time series of pressure, measured on the ground by three "E-turtles," in the vicinity of an F-4 tornado near Allison, Texas, on 8 June 1995. Time $t = 0$ is 0100 UTC. From Winn et al. (1999).

FIG. 5.27. Data collected by the Doppler on Wheels radar of an F-4 tornado near Spencer, South Dakota, on 31 May 1998. (a) Radar reflectivity factor and (b) Doppler velocity, at 0136:59 UTC. Courtesy of J. Wurman.

ever, this radar affords very high spatial resolution: The along-beam resolution is 12 m and, owing to the 0.18° antenna beamwidth, the cross-beam resolution (which also depends on the range to the tornado) can be as low as 5–10 m, as was attained in the 3 May 1999 tornado near Oklahoma City, Oklahoma. As a consequence, this radar is capable of resolving radar reflectivity structures, such as within an apparent tornado "eyewall," suggestive of asymmetries in the tornado vortex in the form of waves or multiple vortices (Fig. 5.23; see also Bluestein and Pazmany 2000). In 1995, J. Wurman and colleagues developed a pulsed, 3-cm wavelength, mobile Doppler radar (Wurman et al. 1997), known as the DOW (Doppler on Wheels). The antenna beamwidth is 0.93°; (tens of meters)^3 resolution volumes and 30–60-s volume scans are possible. Structures resolved by the DOW include a weak-echo hole like that documented by Fujita (1981; see Wurman et al. 1996) and also spiral bands, like those observed in hurricanes (Fig. 5.27). DOW data have also proved useful for the evaluation of azimuthal velocity models (such as the Rankine vortex; see Wurman and Gill 2000). We note that a two-DOW deployment has been attempted with some success since 1997. However, these operations have been focused on gathering data on tornadogenesis rather than tornado structure.

d. Tornado flow regions

1) CORE AND OUTER FLOWS

The outer flow (region Ia) extends outward from the core at least 1 km. It consists of air that approaches and rises around the core, while approximately conserving its angular momentum. Consequently the air spins faster as it gets closer to the axis.

The core (region Ib) is the region surrounding the axis and extending outward to roughly the radius of maximum tangential winds. Core radii vary from tens to hundreds of meters. Narrow cores are approximately in solid-body rotation, owing to the importance of turbulent diffusion. In contrast, the angular velocity in wide cores may increase outward from the axis to close to the core wall. The axial flow in the core may be either upward or downward and there may be axial stagnation points aloft separating axial upflow and downflow.

Flows of the type $u = 0$, $v = v(r)$, $w = 0$ are inertially stable (unstable) to axisymmetric radial displacements according to the criterion $\partial M^2/\partial r > 0$ everywhere ($\partial M^2/\partial r < 0$ somewhere), where M is angular momentum (Rayleigh 1916). For small displacements δ a parcel's radial acceleration is governed by

$$\frac{d^2\delta}{dt^2} \approx -\frac{1}{r_0^3}\left.\frac{\partial M^2}{\partial r}\right|_{r_0}\delta. \qquad (5.17)$$

If M^2 decreases with radius, the parcel experiences a force that acts to move it farther away from its original radius r_0 and the flow is unstable. If M^2 increases with radius, the parcel experiences a restoring force and oscillates about its original position with a frequency $[(1/r_0^3)(\partial M^2/\partial r)|_{r_0}]^{1/2}$. These oscillations are called *inertial* or *centrifugal waves.*

Since both narrow and wide cores are inertially stable, perturbations can generate inertial waves that

may propagate vertically along the core and there is virtually no entrainment of air into the core from region Ia. The core must consist of air that has entered the vortex from its lower end through the boundary layer and corner region and/or from its upper end.

More general flows of the type $u = 0$, $v = v(r)$, $w = w(r)$ are stable to axisymmetric disturbances if $[(1/r^3)(\partial M^2/\partial r)]/(\partial w/\partial r)^2 > \frac{1}{4}$ everywhere (Howard and Gupta 1962), a stability criterion analogous to the Richardson number criterion for stability of stratified flows with the local inertial frequency replacing the buoyancy frequency and $\partial w/\partial r$ replacing $\partial u/\partial z$. Thus large radial shears in vertical velocity can overcome the rotational stability of the core flow, perhaps explaining why some cores appear highly turbulent, although breaking waves may be another cause (Rotunno 1979). If the flow is heterogeneous, the stability criterion becomes roughly $(1/r^3)(\partial M^2/\partial r) - (M^2/r^3) \times (1/\theta)(\partial\theta/\partial r) > \frac{1}{4}(\partial w/\partial r)^2$ (Lewellen 1993). Cold air in the core of the vortex ($\partial\theta/\partial r > 0$) is another destabilizing factor because the potentially cool air may be centrifuged outward and replaced by potentially warmer air. Such replacement would also lower the central pressure because warm air is less dense. These considerations set limits on how potentially cold the air in the core can be compared to surrounding air. The reduction of entrainment in strongly rotating flows explains why the introduction of swirl into the inflow intensifies warm-core updrafts and flames in fire whirls. In a subsiding core, air can be potentially very warm if it descends dry adiabatically from a considerable height. The presence of buoyant air in the core again dampens turbulence and lowers the central pressure hydrostatically.

Exact analytical solutions of the governing equations for the core and outer flow in a real fluid are reviewed in Lewellen (1976) and Davies-Jones (1986). These solutions are not totally realistic because they fail to satisfy realistic conditions at the ground and at radial and/or vertical infinity. They are informative, however; for example, they reveal that the radius of the core of steady laminar vortices r_m is determined by the balance between the inward advection and outward diffusion of angular momentum, resulting in core radius varying as $(v/C)^{1/2}$ where C is the applied horizontal convergence (e.g., Burgers 1948; Rott 1958; Sullivan 1959; Kuo 1966, 1967). (In the simulator r_m varies as $[v/M]^{1/2}$ for reasons explained below.)

However, the above balance does not apply to turbulent vortices because Lilly (1969) calculated from photogrammetric data that the turbulent diffusion of angular momentum in a tornado is inward (a negative eddy viscosity phenomenon) and because Davies-Jones (1973) and Baker and Church (1979) found that the core radius of turbulent vortices r_c in the simulator depends primarily on the swirl ratio and increases with it, and for fixed volume flow rate is nearly independent of the depth of the confluent layer zone feeding the updraft. Baker and Church refined Ward's core radii measurements and extended them to large S, where multiple vortices develop in the simulator (see below). In the multivortex regime, the core radius pertains to the azimuthally averaged flow. Originally it had been thought that the core radius was a function of the tangent of the inflow angle M/Qh in the confluent zone (Ward 1972). In the limit of inviscid flow ($v \to 0$), angular momentum M is conserved and the outer flow cannot penetrate to the axis because this would require infinite inward pressure-gradient force to counteract the infinite centrifugal force M^2/r^3 at $r = 0$. There has to be a nonrotating core composed either of air that was already present prior to the onset of rotation or of nonrotating air that has descended through the top boundary of the simulator. The simplest inviscid axisymmetric model of this flow consists of a stagnant core separated from irrotational outer flow by a vortex sheet. Because the core is stagnant, the core pressure p_c is constant. The radius of the core varies from r_1 at the ground to r_2 at the top of the apparatus. The updraft above the inflow is assumed to be cylindrical with the meridional flow becoming increasingly vertical with height (i.e., $u \to 0$). Since the outer flow is irrotational, $\partial w/\partial r \to 0$ and $w \to 2Q/(r_0^2 - r_2^2)$ with height in the outer flow. Just outside the intersection of the core wall with the ground, $u = w = 0$ and $v = M/r_1$. Since pressure is continuous across the core wall, Bernoulli's equation applied to the streamline just outside the core yields the relationships

$$p_\infty = p_c + \frac{\rho}{2}\left[\frac{M^2}{r_2^2} + \frac{4Q^2}{(r_0^2 - r_2^2)^2}\right]$$

$$= p_c + \frac{\rho}{2}\left[\frac{M^2}{r_1^2}\right], \tag{5.18}$$

where p_∞ is the pressure at infinity and the stagnation pressure of the outer flow. In terms of the pressure drop driving the vortex $\Delta p \equiv p_\infty - p_c$, the core radius at the ground is given by

$$r_1 = (2\Delta p/\rho)^{-1/2} M. \tag{5.19}$$

Also from (5.18), the core radii at the ground and near the top are related by

$$\frac{1}{x_1} = \frac{1}{x_2} + \frac{1}{S^2}\frac{1}{(1 - x_2)^2}, \tag{5.20}$$

where $x_1 \equiv (r_1/r_0)^2$ and $x_2 \equiv (r_2/r_0)^2$. In the simulator, the core is composed of initially nonrotating air that descends through the honeycomb baffle at the top of the updraft. The stagnation pressure of this air is lower than that of the inflow air by an unknown amount so that the core radius cannot be obtained directly from

(5.19). Davies-Jones (1973) postulated that the core radius can be determined by minimizing Δp for given Q, M, and r_0. This is equivalent to minimizing the maximum wind speed in the flow, which occurs at the core wall, or minimizing $1/x_1$ in (5.20). According to Binnie and Hookings (1948), the resulting flow is critical in the sense that the exit vertical velocity is equal to the phase speed of a long small-amplitude inertial wave. The minimum strength vortex occurs when

$$S^2(1 - x_2)^3 = 2x_2^2. \tag{5.21}$$

An optimum core radius for minimizing extreme wind speed exists for fixed Q, M, and r_0 because tangential velocity becomes large as $x_2 \to 0$ and vertical velocity becomes large as $x_2 \to 1$ owing to the cross-sectional area of the updraft $\pi r_0^2(1 - x_2) \to 0$. The theory can account for the core radius increasing from 0 at $S = 0$ to r_0 as $S \to \infty$. The method predicts the core radius fairly well at large S, but is too large at small S, probably owing to the neglect of turbulent stresses along the core wall, the effects of which should increase with the length of the vortex (Baker and Church 1979). Wilkins and Diamond (1987) demonstrated that for fixed updraft radius the core radius decreases as the height of the baffle is increased. Other theories may yield better fits, but they have at least one tuning parameter and some assume a radius that does not vary with height. Note that although the radius of a rotating thunderstorm updraft is probably an optimum value according to some variational principle, it is not obvious that this value has to be independent of swirl ratio. This casts doubt on the straightforward applicability of the laboratory core radius results to tornadoes.

Unlike the simple inviscid solution, the similarity solutions of the full equations presented by Burgers (1948), Rott (1958), Sullivan (1959), and Kuo (1966) all suffer from decoupling of the swirling and meridional flows because the radial pressure gradient is independent of height. This condition cannot be satisfied in atmospheric vortices because they are not infinitely tall. Long's (1958) similarity solution and Morton's (1966) scale analysis for a tall thin axisymmetric vortex that spreads slowly with height showed that 1) the core is in cyclostrophic balance, 2) vertical and tangential velocities in the core are of the same order of magnitude, while radial velocities are much smaller, and 3) swirling and updraft flows interact strongly. Of the above solutions, Kuo's are the only

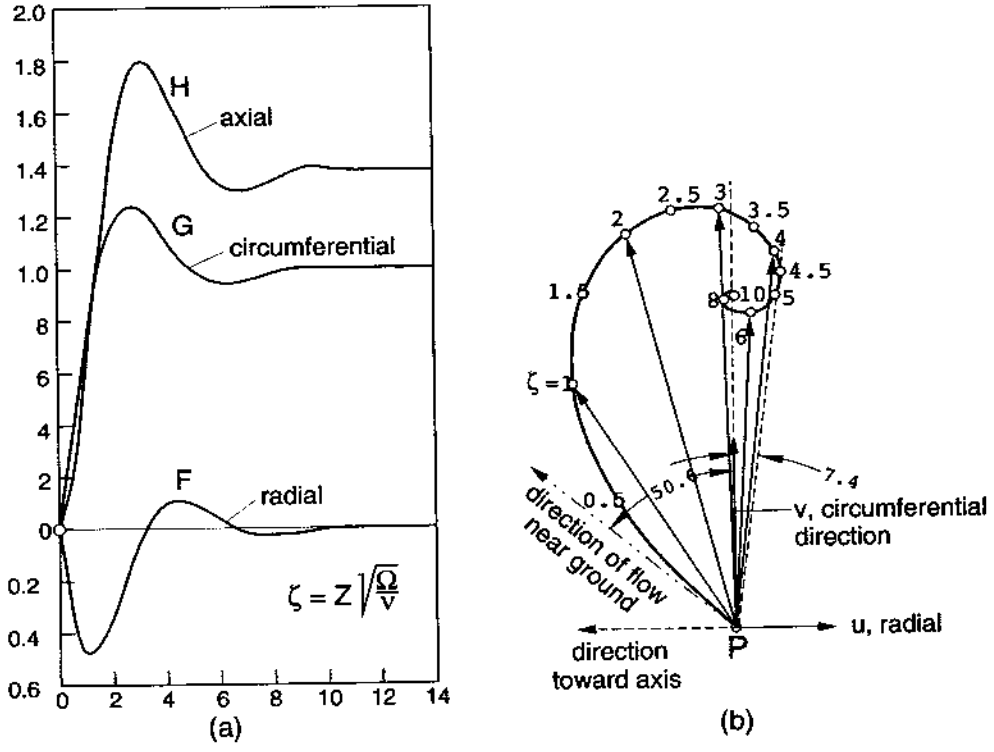

FIG. 5.28. The boundary layer beneath a fluid in solid-body rotation. (a) The functions $F(\zeta)$, $G(\zeta)$ $H(\zeta)$ where $\zeta \equiv z(\Omega/\nu)^{1/2}$ is the nondimensional height. The radial, tangential and vertical velocities are given by $u = r\Omega F(\zeta)$, $v = r\Omega G(\zeta)$ and $w = (\nu\Omega)^{1/2}H(\zeta)$. (b) Hodograph of horizontal wind. From Schlichting (1960; reprinted with permission).

ones for convective vortices in a (conditionally) unstable atmosphere, albeit a saturated one. Both the one- and two-cell solutions have cold cores as a result of assuming that saturation is maintained everywhere, an unlikely circumstance in the core of a two-cell vortex. Lewellen (1993) concludes that buoyancy forces are unimportant in the corner region except for their role in stabilizing the flow, but become quite important in the core at higher levels.

2) THE BOUNDARY LAYER

Frictional interaction of a "primary" rotating flow with the ground reduces tangential velocities near the surface. Pressure does not vary much across the boundary layer and therefore the imbalance between the radial pressure-gradient force and the reduced centrifugal force drives a strong radial inflow within the lower part of the boundary layer; the boundary layer of a tornado is roughly 100 m deep. Bödewadt (1940) found an exact similarity solution describing the laminar interaction of a flow rotating as a solid body at the rate Ω with a stationary solid rigid surface (Fig. 5.28). The boundary layer thickness $\delta \approx 8(\nu/\Omega)^{1/2}$, where ν is the kinematic viscosity. The maximum radial inflow velocity of $0.5\Omega r$ occurs at a height of around $\delta/8$. The vertical velocity, equaling $1.4(\nu/\Omega)^{1/2}$ far from the ground, is independent of radius and is upward at all heights. All three velocity components overshoot as they tend to their values at great height. The radial inflow forces the overshoot in tangential velocity, resulting in rotation in the midboundary layer that exceeds the rotation aloft by 25%. Paradoxically, friction can increase extreme wind speeds!

Of more relevance to tornadoes and hence to region II is the case in which the primary swirling flow is a potential vortex, wherein $v \propto 1/r$ (rather than a solid-body rotation, wherein $v \propto r$). Burggraf et al. (1971) matched a laminar boundary layer on a surface of radius r_s to a potential vortex. They found that the boundary layer has a double structure with an inner viscous layer next to the surface with variable thickness of order $(\nu/M)^{1/2}r$, in which the flow is primarily radial, and an outer inertial layer of order $(\nu/M)^{1/2}r_s$ thick, in which the flow recovers to the external potential flow; the head $B \equiv (p/\rho) + \frac{1}{2}\mathbf{v}\cdot\mathbf{v} + gz$ is nearly conserved in the outer layer. In contrast to the Bödewadt solution, the vertical velocity is negative and thus the inward mass flux in the boundary layer cannot be compensated for by flux out of the top of the boundary layer: The fluid has no escape until it reaches the core radius where M is no longer constant; then it turns violently upward inside a narrow core. The laminar boundary layer in the simulator has a similar double-layer structure; the radius r_s at which the swirling boundary layer effectively begins is said to correspond to the radius of the rotating screen or the vanes (Fiedler and Rotunno 1986). Note, however, that the flow above the boundary layer in the confluent zone and in the outer part of the convergence zone has a strong radial component. Hence, the effective beginning radius of the potential vortex boundary layer thickness may only be $0.6r_0$ (Wilson and Rotunno 1986).

The nature of the flow in the boundary layer is Reynolds number dependent. The boundary layer of flow past a flat plate (for which the pressure gradient is neutral) becomes turbulent at a Reynolds number of around 3×10^5 for a smooth surface and at lower values for rough surfaces. The radial Reynolds number $\mathrm{Re}_r \equiv Q/\nu h$ in the simulator is typically close to this critical value. Given that the radial pressure-gradient force is inward and hence favorable for the damping of perturbations in the inflow, we conclude that the flow in the boundary layer may be either laminar or turbulent, depending on the settings of the external parameters. In the atmosphere, Re_r is much higher, $\mathcal{O}(10^9)$, and the ground is rough, so it is generally accepted that the ~100-m boundary layer of a tornado is turbulent rather than laminar, although the flow may be relatively smooth because of the favorable pressure gradient. For reviews of turbulent boundary layers pertinent to tornadoes, we defer to Lewellen's (1976, 1993) articles. Since the boundary layer is rotating, it is susceptible to Ekman instability and consequent formation of horizontal roll vortices resembling the spiral bands in hurricanes (Faller 1963). The boundary layer rolls are oriented about 15° to the left of the flow above the boundary layer.

3) THE CORNER REGION

The boundary layer erupts upward in region III, the corner region. It is here that missiles are generated and debris is lofted into the air. Light debris such as bank checks drawn up into the storm through this region may be transported hundreds of kilometers downstream (Snow et al. 1995; Magsig and Snow 1998). The vertical pressure gradient, which is small in boundary layers, is large here. The mass flux of virtually nonrotating air that flows into the vortex through the lower part of the boundary layer and the corner region is insufficient to "fill" or eliminate the vortex from below. Lewellen (1976) suggested that the maximum tangential velocity in the tornado occurs in the upper half of the corner region: Parcels flowing into region III from the upper part of region II penetrate closer to the axis than parcels in region Ia and consequently gain more tangential velocity (the loss of angular momentum is not large enough to annul this gain).

Vortex breakdown is most important to high tornadic wind speeds when it occurs in the corner region, and therefore this phenomenon is introduced here. Note that the following discussion is relevant to the tornado but not to its mesocyclonic parent circulation, despite some recent observations that have been interpreted otherwise (Trapp 2000). The vortex breakdown

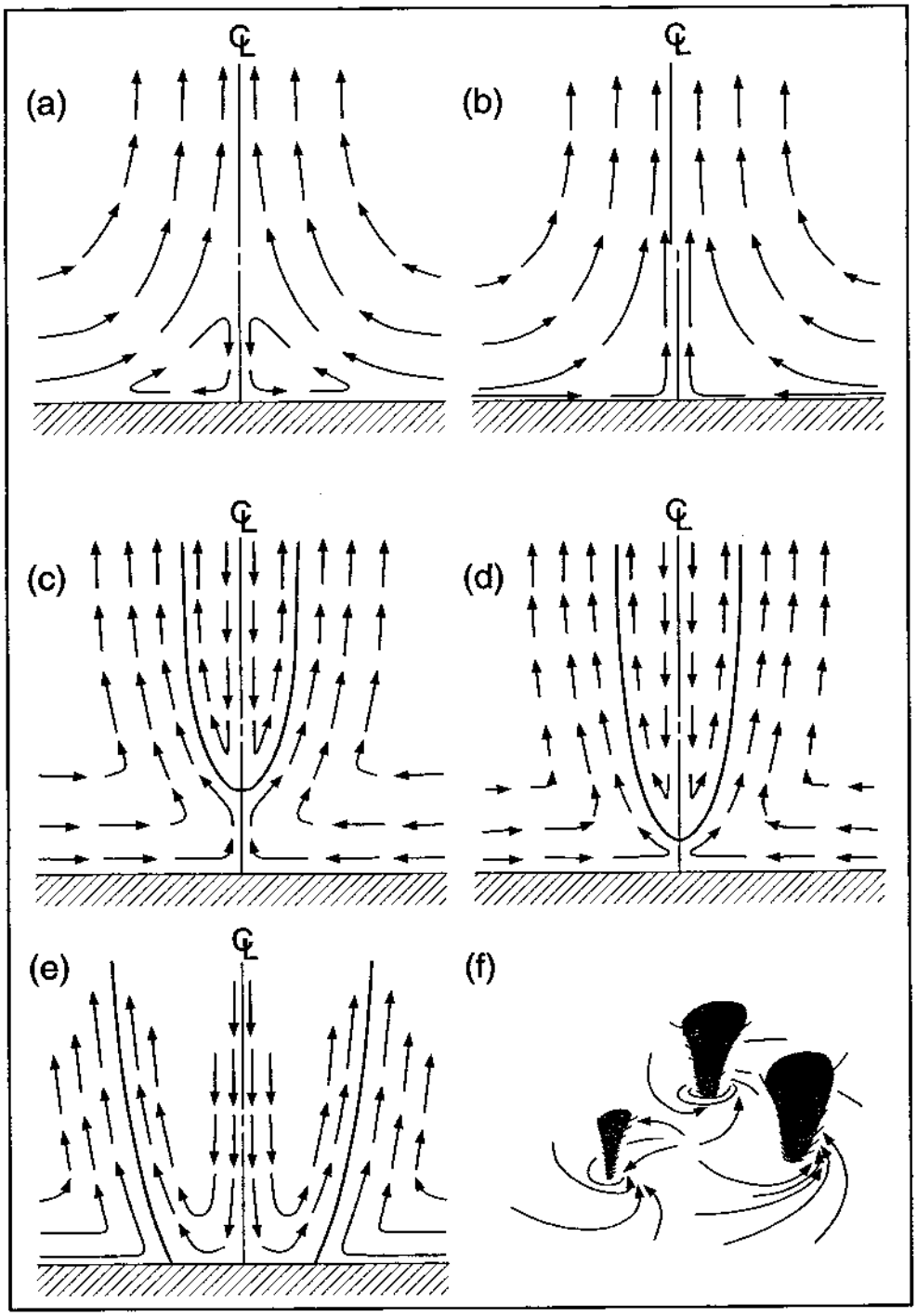

FIG. 5.29. Effect of increasing swirl ratio, S, on tornadic vortex flows. (a) Very weak swirl—flow in boundary layer separates and passes around corner region and there is no tornado; (b) Low S—smooth-flowing one-cell weak tornado; (c) Moderate S—end-wall boundary layer erupting upward into strong smooth-flowing end-wall vortex that breaks down near the top of the boundary layer into a turbulent two-cell vortex aloft: (d) Slightly higher S—drowned vortex jump (DVJ) with the defining characteristic of the vortex-breakdown stagnation point very close to the ground; (e) Turbulent two-cell tornado at higher S—the central downdraft now impinges on the ground, eliminating the stagnation point aloft, inflow in the boundary layer erupts upward in a now-annular corner region, and the core radius increases rapidly with S; (f) Large S—tornado "splits" into multiple vortices (2, 3, . . . , 6 as S increases). (Modified from Davies-Jones 1986.)

is the rotating-flow counterpart of the hydraulic jump in stratified flows. It is a transition between two conjugate vortex states (Fig. 5.29c) that occurs when the swirl ratio increases beyond a critical value of order one. For tornado-like vortices, the upstream state (below the breakdown level) is a smooth, high-speed swirling jet that arises from the eruption of the boundary layer near the axis. It is also referred to as an end-wall vortex. In the downstream state above the breakdown, the vortex "bursts" into a much wider two-celled structure with highly reduced axial flow (often downdraft) surrounded by updraft, much higher levels of turbulence, lower vertical and tangential velocities, and reduced pressure deficit. In some cases the upper flow is asymmetric and assumes the form of a precessing single or double helix. With vortex breakdown, it is possible to have a tornado that appears as a condensation funnel below a bowl-shaped lowering of cloud base with a cloud-free gap in between (see Pauley and Snow 1988).

The upstream state is supercritical, meaning that the upward flow is faster than the speed of the fastest inertial waves and information of the downstream conditions cannot be carried upstream (i.e., downward) by the waves. The flow above the breakdown is subcritical so that waves are able to progress upstream as far as the breakdown and "impart knowledge" of the downstream conditions or the top boundary condition throughout the subcritical vortex. The conjugate states arise because the inviscid swirl equation (Wilson and Rotunno 1986) has both a supercritical and a subcritical solution for the same distribution of angular momentum across streamlines $M(\psi)$. Like the hydraulic jump, the vortex breakdown is a transition between conjugate states. Maxworthy (1972) views vortex breakdown as a "buffer zone" through which incompatible upstream and downstream boundary conditions can be matched. The downstream flow can become supercritical again with the subcritical flow confined to a bubble-shaped enlargement of the core. In these cases a second breakdown can occur farther downstream.

Fiedler (1989) has argued that the flow in supercritical end-wall vortices might be laminar if the boundary layer is turbulent. This would account for the smooth appearance of some slender condensation funnels. Lewellen (1993) disagrees since the advective timescale in region III is too small for the total elimination of turbulent eddies. Condensation funnels may appear laminar simply as a result of rotational damping of turbulent eddies. Furthermore, the balance between inward advection and outward viscous diffusion of angular momentum yields an unrealistically small core radius of less than 1 m in Kuo's (1966) vortex solution.

4) THE UPPER FLOW

The upper-flow region of the tornado is uncertain because it is embedded in the parent storm and has yet to be observed in detail with present instruments (Lewellen 1993). The core of a moderate tornado that has a TVS only to midaltitudes (perhaps only up to 3 km; Brandes 1981) may become unstable at some height and change into a turbulent buoyant nonrotating plume with the angular momentum at this level transported outward by turbulent eddies (Lewellen 1993), as apparently occurs in the experiment of Mullen and Maxworthy (1977). The strong buoyancy of the air above the vortex acts like a "buoyant cork" (Fiedler 1995) by preventing the core low pressure from being filled from above.

A large tornado that reaches to near the tropopause (Brown et al. 1978; Johnson and Ziegler 1984) probably terminates in surrounding upflow that is strongly divergent. As pointed out by Lilly (1969), the dynamics of rotating and nonrotating updrafts differ near the tropopause. The anvil outflow from a nonrotating updraft is driven by an outward pressure-gradient force that arises as follows. The updraft penetrates above the equilibrium level (EL) into the stratosphere creating an overshooting storm top and, relative to the environment, a cold dome of air that gives rise hydrostatically to high pressure beneath it. The cold dome cancels the effect on the surface pressure of the warmth of the updraft column below the EL, so there is little hydrostatic pressure deficit at the ground. Using the inviscid swirl equation, Lilly showed that a rotating updraft can terminate without overshooting the EL. In this case the radial pressure gradient goes to zero and unbalanced centrifugal forces can drive the outflow. Without a cold dome, there is low hydrostatic pressure at the surface, which can be maintained in a vortex because it has "dynamic walls" owing to its cyclostrophically balanced state. Even though the vortex is tilted so that its top does not overlie its base, its nonporous core acts like the glass walls of a tilted mercury barometer in transmitting the hydrostatic pressure deficit down the axis. Some of the environmental potential energy can now be realized in the form of violent surface winds (see section 5.5).

e. Different flow regimes

As the swirl ratio in the simulator is increased, vortex structure changes as shown in Fig. 5.29. The critical swirl ratio values given below are approximate because they depend slightly on Reynolds number and they are machine dependent because of differences in the height of the baffle H compared to r_0 (Wilkins and Diamond 1987). At $S = 0$ high pressure at the stagnation point at the foot of the axis causes the boundary layer to separate in the region of adverse pressure gradient, and the outer flow circumvents the corner region that consists of a recirculating eddy. A very small amount of swirl does not change this pattern of meridional circulation so that even if a weak vortex forms it will not be in contact with the ground. Low

swirl is sufficient to cause the boundary layer to reattach itself, resulting in a one-cell vortex, which by definition has a central updraft (except near the top baffle where the vortex breaks down). In the one-cell vortex, the central pressure deficit at the surface is surrounded by a ring of high pressure. This occurs at a radius where the wind speed just above the boundary layer is a minimum, owing to a rapid decrease of tangential velocity with respect to radius outside the core, and an increase in radial inflow with respect to radius from the axis to $r = r_0$ (Ward 1972). Addition of more swirl keeps the boundary layer attached to the ground, eliminates the adverse pressure gradient and high pressure ring, and lowers the vortex breakdown. The subcritical flow consists of a bubble or eddy of recirculating air at the base of an enlarged turbulent wakelike vortex core, which is capped at a downstream axial stagnation point by either stagnant flow or downflow near the axis. With increasing swirl, the flow between the two stagnation points evolves into first a single helix and then a double helix (Church and Snow 1979).

At moderate swirl ratio, the boundary layer erupts into a smooth, high-speed vortex jet that ends at a low-level vortex breakdown, above which exists a much larger turbulent two-celled vortex. At a critical swirl ratio $S^* \approx 0.45$, the breakdown point descends into the surface boundary layer. This case is called a *drowned vortex jump* (DVJ; Maxworthy 1973; Snow 1982). Note that the critical swirl ratio for this and other transitions decreases to an asymptotic value as the radial Reynolds number (Re_r) is increased (Church et al. 1979). As S increases beyond S^*, the breakdown point is eliminated altogether as the central downdraft impinges on the ground and the boundary layer erupts in a now annular corner region surrounding the inner cell of the vortex. With increasing S, the core radius increases and the vortex resembles a wide single-vortex tornado.

At large swirl ratio, $S \approx 0.8$, the single vortex becomes unstable and "splits" instantaneously into two secondary vortices that form near the radius of maximum tangential wind of the primary vortex. These vortices revolve around the axis under the influence of each other and their parent circulation at the rate of about half the maximum tangential wind speed of the primary vortex. As S is increased to 3 or beyond (depending on Re_r and the version of the simulator), further transitions to three, four, five, and six vortices occur. A system of seven vortices has not been observed, perhaps because seven equal-strength line vortices spaced regularly around a circle is an unstable configuration (Saffman 1992, p. 119).

Increasing the swirl ratio with a vortex pair initially present sends the flow into a disordered state before the swirl ratio becomes large enough for a triad of vortices. The higher transitions also occur following episodes of chaotic flow. This behavior is typical of nonlinear dynamical systems and flows in transition to turbulence (Sreenivasan 1985). As S is decreased, the reverse transition—from two vortices to one vortex—occurs at a higher critical swirl ratio. This hysteresis effect is characteristic of a subcritical bifurcation in the theory of dynamical systems (Bergé et al. 1984, pp. 40–42).

We note here that it is possible to define a local corner flow swirl ratio, $S_c \equiv r_c M_\infty^2 / \Upsilon$, where r_c is the radius of maximum swirl velocity in the upper-core region, M_∞ is angular momentum outside the core and boundary layer, and Υ is the total depleted M flux flowing through the corner flow region (Lewellen et al. 2000). Whereas S characterizes the swirling, converging flow within which the tornado vortex forms, S_c characterizes the surface-layer core flow embedded within this larger-scale swirling converging flow; both affect tornado structure. Hence, as Lewellen et al. state, S_c does not replace or redefine S, yet S_c can more completely determine the corner-flow structure. Indeed, since only S_c can compensate for the existence of/variations in surface-layer inflow of low angular momentum fluid, flows with the same S can exhibit very different vortex structure in the corner flow region.

Ward (1972), Davies-Jones and Kessler (1974), and Davies-Jones (1976) idealized the two-cell vortex as a cylindrical vortex sheet in an otherwise irrotational flow and suggested, without proof, that the multiple vortices formed as a result of this vortex sheet becoming barotropically unstable and rolling up into individual vortices. Rotunno (1978) proved this conjecture by demonstrating that a cylindrical vortex sheet with an inner uniform downdraft and outer uniform updraft is unstable to three-dimensional perturbations. The most unstable perturbation is a helical one with negative pitch (i.e., turns anticyclonically with height in a cyclonic vortex), in agreement with the observed negative pitch of secondary vortices in tornadoes and in laboratory and numerically simulated vortices. The perturbations also transported angular momentum radially inward, consistent with Lilly's (1969) analysis of Hoecker's (1960) photogrammetric wind measurements in the 1957 Dallas tornado and with the pressure profile observed by Winn et al. (1999). Extreme winds are located in the secondary vortices. In the simulator the instantaneous winds in a secondary vortex may be almost double the maximum winds in the azimuthally averaged flow (Leslie 1977).

Increasing the surface roughness generally increases the core radius, radial and vertical velocities, turbulence levels, and the critical swirl ratios for transitions to higher numbers of vortices, while decreasing tangential velocities. Effects of surface roughness on tornadoes and laboratory vortices are discussed further in Davies-Jones (1986) and Church and Snow (1993).

f. Measurements in the simulator

Extensive pressure measurements, both at the surface (Snow et al. 1980; Pauley et al. 1982) and aloft (Church and Snow 1985; Pauley 1989) have been made in the Purdue University version (TVC I) of the Ward-type simulator. Church and Snow (1985) found that the nondimensional axial pressure deficit $\Delta p^* \equiv \Delta p/\rho\bar{w}^2$ is a function of S and has a maximum value of 60 at S just less than $S^* \equiv 0.45$. The minimum occurred in the laminar supercritical vortex at a height of several core radii above the surface. The elevated pressure minimum is a common feature of the laminar vortices. To avoid confusion we denote the core radius and maximum velocities in laminar supercritical and turbulent subcritical vortices by subscripts m and c, respectively. Church and Snow also found that the core radius of the supercritical vortex $r_m \approx \delta \equiv r_s(\nu/M)^{1/2}$ where δ is the depth of the laminar boundary layer. This indicates that the end-wall vortex is simply a continuation of the boundary layer. In terms of $\beta_1 \equiv \Delta p/\rho v_m^2$, where $v_m \approx M/2\delta$ is the maximum tangential wind speed (allowing for loss of angular momentum), $\Delta p^* \sim \beta_1 (r_0^2/r_s^2)(M/\nu)S^2$, so the nondimensional pressure deficit increases rapidly with S until S^* is reached. Since head is nearly conserved from the rotating screen to the axis in the upper boundary layer, the maximum vertical velocity w_m in the end-wall vortex at $S \approx S^*$ is given by $w_m^2/2 \approx \Delta p/\rho = 60\bar{w}^2$ or $w_m \approx 11\bar{w}$ (Fig. 5.30). According to velocity measurements in laminar vortices $v_m \approx 0.54w_m$, so $v_m \approx 6\bar{w}$ and $\beta_1 \approx 1.7$. Baker and Church (1979) showed that the maximum tangential velocity in turbulent cores v_c was given by $v_c \approx 2.6\bar{w}$ over a wide range of S. Assuming that $r_c \approx M/2v_c$, this is consistent with $r_c/r_0 \propto S$. For these vortices the nondimensional pressure deficit is much smaller, $\Delta p^* \approx 6.8\beta_2$, where $\beta_2 \equiv \Delta p/\rho v_c^2$ is probably around 1 based on Kuo's two-cell vortex. The maximum tangential velocity is 2.3 times larger below the breakdown than above it. Fiedler and Rotunno (1986) have shown from a solution of the inviscid swirl equation that this is roughly commensurate with conjugate states with flow force (Morton 1966, 1969) invariant across the breakdown, but with a loss of head owing to turbulence at the top of the jet. Their solution also predicted the value of S^*.

According to the Purdue measurements, the azimuthally averaged surface pressure field has the following characteristics. The lowest pressure is at the center for one-celled vortices, and maximizes at $S \approx S^*$. For $S > S^*$ the vortices become two-celled at the surface, the lowest surface pressure becomes located in a ring off center with a slight pressure maximum on the axis, and Δp^* is much less than in the end-wall vortex because the tangential velocity is much reduced. Although Δp^* increases once more at swirls beyond the transition to multiple vortices, it never reaches the maximum value attained at $S \approx S^*$. The pressure deficits in individual secondary vortices were also measured; these were 2–3 times greater than the Δp^* in the azimuthally averaged flow, but were still less than Δp^* at S^*.

The variation of central pressure with height was also measured. For the laminar vortices, core pressure

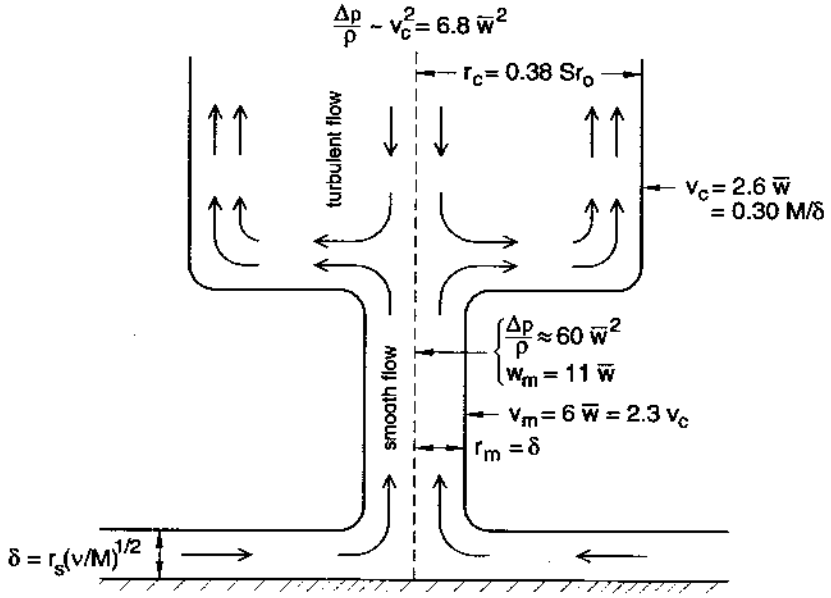

FIG. 5.30. The geometry of and the velocities in the supercritical end-wall vortex and the subcritical turbulent vortex aloft at S slightly less than $S^* = 8.7\delta/r_0$.

decreases rapidly with height, then becomes constant. As shown above, Δp^* aloft in laminar vortices increases as the cube of the circulation so that the largest pressure deficit occurs at $S \approx S^*$. The strong upward pressure-gradient force near the surface provides the upward acceleration for air in the corner region. The pressure deficit at the surface is less than the maximum deficit aloft by a factor that ranges up to 7. The pressure deficit declines abruptly with height across the vortex breakdown. The largest surface pressure deficit is associated with the DVJ. In this case the pressure deficit declines rapidly with height. In the turbulent two-celled vortices that occur at $S > S^*$, the axial pressure deficit is much less than in the DVJ, but declines little with height. Over the region of parameter space that has been investigated, 60 appears to be an upper limit for the maximum nondimensional pressure deficit that can occur in the simulator.

5.5. Tornado intensity

The issue of tornado intensity can be addressed using measurements of maximum tornado wind speed, through theoretical considerations of the kinetic energy of the tornado, and/or by atmospheric scaling of atmosphere laboratory or numerical model results, the caveats of which are discussed in section 5.4. In the spirit of the preceding sections, we begin with a discussion of relevant tornado observations, which, as mentioned above, indicate wind speeds as high as 125 m s^{-1} to perhaps 140 m s^{-1}.

a. Measurements of maximum tornado wind speeds

Photogrammetric analyses of tornado-debris movies (e.g., Hoecker 1960; Golden 1976; Golden and Purcell 1978a; and many others) have yielded maximum wind speed estimates ranging from 56 to 95 m s^{-1}, at 15–200 m above the ground; aloft, in a suction vortex, Forbes (1978) estimated wind speeds as high as 125 m s^{-1}. Analyses additionally suggest upward vertical velocities in tornadoes as high as 25–60 m s^{-1} between 25 and 60 m AGL. The photogrammetric techniques require accurate knowledge of the distance of visible landmarks (in the film) and of the tornado to the camera site. Air tracers (tornado debris, cloud tags) can then be scaled on each movie loop and subsequently tracked on a grid (Golden and Purcell 1978a). The techniques may underestimate maximum wind speed owing to the following reasons: (i) the tracer motion may be less than the actual wind speed, (ii) the location of the maximum wind speeds may be hidden by an opaque dust column or condensation funnel, and (iii) the line-of-sight motions cannot be determined. In addition, debris tracers may be absent in some parts of the vortex.

With Doppler radar, the maximum wind speed estimation proceeds as follows. Facilitated by the use of a relatively high pulse repetition frequency, unfolded Doppler spectra can be computed; maximum wind speeds in the radar volume are then determined by locating the highest frequency in the spectrum above the noise floor (see also Doviak and Zrnic 1993, pp. 344–350). Such a Doppler spectrum of a tornado was first reported by Smith and Holmes (1961): Using a fixed-site CW (continuous wave) Doppler radar in Kansas in 1958, they found maximum wind speeds in a tornado of 92 m s^{-1}. Comparable estimates (65–92 m s^{-1}) from a number of tornadoes that passed within a 100-km range of NSSL's 10-cm wavelength, fixed-site, pulsed Doppler radar have been reported by Zrnic and Doviak (1975), Zrnic et al. (1977), Zrnic and Istok (1980), and Zrnic et al. (1985).

A portable, 3-cm wavelength, CW Doppler radar, designed and built at the Los Alamos National Laboratory (LANL) (and later modified to have the capability to collect Doppler spectra in range bins of 78-m spacing, using FM-CW signal processing), has been utilized to increase the probability of determining the Doppler velocity spectrum at and below cloud base in tornadoes (Bluestein and Unruh 1989; Bluestein and Unruh 1993; Bluestein et al. 1993, 1997). At close range (i.e., within sight, or less than 5–10 km in range), visual documentation by a boresighted video camera mounted on the radar antenna was used to determine the location of the maximum wind speeds relative to the condensation funnel, if present. Most of the portable radar–based estimates (collected during 1987, 1990, 1991, and 1994) of maximum tornadic wind speed were between 50 and 100 m s^{-1}, at some distance (as much as 100 m) above the ground (mea-

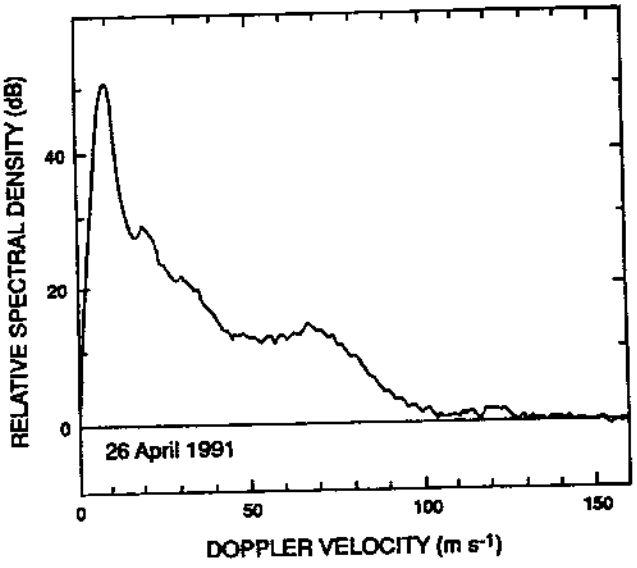

FIG. 5.31. Receding portion of the Doppler velocity spectrum of an F-5 tornado, as measured by a portable, 3-cm wavelength CW Doppler radar near Ceres and Red Rock, Oklahoma, on 26 April 1991. From Bluestein et al. (1993).

surements confined to volumes near the ground were not possible owing to the 5° beamwidth of the antennas). For example, maximum wind speeds in the tornado near Northfield, Texas, on 25 May 1994 reached 65 m s^{-1} and possibly 75 m s^{-1}; the 2-km diameter parent mesocyclone had wind speeds of 45–50 m s^{-1} (Bluestein et al. 1997). Higher wind speeds—up to 120–125 m s^{-1}—were estimated in a tornado on 26 April 1991 near Ceres and Red Rock, Oklahoma (Fig. 5.31; see Bluestein et al. 1993). These measurements were the first confirmation of F5 wind speeds in a tornado based on Doppler radar measurements. [On 3 May 1999, DOW data were collected on a tornado that was associated with F5 damage near Oklahoma City, Oklahoma. Wind speeds possibly as high as 140 m s^{-1}—the upper end of the F5 scale—were measured over a very short duration (~50 ms) at about 50 m AGL; J. Wurman 1999, personal communication.] Not surprisingly, however, wind speeds corresponding to the F-scale ratings for other tornadoes were less than those indicated by the Doppler spectra. Hence, as alluded to in section 5.1, estimates of tornado intensity based on damage surveys alone must be viewed with caution (see also Doswell and Burgess 1988).

A comparison by Bluestein et al. (1993) of simulated wind spectra with actual spectra suggests that the highest radar reflectivities are located well outside the core of the tornadoes, presumably in the debris cloud. This inference is consistent with other radar observations of weak-echo holes. It is therefore possible that there are even higher wind speeds closer to the center of the tornado where radar reflectivities may be too weak to detect a signal and near the ground where wind speeds could not be measured owing to the 5° beam width of the antennas.

b. Theoretical limits

The parent thunderstorm contains far more energy than does the tornado simply because of the thunderstorm's far greater volume. The kinetic energy of the thunderstorm circulation is derived largely from the latent heat released in the updraft and evaporative cooling in the downdraft, and possibly from some conversion from environmental kinetic energy. The high density of kinetic energy in the tornado is associated with a large local drop in pressure, which occurs by mechanisms described below. Investigators have attacked the question of the maximum wind speed that can occur in a tornado by addressing the equivalent question of how large a pressure deficit can be supported in the atmosphere. Since nature abhors even a partial vacuum, a mechanism is needed that prevents fluid from rushing in to fill the void.

Various attempts have been made to place upper bounds on tornado wind speeds by calculating a maximum hydrostatic pressure drop (e.g., Lilly 1969, 1976). The conceptual model assumes a warm axisymmetric updraft column at $r = 0$ in an environment that is in hydrostatic equilibrium at $r = \infty$. The vertical momentum equation

$$\frac{\partial w}{\partial t} + \frac{1}{r}\frac{\partial}{\partial r}(ruw) + \frac{\partial}{\partial z}(w^2) = -c_p\theta(z)\frac{\partial \pi}{\partial z} - g + v\left[\frac{1}{r}\frac{\partial}{\partial r}\left(r\frac{\partial w}{\partial r}\right) + \frac{\partial^2 w}{\partial z^2}\right]$$

reduces at radial infinity to the hydrostatic equation, which can be written as

$$0 = -c_p\theta_\infty(z)\partial\pi_\infty/\partial z - g, \tag{5.22}$$

where the subscript ∞ denotes $r = \infty$. On the axis, denoted by subscript 0, the steady-state vertical momentum equation can be approximated by

$$\frac{1}{2}\frac{\partial w_0^2}{\partial z} = -c_p\theta_0(z)\frac{\partial \pi_0}{\partial z} - g + 2v\left.\frac{\partial^2 w}{\partial r^2}\right|_{r=0} - \left.\frac{1}{r}\frac{\partial}{\partial r}(\overline{ru'w'})\right|_{r=0}, \tag{5.23}$$

where l'Hôpital's rule has been used, and the last term is a turbulent stress term for quasi-cylindrical flow (Pauley 1989). Using (5.22), (5.23) may be written

$$\frac{1}{2}\frac{\partial w_0^2}{\partial z} = c_p\theta_0\frac{\partial(\pi_\infty - \pi_0)}{\partial z} + g\frac{\theta_0 - \theta_\infty}{\theta_\infty} + 2v\left.\frac{\partial^2 w}{\partial r^2}\right|_{r=0} - \left.\frac{1}{r}\frac{\partial}{\partial r}(\overline{ru'w'})\right|_{r=0}. \tag{5.24}$$

Let the updraft terminate at the equilibrium level $z = H$ without overshooting so that $\pi_0(H) = \pi_\infty(H)$ and $w_0(H) = 0$. Then integrating (24) from the top of the corner region $z = \delta$ to $z = H$ yields a formula for the pressure drop near the surface,

$$c_p\tilde{\theta}_S[\pi_\infty(\delta) - \pi_0(\delta)] \approx \text{CAPE} + \frac{1}{2}w_0^2(\delta) + 2\int_\delta^H \left.v\frac{\partial^2 w}{\partial r^2}\right|_0 dz - \int_\delta^H \left.\frac{1}{r}\frac{\partial}{\partial r}(\overline{ru'w'})\right|_{r=0} dz, \tag{5.25}$$

where $\tilde{\theta}_S$ is an intermediate value of $\theta|_{z=0}$ and $\text{CAPE} \equiv g\int_\delta^H [\theta_0(z) - \theta_\infty(z)]/[\theta_\infty(z)]dz$. The pressure drop is related to a maximum tangential wind speed v_M by assuming cyclostrophic balance and some tangential-wind profile $v(r)$. For several different

types of vortices this results in the relationship $c_p\bar{\theta}_S[\pi_\infty(\delta) - \pi_0(\delta)] = \beta v_M^2$, where the constant $\beta = 0.5$ for a stagnant-core vortex, 1 for a Rankine combined vortex, 1.14 for Kuo's two-cell vortex, 1.74 for his one-cell vortex, and 1.68 for the Burgers–Rott vortex. For a steady nondiffusive flow, $\delta = 0$, $v = 0$, and $w_0(\delta) = u' = w' = 0$, and the maximum tangential velocity on the ground is given by the "thermodynamic speed limit" $v_M = (\text{CAPE}/\beta)^{1/2}$, where $\theta_0(z)$ is the potential temperature of a surface parcel lifted adiabatically to cloud base and pseudoadiabatically above cloud base. This limit pertains only to inviscid tornadoes with axial updrafts.

Based on an environmental sounding, Bluestein et al. (1993) calculated a CAPE of 3900 $m^2\ s^{-2}$ for the Red Rock, Oklahoma, tornado and a thermodynamic speed limit of 62 $m\ s^{-1}$ based on a Rankine combined vortex ($\beta = 1$). As discussed above, this is roughly one-half the observed wind speed measured somewhere below cloud base. Since this tornado was large, the inner part of the core may have been rotating slowly compared to the core wall, hence β may have been closer to 0.5, which would increase the speed limit to 88 $m\ s^{-1}$. Since the tornado was moving to the east-northeast at about 15 $m\ s^{-1}$ and the measurement was obtained when the tornado was northeast of the radar, the maximum tornado-relative wind speed may be only 105 $m\ s^{-1}$. By this reckoning the speed limit is broken not by a factor of 2, but by only 20%. To explain away the remaining 20% without invoking subsidence warming in the core, we could postulate that the measurements were made near the top of the tornado's boundary layer where inflowing parcels overshot their equilibrium radius by 20%. Or we might point out that the CAPE is relative to a pristine horizontally homogeneous environment, instead of the actual inhomogeneous surroundings that include the storm's cold pool (Lewellen 1976, 1993; Trapp and Davies-Jones 1997). These remarks are intended only to raise uncertainty, not to lend support to the thermodynamic speed limit that is based on constant equivalent potential temperature along the axis.

The simplest mechanism for breaking the thermodynamic speed limit is via subsidence in the core forced by a downward axial pressure-gradient force (Lilly 1969, 1976). The CAPE in (5.25) is now based on the temperature difference between a depressed (instead of lifted) parcel and the environment, resulting in a much higher speed limit based on constant potential temperature along the axis, which is labeled here the *upper thermodynamic speed limit*. Subsidence in the core can result in a much larger CAPE if the core is filled almost down to the ground with parcels that have entered a large tornado through its top near the equilibrium level. The core of such a tornado would be very stable (since $\partial\theta/\partial r < 0$; see section 5.4) and hence very warm because the air would descend dry adiabatically in the absence of turbulent mixing with air outside the core. There is limited observational evidence for the existence of tornadoes with hurricane-like eyes from Doppler radar observations of an echo-weak hole associated with a TVS (Johnson and Ziegler 1984; see also Wakimoto et al. 1996) and from mobile Doppler radar observation of a suspected strong downdraft near cloud base in a tornado (Wurman et al. 1996; see also Figs. 5.23 and 5.27).

For $\beta = 0.5$ both limits are commensurate with assuming a stagnant-core vortex in hydrostatic and cyclostrophic balance. The balanced state can be illustrated in the case of core subsidence with a two-layer atmosphere consisting of a troposphere of constant potential temperature θ_1 and a stratosphere of constant potential temperature θ_2, where $\theta_2 > \theta_1$ (Fig. 5.32a). The unperturbed tropopause is at $z = H$. Assume that a thunderstorm generates a vortex that draws θ_2 air down to the surface as shown in Fig. 5.32b. The new

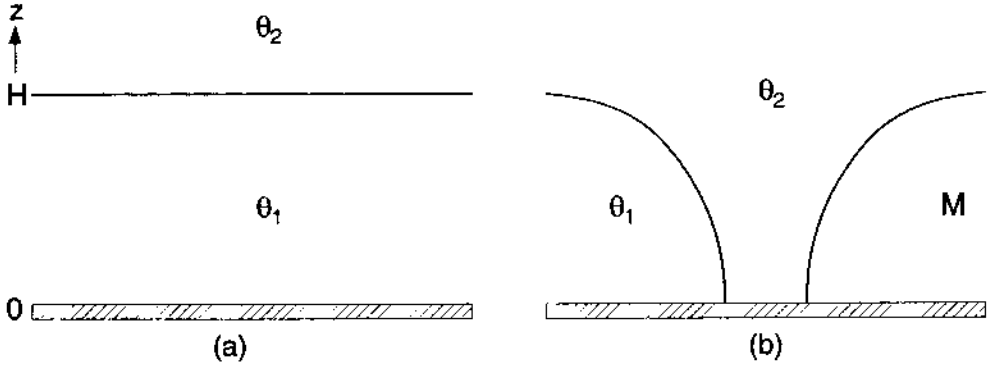

FIG. 5.32. (a) Equilibrium state in a two-layer atmosphere in the absence of rotation. The troposphere of constant potential temperature θ_1 is overlaid by a stratosphere of constant potential temperature θ_2 ($>\theta_1$). (b) Balanced inviscid vortex in the same two-layer atmosphere. There is no flow in the radial and vertical directions. An outer potential vortex of tropospheric air with constant angular momentum M surrounds a stagnant core of air drawn down from the stratosphere.

state has higher potential energy than did the original one so the transition requires (i) the addition of energy, which has to be supplied by the parent storm, and (ii) the prior presence of strong low-level rotation, probably the tornadic vortex in its formative stages, to provide the downward pressure-gradient force needed to draw down the θ_2 air. Figure 5.32b may represent an ideal state for tornadoes.

The core pressure deficit and maximum wind can be derived for the two-layer model as follows. The nondimensional pressure at height $z \leq H$ in the environment, characterized by constant potential temperature θ_1, is found by integrating (5.22) upward from the surface and assuming $\pi(\infty, 0) = 1$, and is given by $\pi(\infty, z) = 1 - gz/c_p\theta_1$. The nondimensional pressure at $z = H$ is independent of r and hence is $\pi(r, H) = 1 - gH/c_p\theta_1$. The pressure along the axis, found by integrating the hydrostatic equation downward from the tropopause, is $\pi(0, z) = \pi(0, H) + g(H - z)/c_p\theta_2$. The axial pressure deficit is

$$\Delta\pi(z) \equiv \pi(\infty, z) - \pi(0, z) = \frac{g}{c_p}\left(\frac{1}{\theta_1} - \frac{1}{\theta_2}\right)(H - z), \quad (5.26)$$

which also applies to the entire stagnant core. The Froude number based on the total height of the tornado, defined as $\mathrm{Fr} \equiv \{(c_p\theta/gH)/[\Delta\pi(0)/\Delta\theta/\theta)]\}^{1/2}$ (Lewellen 1993), is 1 for our two-layer model. In the outer potential part of the vortex centrifugal forces balance the inward pressure-gradient force. The maximum tangential velocity and the core radius at each level are given by

$$v_c(z) = [2c_p\theta_1\Delta\pi(z)] = \left[2g\left(1 - \frac{\theta_1}{\theta_2}\right)(H - z)\right]^{1/2} \quad (5.27)$$

and

$$r_c(z) = M/v_c(z). \quad (5.28)$$

These formulas for maximum pressure drop and tangential velocity can be generalized easily to include a general sounding and a general vortex core with potential temperatures $\theta_\infty(z)$ and $\theta_0(z)$, respectively. Now H becomes the height of the equilibrium level [where $\theta_0(H) = \theta_\infty(H)$]. Integrating the hydrostatic equation yields

$$\Delta\pi(z) = \frac{g}{c_p}[\overline{(1/\theta_\infty)} - \overline{(1/\theta_0)}](H - z), \quad (5.29)$$

where the overbar denotes average values between $H - z$ and H. The maximum wind is

$$v_c \approx \left\{\frac{gH}{\beta}\,\theta_\infty(0)[\overline{(1/\theta_\infty)} - \overline{(1/\theta_0)}]\right\}^{1/2}. \quad (5.30)$$

Adopting the sounding shown in Lilly (1976), we can use the formulas to make estimates of tornado parameters. Assuming that the source height of the subsiding air is 180 mb, $H = 13\,000$ m and $\theta_2 = 340$ K. Here $\theta_1 = 315$ K is representative of a mean tropospheric value of θ and $M = 2 \times 10^4$ m^2 s^{-1} is typical for a strong tornado. For a dry adiabatic core, these values yield a central pressure drop of 100 mb, a maximum tangential velocity of 137 m s^{-1}, a core radius of 146 m, and a ground temperature in the tornado of 57°C if the subsiding air reaches the ground unmodified (although such warm air has never been observed). The pressure drop and speed limit (with the translation speed added) seem to be reasonable *upper* bounds in the light of existing measurements. Higher values can be obtained by assuming that the air descends from 160 mb, the parcel equilibrium level, instead of 180 mb. With pseudoadiabatic descent, the surface pressure deficit and the maximum tangential wind speeds are only about 30% and 55%, respectively, of the above values.

In addition to the hydrostatic lowering of pressure, Eq. (5.25) offers two dynamical mechanisms for maintaining a large pressure deficit: the turbulent stress term (Ward 1972; Pauley 1989) and large vertical kinetic energy of parcels at the top of the corner region (Davies-Jones and Kessler 1974; Lewellen 1976; Snow and Pauley 1984; Fiedler and Rotunno 1986). These dynamical effects allow the lower thermodynamic speed limit to be broken without subsidence warming in the core (Lewellen 1976; Snow and Pauley 1984; Fiedler and Rotunno 1986). The dynamical mechanisms may also be responsible for the relatively larger pressure drops and associated higher wind speeds that occur in secondary vortices: Photogrammetric measurements in tornadoes (Forbes 1976) and laboratory vortices (Leslie 1977) and three-dimensional numerical modeling results (Rotunno 1984; Lewellen et al. 1997) show that tornado-relative winds may be 30%–50% higher in secondary vortices than in the azimuthally averaged flow.

Ward (1972) proposed that the low axial pressure near the surface could be maintained by turbulent stresses preventing filling of the vortex from above. Pauley's (1989) measurements support this conclusion, but the turbulent stress term does not seem to be important in the axial momentum budget in some axisymmetric numerical simulations (Walko 1988; Fiedler 1994).

The most complete explanation of the mechanism involving the vertical kinetic energy term is that due to Fiedler and Rotunno (1986). They suggest that, in some instances, intense tornadoes could be supercritical end-wall vortices with axial jets in their cores,

arising from the frictional interaction of a vortex with the ground; thus, as already explained, the vertical kinetic energy term is large for end-wall vortices and drowned vortex jumps. An example of a tornado of this type may be the narrow, intense, and well videographed Pampa, Texas, tornado of 8 June 1995, which lofted a flattened pickup truck 30 m in the air. Indications of vortex breakdowns in tornadoes have been reported by Hoecker (1960), Ward (1972), Burggraf and Foster (1977), and Pauley and Snow (1988). Because end-wall vortices are supercritical flows that do not allow upstream (i.e., downward) wave propagation, they can contain intense dynamical pressure drops that cannot be reduced by filling from above. With increasing circulation M, the end-wall vortex intensifies because $r_m \propto M^{-1/2}$, and $(\Delta p)_m \propto v_m^2 \propto M^3$. There is still a limit, however, on the maximum pressure drop that can be realized in a given parent updraft because adding more swirl to the flow eventually leads to the less intense subcritical vortex reaching the surface and preventing the more intense end-wall vortex from forming. Conversely, reducing the swirl leads to a less intense end-wall vortex and less disparity between upstream and downstream conditions that can be matched by a vortex breakdown further aloft (Fiedler and Rotunno 1986).

Fiedler and Rotunno estimated the intensity of a supercritical end-wall tornado by assuming that the maximum tangential velocity in the subcritical vortex aloft was $v_c = (\text{CAPE})^{1/2}$, the thermodynamic speed limit for a Rankine combined vortex. Applying their theoretical results that $v_m \approx 1.7 v_c$, $w_m \approx 2 v_m$, and $(\Delta p)_m \approx \rho w_m^2/2$ yields for $v_c = 65$ m s^{-1}, $v_m \sim 110$ m s^{-1}, $w_m \sim 220$ m s^{-1}, and $(\Delta p)_m \sim 242$ mb. The maximum inward velocity is about half of v_m according to Fiedler's (1994) model. These extreme values are aloft where measurements of axial pressure and vertical velocity are difficult to obtain. Can the simulator results and the theory be applied to tornadoes where the flow in the boundary layer and corner region is turbulent, the earth's surface is rougher than plywood, the flow force has a buoyancy term (Morton 1966, 1969), the termination of the tornado aloft may be radically different in the absence of an atmospheric counterpart to the baffle, the flow is no longer approximately incompressible at the estimated wind speeds, and the downstream conditions probably are not simply $v_c \approx 2.6\bar{w}$? The latter condition appears inconsistent because it makes $\bar{w} = (\text{CAPE})^{1/2}/2.6$, whereas $\bar{w} = (\text{CAPE})^{1/2}$ would seem more in keeping with observations. Regarding the first condition, however, even if the boundary layer and end-wall vortex are turbulent, the ratio v_m/v_c may still be around 2 (Chi 1977) or even 2.5 (Lewellen et al. 2000), although w_m/v_m may be reduced (to 1.4, as given by Lewellen et al. 2000; see also Fiedler and Rotunno 1986; Lewellen 1993).

The supercritical end-wall vortex tornado, although high velocity, is arguably not the most damaging at the ground (aside from hits from large falling objects ejected from the tornado) because its high winds and low pressure are located some 50 m above the ground in the axial jet very close to the axis. The wind damage in this type of tornado should be worst at treetop level, although the recent modeling study by Lewellen et al. (2000) suggests that the most significant damage might be much lower; the location of the extreme winds and pressure deficit makes observational verification (using current observing tools and strategies) of the theory and model almost impossible. The most damaging types of tornado should be the drowned vortex jump and large two-celled vortices with (or even sometimes without) secondary vortices. The majority of intense tornadoes should be of the latter type since it occurs over a much wider range of swirl ratios than the end-wall vortex and DVJ. A damage survey of the violent Union City tornado (Davies-Jones et al. 1978) gave indications that it was equally damaging to houses in its path when it was two-celled at the surface (damaging winds circulatory) as it was when it later became a smaller vortex with signs in the lowest few meters of strong low-level convergence into its center (and with damage and debris dispersal caused predominantly by winds that were in the same direction as tornado translation).

5.6. Concluding remarks

A buoyant updraft, rainy downdrafts, and a deep, mesocyclonic vortex (preexisting vertical vorticity) are tornadic supercell (nonsupercell) storm "ingredients." These are, to varying degrees, mutually dependent processes and interact in some way to yield a tornado. It is unlikely that a single such "recipe" can be generalized to all instances of tornadogenesis. For example, the exact sequence of events leading to tornado formation will depend, as alluded to in section 5.2, on whether or not the mechanism for the genesis of the near-ground mesocyclone is effectively baroclinic or barotropic.

Observationally, the basic mechanism for midlevel mesocyclogenesis (section 5.2) has been confirmed. Refuting or verifying other model- or theoretical-based mechanisms such as those involving near-ground mesocyclogenesis and the modes of tornadogenesis (section 5.3) may be hard to verify or refute with present data of tornadic storms. Similarly, much about the tornado structure deduced from models and theory, particularly that which governs tornado intensity (sections 5.4 and 5.5), awaits observational confirmation.

Current and future researchers are faced with additional yet related unresolved scientific issues too numerous to list here. One such issue regards the current inability among meteorologists to reliably forecast or even "nowcast" tornado intensity and longevity. Another that has critical operational implications is the

current lack of a means to discriminate tornadic storms from those storms that appear quantitatively and qualitatively identical to tornadic storms yet do not produce tornadoes. The exact nature of tornado demise remains speculative, as does the physics of the storm–boundary interactions that sometimes precede tornadogenesis. And, of course, we have yet to solve the mysteries of whether the cores of large tornadoes are warm and how the vortex terminates aloft. Solutions to these problems will require cooperation and complementary efforts among observationalists, modelers, and theoreticians.

Apart from limited temporal and spatial resolution in inadequately small temporal and spatial domains, datasets currently available for mesocyclone and tornadogenesis study also suffer from (i) lack of wind information in the lowest few hundred meters between the ground and the lowest elevation angle of a typical Doppler radar scan, where horizontal convergence and baroclinic generation of vorticity are concentrated; and (ii) lack of temperature and humidity measurements in the lowest 1–2 km in the vicinity of the wall cloud, tail cloud, and clear slot, and within the rear- and forward-flank downdraft regions. Data appropriate for investigations of tornado dynamics necessarily must have even higher temporal and spatial resolution. On both the mesocyclone and the tornado scales, a sufficient number of observations must be gathered to allow for generalization of the results.

In addition to fixed-site and mobile rawinsondes and surface mesonets that provide in situ measurements, collecting the needed data in the future will probably require remotely controlled instruments (perhaps aboard a remotely piloted aircraft; e.g., see Bluth et al. 1996) and/or other remote-sensing techniques, and yet will still be very challenging owing to the logistics of intercepting hazardous and quickly moving and evolving storms. Clearly, single- and coordinated multiple-Doppler radars will continue to play a prominent role in tornado and tornadic storm research. We emphasize the future importance of radars installed on mobile ground-based and airborne platforms (see sections 5.2 and 5.3), which can ease (albeit with their unique set of limitations) the primary shortcomings of ground-based, fixed-site radars. For example, owing to the tens of kilometers typical distance between the storm and the radar(s), the fixed-site data suffer from relatively coarse vertical resolution. Such degraded resolution and the related lack of data close to the ground diminish the accuracy of horizontal convergence calculations within the convective boundary layer and therefore of vertical velocity and subsequent retrieved variables (the computations of which are sensitive to vertical velocity). Another shortcoming is that the probability is low that a storm will pass through a fixed-site Doppler-radar network such that data can be collected to document tornado formation, maintenance, and decay. In contrast, an aircraft equipped with Doppler radar[2] can fly close to a storm at low levels and can follow it during its entire life cycle. An analogous statement can be made about ground-based mobile radars, with the caveat that the deployment and data collection are subject to the availability of a suitable road network.

These shortcomings aside, fixed-site radars will continue to provide invaluable information. Data from operational radars such as the WSR-88D and the Terminal Doppler Weather Radar can be used to compile large-sample statistics on observable storm attributes, to help focus research endeavors, and to improve warning operations. In addition, retrieval of the 3D wind in thunderstorms using single Doppler radar data has become possible recently using techniques based on assumptions of conservation of radar reflectivity or velocity stationarity (e.g., Tuttle and Foot 1990; Qiu and Xu 1992; Laroche and Zawadzki 1994; Shapiro et al. 1995; Zhang and Gal-Chen 1996; Sun and Crook 1997). In addition to their potential for storm diagnostic purposes (e.g. Sun and Crook 1998), the retrieved winds and subsequently (or concurrently) retrieved thermodynamic variables can be assimilated into numerical models, for the purpose of producing very short-term prognoses of the future state of the storm. Weygandt et al. (1998) have reported some success recently with such predictions of the 17 May 1981 Arcadia, Oklahoma, tornadic supercell. Storm-scale predictions (and also diagnoses) will be limited by the characteristics of the data sampling, as mentioned above, and additionally by the assumptions that underlie the single-Doppler retrieval techniques.

It is appropriate to close our review as did Davies-Jones (1986) with comments on tornado "modification." Numerous suggestions on tornado destruction/wind modification have been offered[3] (by meteorologists and nonmeteorologists alike) that purport to disrupt the flow in and around the tornado. An explosive device administered to the tornado by missiles is an example of one of the more popular ideas. Such an approach carries with it the grave consequences associated with a number of unintended results, the most obvious of which is damage to life and property by explosives themselves. Similarly, cloud seeding, if effective in enhancing rainfall, would have uncertain effects on tornado modification. For example, in storms with too little natural precipitation, it is plausible that an increase in rainfall would then allow the storm to support

[2] Details of radar scanning strategies, and how these radar scans comprise "pseudo-dual-Doppler" radar data, are given by Jorgensen et al. (1996). A discussion of airborne Doppler radar sampling limitations and of error sources in pseudo-dual-Doppler analyses can be found in Ray and Stephenson (1990) and elsewhere.

[3] It has been our experience that these tend to follow highly publicized tornado outbreaks with numerous fatalities such as the event on 3 May 1999 near Oklahoma City, Oklahoma.

the processes that lead to tornadogenesis! Other proposals are outlined by Davies-Jones (1986).

To our knowledge, none of these techniques have been advanced. Thus, as stated by Davies-Jones (1986), we are "probably many years away" from practical implementation of any such techniques, which will continue to be limited by the gaps in our understanding of tornadoes and tornadic storms. In the meantime, we recommend that steps be taken toward continued mitigation of loss of life, with appropriate structural engineering and building practices, installation of concrete-reinforced "safe rooms," public outreach and education on storm and tornado safety, and basic research on tornadoes and tornadic storms, with rapid transfer of these research results to the operational sector.

Acknowledgments. The authors wish to thank the members of the review panel, and in particular S. Lewellen and J. Snow, for their constructive comments on various versions of the manuscript. We are grateful to Joan O'Bannon for her time and effort in drafting many of the figures. The second author contributed to this chapter while he was a visiting scientist with the Mesoscale and Microscale Meteorology Division of the National Center for Atmospheric Research. The National Center for Atmospheric Research is sponsored by the National Science Foundation.

REFERENCES

Adlerman, E. J., K. K. Droegemeier, and R. Davies-Jones, 1999: A numerical simulation of cyclic mesocyclogenesis. *J. Atmos. Sci.*, **56,** 2045–2069.

Agee, E. M., 1969: Tornado Project activities at Purdue University. *Bull. Amer. Meteor. Soc.*, **50,** 806–807.

———, 1970: Purdue tornado project activities—Part II. *Bull. Amer. Meteor. Soc.*, **51,** 951.

———, J. T. Snow, and P. R. Clare, 1976: Multiple vortex features in the tornado cyclone and the occurrence of tornado families. *Mon. Wea. Rev.*, **104,** 552–563.

Atkins, N. T., M. L. Weisman, and L. J. Wicker, 1999: The influence of preexisting boundaries on supercell evolution. *Mon. Wea. Rev.*, **127,** 2910–2927.

Baker, G. L., and C. R. Church, 1979: Measurements of core radii and peak velocities in modeled atmospheric vortices. *J. Atmos. Sci.*, **36,** 2413–2424.

Barcilon, A., and P. G. Drazin, 1972: Dust devil formation. *Geophys. Fluid Dyn.*, **4,** 147–158.

Barnes, S. L., 1970: Some aspects of a severe, right-moving thunderstorm deduced from mesonet rawinsonde observations. *J. Atmos. Sci.*, **27,** 634–648.

———, 1978: Oklahoma thunderstorms on 29–30 April 1970. Part I: Morphology of a tornadic storm. *Mon. Wea. Rev.*, **106,** 673–684.

Batchelor, G. K., 1967: *An Introduction to Fluid Dynamics.* Cambridge University Press, 615 pp.

Bedard, A. J., Jr., and C. Ramzy, 1983: Surface meteorological observations in severe thunderstorms. Part I: Design details of TOTO. *J. Climate Appl. Meteor.*, **22,** 911–918.

Bergé, P., Y. Pomeau, and C. Vidal, 1984: *Order Within Chaos.* Wiley, 329 pp.

Bieringer, P., and P. S. Ray, 1996: A comparison of tornado warning lead times with and without NEXRAD Doppler radar. *Wea. Forecasting,* **11,** 47–52.

Binnie, A. M., and G. A. Hookings, 1948: Laboratory experiments on whirlpools. *Proc. Roy. Soc. London A,* **194,** 348–415.

Bluestein, H. B., 1980: The University of Oklahoma Severe Storms Intercept Project—1979. *Bull. Amer. Meteor. Soc.*, **61,** 560–567.

———, 1983a: Measurements in the vicinity of severe thunderstorms and tornadoes with TOTO: 1982–1983 results. Preprints, *13th Conf. on Severe Local Storms,* Tulsa, OK, Amer. Meteor. Soc., 89–92.

———, 1983b: Surface meteorological observations in severe thunderstorms. Part II: Field experiments with TOTO. *J. Climate Appl. Meteor.*, **22,** 919–930.

———, 1984: Photographs of the Canyon, TX storm on 26 May 1978. *Mon. Wea. Rev.*, **112,** 2521–2523.

———, 1985a: The formation of a "landspout" in a "broken-line" squall line in Oklahoma. Preprints, *14th Conf. on Severe Local Storms,* Indianapolis, IN, Amer. Meteor. Soc., 267–270.

———, 1985b: Wall clouds with eyes. *Mon. Wea. Rev.,* **113,** 1081–1085.

———, 1986: Visual aspects of the flanking line in severe thunderstorms. *Mon. Wea. Rev.*, **114,** 788–795.

———, 1994: High-based funnel clouds in the Southern Plains. *Mon. Wea. Rev.*, **122,** 2631–2638.

———, 1996: 3-D stereo photography of supercell tornadoes. Preprints, *18th Conf. on Severe Local Storms,* San Francisco, CA, Amer. Meteor. Soc., 469–470.

———, 1999a: A history of severe-storm intercept field programs. *Wea. Forecasting,* **14,** 558–577.

———, 1999b: *Tornado Alley: Monster Storms of the Great Plains.* Oxford University Press, 180 pp.

———, and C. Parks, 1983: A synoptic and photographic climatology of low-precipitation severe thunderstorms in the Southern Plains. *Mon. Wea. Rev.*, **111,** 2034–2046.

———, and W. P. Unruh, 1989: Observations of the wind field in tornadoes, funnel clouds, and wall clouds with a portable Doppler radar. *Bull. Amer. Meteor. Soc.*, **70,** 1514–1525.

———, and G. R. Woodall, 1990: Doppler-radar analysis of a low-precipitation severe storm. *Mon. Wea. Rev.*, **118,** 1640–1664.

———, and J. H. Golden, 1993: A review of tornado observations. *The Tornado: Its Structure, Dynamics, Prediction, and Hazards, Geophys. Monogr.*, No. 79, Amer. Geophys. Union, 319–352.

———, and W. P. Unruh, 1993: On the use of a portable FM-CW Doppler radar for tornado research. *The Tornado: Its Structure, Dynamics, Prediction, and Hazards, Geophys. Monogr.*, No. 79, Amer. Geophys. Union, 367–376.

———, and D. R. MacGorman, 1998: Evolution of cloud-to-ground lightning characteristics and storm structure in the Spearman, Texas, tornadic supercells of 31 May 1990. *Mon. Wea. Rev.*, **126,** 1451–1467.

———, and A. Pazmany, 2000: Observations of tornadoes and other convective phenomena with a mobile 3-mm wavelength, Doppler radar: The spring 1999 field experiment. *Bull. Amer. Meteor. Soc.*, **81,** 2939–2951.

———, W. P. Unruh, J. LaDue, H. Stein, and D. Speheger, 1993: Doppler-radar wind spectra of supercell tornadoes. *Mon. Wea. Rev.*, **121,** 2200–2221.

———, A. L. Pazmany, J. C. Galloway, and R. E. McIntosh, 1995: Studies of the substructure of severe convective storms using a mobile 3-mm wavelength Doppler radar. *Bull. Amer. Meteor. Soc.*, **76,** 2155–2169.

———, W. P. Unruh, D. C. Dowell, T. A. Hutchinson, T. M. Crawford, A. C. Wood, and H. Stein, 1997: Doppler radar analysis of the Northfield, Texas tornado of 25 May 1994. *Mon. Wea. Rev.*, **125,** 212–230.

Bluth, R. T., P. A. Durkee, J. H. Seinfeld, R. C. Flagan, L. M. Russell, P. A. Crowley, and P. Finn, 1996: Center for interdisciplinary remotely-piloted aircraft studies (CIRPAS). *Bull. Amer. Meteor. Soc.*, **77,** 2691–2699.

Bödewadt, U. T., 1940: Die Drehströmung über festem Grund. *Z. Angew Math. Mech.*, **20,** 241–253.

Borisenko, A. I., and I. E. Tarapov, 1979: *Vector and Tensor Analysis with Applications.* Dover, 257 pp.

Brady, R. H., and E. J. Szoke, 1989: A case study of nonmesocyclone tornado development in northeast Colorado: Similarities to waterspout formation. *Mon. Wea. Rev.*, **117,** 843–856.

Brandes, E. A., 1977: Gust front evolution and tornadogenesis as viewed by Doppler radar. *J. Appl. Meteor.*, **16,** 333–338.

———, 1978: Mesocyclone evolution and tornadogenesis: Some observations. *Mon. Wea. Rev.*, **106,** 995–1011.

———, 1981: Fine-structure of the Del City-Edmond tornado mesocirculation. *Mon. Wea. Rev.*, **109,** 635–647.

———, 1984a: Relationships between radar-derived thermodynamic variables and tornadogenesis. *Mon. Wea. Rev.*, **112,** 1033–1052.

———, 1984b: Vertical vorticity generation and mesocyclone sustenance in tornadic thunderstorms: The observational evidence. *Mon. Wea. Rev.*, **112,** 2253–2269.

———, R. P. Davies-Jones, and B. C. Johnson, 1988: Streamwise vorticity effects on supercell morphology and persistence. *J. Atmos. Sci.*, **45,** 947–963.

Brock, F. V., G. Lesins, and R. Walko, 1987: Measurement of pressure and air temperature near severe thunderstorms: An inexpensive and portable instrument. *Extended Abstracts, Sixth Symp. Meteorological Observations and Instrumentation,* New Orleans, LA, Amer. Meteor. Soc., 320–323.

Brooks, H. E., and R. B. Wilhelmson, 1993: Hodograph curvature and updraft intensity in numerically modeled supercells. *J. Atmos. Sci.*, **50,** 1824–1833.

———, C. A. Doswell III, and R. Davies-Jones, 1993: Environmental helicity and the maintenance and evolution of low-level mesocyclones. *The Tornado: Its Structure, Dynamics, Prediction, and Hazards, Geophys. Monogr.,* No. 79, Amer. Geophys. Union, 97–104.

———, ———, and J. Cooper, 1994a: On the environments of tornadic and nontornadic mesocyclones. *Wea. Forecasting,* **9,** 606–618.

———, ———, and R. B. Wilhelmson, 1994b: The role of midtropospheric winds in the evolution and maintenance of low-level mesocyclones. *Mon. Wea. Rev.*, **122,** 126–136.

Brown, J. M., and K. R. Knupp, 1980: The Iowa cyclonic-anticyclonic tornado pair and its parent thunderstorm. *Mon. Wea. Rev.*, **108,** 1626–1646.

Brown, R. A., D. W. Burgess, and K. C. Crawford, 1973: Twin tornado cyclones within a severe thunderstorm: Single Doppler radar observations. *Weatherwise,* **26,** 63–71.

———, L. R. Lemon, and D. W. Burgess, 1978: Tornado detection by pulsed Doppler radar. *Mon. Wea. Rev.*, **106,** 29–39.

Browning, K. A., 1964: Airflow and precipitation trajectories within severe local storms which travel to the right of the winds. *J. Atmos. Sci.*, **21,** 634–639.

———, 1986: Morphology and classification of middle-latitude thunderstorms. *Thunderstorm Morphology and Dynamics,* 2d ed., E. Kessler, Ed., University of Oklahoma Press, 133–152.

———, and C. R. Landry, 1963: Airflow within a tornadic thunderstorm. Preprints, *10th Weather Radar Conf.*, Washington, DC, Amer. Meteor. Soc., 116–122.

Burgers, J. M., 1948: A mathematical model illustrating the theory of turbulence. *Adv. Appl. Mech.*, **1,** 197–199.

Burgess, D. W., and R. P. Davies-Jones, 1979: Unusual tornadic storms in eastern Oklahoma on 5 December 1975. *Mon. Wea. Rev.*, **107,** 451–457.

———, and L. R. Lemon, 1990: Severe thunderstorm detection by radar. *Radar in Meteorology,* D. Atlas, Ed., Amer. Meteor. Soc., 619–647.

———, V. T. Wood, and R. A. Brown, 1982: Mesocyclone evolution statistics. Preprints, *12th Conf. on Severe Local Storms,* San Antonio, TX, Amer. Meteor. Soc., 84–89.

———, S. V. Vasiloff, R. P. Davies-Jones, D. S. Zrnic, and S. E. Frederickson, 1985: Recent NSSL work on windspeed measurement in tornadoes. *Proc. Fifth U.S. National Conf. of Wind Engineering,* Lubbock, TX, Texas Tech University, 1A-53–1A-60.

Burggraf, O. R., and M. R. Foster, 1977: Continuation or breakdown in tornado-like vortices. *J. Fluid Mech.*, **80,** 685–703.

———, K. Stewartson, and R. Belcher, 1971: Boundary layer induced by a potential vortex. *Phys. Fluids,* **14,** 1821–1833.

Carbone, R. E., 1983: A severe frontal rainband. Part II: Tornado parent vortex circulation. *J. Atmos. Sci.*, **40,** 2639–2654.

Chi, J., 1977: Numerical analysis of turbulent end-wall boundary layers of intense vortices. *J. Fluid Mech.*, **82,** 209–222.

Church, C. R., and J. T. Snow, 1979: The dynamics of natural tornadoes as inferred from laboratory simulations. *J. Rech. Atmos.*, **12,** 111–133.

———, and ———, 1985: Measurements of axial pressure in tornado-like vortices. *J. Atmos. Sci.*, **42,** 576–582.

———, and ———, 1993: Laboratory models of tornadoes. *The Tornado: Its Structure, Dynamics, Prediction, and Hazards, Geophys. Monogr.,* No. 79, Amer. Geophys. Union, 277–295.

———, ———, and E. M. Agee, 1977: Tornado vortex simulation at Purdue University. *Bull. Amer. Meteor. Soc.*, **58,** 900–908.

———, ———, G. L. Baker, and E. M. Agee, 1979: Characteristics of tornado-like vortices as a function of swirl ratio: A laboratory investigation. *J. Atmos. Sci.*, **36,** 1755–1776.

———, D. Burgess, C. Doswell, and R. Davies-Jones, Eds., 1993: *The Tornado: Its Structure, Dynamics, Prediction, and Hazards, Geophys. Monogr.,* No. 79, Amer. Geophys. Union, 637 pp.

Concannon, P. R., H. E. Brooks, and C. A. Doswell III, 2000: Climatological risk of strong and violent tornadoes in the United States. Preprints, *Second Conf. on Environmental Applications,* Long Beach, CA, Amer. Meteor. Soc., 212–219.

Cooley, J. R., 1978: Cold air funnel clouds. *Mon. Wea. Rev.*, **106,** 1368–1372.

Darkow, G. L., 1971: Periodic tornado production by long-lived parent thunderstorms. Preprints, *Seventh Conf. on Severe Local Storms,* Kansas City, MO, Amer. Meteor. Soc., 214–217.

Davies, J. M., 1993a: Hourly helicity, instability and EHI in forecasting supercell tornadoes. Preprints, *17th Conf. on Severe Local Storms,* St. Louis, MO, Amer. Meteor. Soc., 56–60.

———, 1993b: Small tornadic supercells in the central Plains. Preprints, *17th Conf. Severe Local Storms,* St. Louis, MO, Amer. Meteor. Soc., 305–309.

Davies-Jones, R. P., 1973: The dependence of core radius on swirl ratio in a tornado simulator. *J. Atmos. Sci.*, **30,** 1427–1430.

———, 1976: Laboratory simulations of tornadoes. *Proc. Symp. on Tornadoes: Assessment of Knowledge and Implications for Man,* Lubbock, TX, Texas Tech University, 151–174.

———, 1982: Observational and theoretical aspects of tornadogenesis. *Intense Atmospheric Vortices,* L. Bengtsson and J. Lighthill, Eds., Springer-Verlag, 175–189.

———, 1983: Tornado interception with mobile teams. *Instruments and Techniques for Thunderstorm Observation and Analysis. Vol. III, Thunderstorms: A Social, Scientific, and Technological Documentary,* E. Kessler, Ed., University of Oklahoma Press, 23–32.

———, 1984: Streamwise vorticity: The origin of updraft rotation in supercell storms. *J. Atmos. Sci.*, **41,** 2991–3006.

———, 1985: Dynamical interaction between an isolated convective cell and a veering environmental wind. Preprints, *14th Conf. on Severe Local Storms,* Indianapolis, IN, Amer. Meteor. Soc., 216–219.

———, 1986: Tornado dynamics. *Thunderstorm Morphology and Dynamics,* 2d ed., E. Kessler, Ed., University of Oklahoma Press, 197–236.

———, 1995: Tornadoes. *Sci. Amer.*, **273,** (2), 34–41.
———, 1996a: Formulas for the barotropic and baroclinic components of vorticity with applications to vortex formation near the ground. Preprints, *Seventh Conf. on Mesoscale Processes,* Reading, UK, Amer. Meteor. Soc., 14–16.
———, 1996b: Inclusion of boundary conditions on pressure in conceptual models of updraft-environment interaction. Preprints, *18th Conf. Severe Local Storms,* San Francisco, CA, Amer. Meteor. Soc., 713–717.
———, 2000a: A Lagrangian model for baroclinic genesis of mesoscale vortices. Part I: Theory. *J. Atmos. Sci.,* **57,** 715–736.
———, 2000b: Can the hook echo instigate tornadogenesis barotropically? Preprints, *20th Conf. on Severe Local Storms,* Orlando, FL, Amer. Meteor. Soc., 269–272.
———, and E. Kessler, 1974: Tornadoes. *Weather and Climate Modification,* W. N. Hess, Ed., Wiley, 552–595.
———, and H. E. Brooks, 1993: Mesocyclogenesis from a theoretical perspective. *The Tornado: Its Structure, Dynamics, Prediction, and Hazards, Geophys. Monogr.,* No. 79, Amer. Geophys. Union, 105–114.
———, D. W. Burgess, L. R. Lemon, and D. Purcell, 1978: Interpretation of surface marks and debris patterns from the 24 May 1973 Union City, Oklahoma, tornado. *Mon. Wea. Rev.,* **106,** 12–21.
———, D. Burgess, and M. Foster, 1990: Test of helicity as a tornado forecast parameter. Preprints, *16th Conf. on Severe Local Storms,* Kananaskis Park, AB, Canada, Amer. Meteor. Soc., 588–592.
Donaldson, R. J., and W. E. Lamkin, 1964: Visual observations beneath a developing tornado. *Mon. Wea. Rev.,* **92,** 326–328.
Donaldson, R. J., Jr., 1970: Vortex signature recognition by a Doppler radar. *J. Appl. Meteor.,* **9,** 661–670.
———, 1990: Foundations of severe storm detection by radar. *Radar in Meteorology,* D. Atlas, Ed., Amer. Meteor. Soc., 115–121.
Doswell, C. A., III, and D. W. Burgess, 1988: On some issues of United States tornado climatology. *Mon. Wea. Rev.,* **116,** 495–501.
———, and D. W. Burgess, 1993: Tornadoes and tornadic storms: A review of conceptual models. *The Tornado: Its Structure, Dynamics, Prediction, and Hazards, Geophys. Monogr.,* No. 79, Amer. Geophys. Union, 161–172.
———, and T. P. Grazulis, 1998: A demonstration of vortex configurations in an inexpensive tornado simulator. Preprints, *19th Conf. on Severe Local Storms,* Minneapolis, MN, Amer. Meteor. Soc., 85–88.
———, A. R. Moller, and H. E. Brooks, 1999: Storm spotting and public awareness since the first tornado forecasts of 1948. *Wea. Forecasting,* **14,** 544–557.
Doviak, R. J., and D. S. Zrnić, 1993: *Doppler Radar and Weather Observations.* Academic Press, 562 pp.
Dowell, D. C., and H. B. Bluestein, 1997: The Arcadia, Oklahoma, storm of 17 May 1981: Analysis of a supercell during tornadogenesis. *Mon. Wea. Rev.,* **125,** 2562–2582.
———, and ———, 2000: Conceptual models of cyclic supercell tornadogenesis. Preprints, *20th Conf. on Severe Local Storms,* Orlando, FL, Amer. Meteor. Soc., 259–262.
———, ———, and D. P. Jorgensen, 1997: Airborne Doppler radar analysis of supercells during COPS-91. *Mon. Wea. Rev.,* **125,** 365–383.
Droegemeier, K. K., S. M. Lazarus, and R. Davies-Jones, 1993: The influence of helicity on numerically simulated convective storms. *Mon. Wea. Rev.,* **121,** 2005–2029.
Dutton, J. A., 1976: *The Ceaseless Wind.* McGraw-Hill, 579 pp.
Emanuel, K. A., 1994: *Atmospheric Convection.* Oxford University Press, 580 pp.
Eskridge, R. E., and P. Das, 1976: Effect of a precipitation-driven downdraft on a rotating wind field: A possible trigger mechanism for tornadoes? *J. Atmos. Sci.,* **33,** 70–84.
Faller, A. J., 1963: An experimental study of the instability of the laminar Ekman layer. *J. Fluid Mech.,* **15,** 560–576.
Fiedler, B. H., 1989: Conditions for laminar flow in geophysical vortices. *J. Atmos. Sci.,* **46,** 252–259.
———, 1993: Numerical simulations of axisymmetric tornadogenesis in forced convection. *The Tornado: Its Structure, Dynamics, Prediction, and Hazards, Geophys. Monogr.,* No. 79, Amer. Geophys. Union, 41–48.
———, 1994: The thermodynamic speed limit and its violation in axisymmetric numerical simulations of tornado-like vortices. *Atmos.–Ocean,* **32,** 335–359.
———, 1995: On modeling tornadoes in isolation from the parent storm. *Atmos.–Ocean,* **33,** 501–512.
———, and R. Rotunno, 1986: A theory for the maximum windspeeds in tornado-like vortices. *J. Atmos. Sci.,* **43,** 2328–2340.
Forbes, G. S., 1976: Photogrammetric characteristics of the Parker tornado of April 3, 1974. *Proc. Symp. on Tornadoes: Assessment of Knowledge and Implications for Man,* Lubbock, TX, Texas Tech University, 58–77.
———, 1978: Three scales of motion associated with tornadoes. U.S. Nuclear Regulatory Commission Contract Rep. NUREG/CR-0363, 359 pp.
Fujita, T. T., 1958: Tornado cyclone: bearing system of tornadoes. *Proc. Seventh Weather Radar Conf.,* Miami Beach, FL, Amer. Meteor. Soc., K31–K38.
———, 1959: Detailed analysis of the Fargo tornadoes of June 20, 1957. U.S. Weather Bureau Tech. Rep. 5, Severe Local Storms Project, University of Chicago, 29 pp. plus figures.
———, 1963: Analytical mesometeorology: A review. *Severe Local Storms, Meteor. Monogr.* No. 27, Amer. Meteor. Soc., 77–125.
———, 1973: Tornadoes around the world. *Weatherwise,* **26,** 56–62 78–83.
———, 1981: Tornadoes and downbursts in the context of generalized planetary scales. *J. Atmos. Sci.,* **38,** 1511–1534.
———, 1985: The downburst. Satellite and Mesometeorology Research Project (SMRP), Dept. of Geophysical Sciences, University of Chicago, 122 pp.
———, 1993: Plainfield tornado of August 28, 1990. *The Tornado: Its Structure, Dynamics, Prediction, and Hazards, Geophys. Monogr.* No. 79, Amer. Geophys. Union, 1–17.
———, and R. M. Wakimoto, 1982: Anticyclonic tornadoes in 1980 and 1981. Preprints, *12th Conf. on Severe Local Storms,* San Antonio, TX, Amer. Meteor. Soc., 401–404.
———, and B. E. Smith, 1993: Aerial surveys and photography of tornado and microburst damage. *The Tornado: Its Structure, Dynamics, Prediction, and Hazards, Geophys. Monogr.,* No. 79, Amer. Geophys. Union, 479–493.
———, G. S. Forbes, and T. A. Umenhofer, 1976: Close-up view of 20 March 1976 tornadoes: Sinking cloud tops to suction vortices. *Weatherwise,* **29,** 116–131, 145.
Garrett, R. A., and V. D. Rockney, 1962: Tornadoes in northeastern Kansas, 19 May 1960. *Mon. Wea. Rev.,* **90,** 231–240.
Gilmore, M. S., and L. J. Wicker, 1998: The influence of midtropospheric dryness on supercell morphology and evolution. *Mon. Wea. Rev.,* **126,** 943–958.
Golden, J. H., 1974a: The life-cycle of Florida Keys' waterspouts, I. *J. Appl. Meteor.,* **13,** 676–692.
———, 1974b: Scale-interaction implications for the waterspout life cycle. II. *J. Appl. Meteor.,* **13,** 693–709.
———, 1976: An assessment of wind speeds in tornadoes. *Proc. Symp. on Tornadoes,* Lubbock, TX, Texas Tech University, 5–42.
———, and B. J. Morgan, 1972: The NSSL/Notre Dame tornado intercept program, spring 1972. *Bull. Amer. Meteor. Soc.,* **53,** 1178–1180.
———, and D. Purcell, 1978a: Airflow characteristics around the Union City tornado. *Mon. Wea. Rev.,* **106,** 22–28.
———, and ———, 1978b: Life-cycle of the Union City, OK tornado and comparison with waterspouts. *Mon. Wea. Rev.,* **106,** 3–11.

Grasso, L. D., and W. R. Cotton, 1995: Numerical simulation of a tornado vortex. *J. Atmos. Sci.*, **52**, 1192–1203.

Grazulis, T. P., 1993: *Significant Tornadoes 1680–1991*. Environmental Films, 1326 pp.

Hane, C. E., and P. S. Ray, 1985: Pressure and buoyancy fields derived from Doppler radar in a tornadic thunderstorm. *J. Atmos. Sci.*, **42**, 18–35.

Harlow, F. H., and L. R. Stein, 1974: Structural analysis of tornado-like vortices. *J. Atmos. Sci.*, **31**, 2081–2098.

Heymsfield, G. M., 1978: Kinematic and dynamic aspects of the Harrah tornadic storm analyzed from dual-Doppler radar data. *Mon. Wea. Rev.*, **106**, 233–254.

Hoecker, W. H., 1960: Wind speed and airflow patterns in the Dallas tornado of April 2 1957. *Mon. Wea. Rev.*, **88**, 167–180.

Holle, R. L., and M. W. Maier, 1980: Tornado formation from downdraft interaction in the FACE network. *Mon. Wea. Rev.*, **108**, 1010–1028.

Howard, L. N., and A. S. Gupta, 1962: On the hydrodynamic and hydromagnetic stability of swirling flows. *J. Fluid Mech.*, **14**, 463–476.

Howells, P. A. C., R. Rotunno, and R. K. Smith, 1988: A comparative study of atmospheric and laboratory-analogue numerical tornado-vortex models. *Quart. J. Roy. Meteor. Soc.*, **114**, 801–822.

Istok, M. J., and R. J. Doviak, 1986: Analysis of the relation between Doppler spectral width and thunderstorm turbulence. *J. Atmos. Sci.*, **43**, 2199–2214.

Jensen, B., T. P. Marshall, M. A. Mabey, and E. N. Rasmussen, 1983: Storm scale structure of the Pampa storm. Preprints, *13th Conf. on Severe Local Storms*, Tulsa, OK, Amer. Meteor. Soc., 85–88.

Johnson, B. C., and C. L. Ziegler, 1984: Doppler observations and retrieved thermal and microphysical variables for the Binger tornadic storm. Preprints, *22d Weather Radar Conf.*, Zurich, Switzerland, Amer. Meteor. Soc., 31–36.

Johnson, K. W., P. S. Ray, B. C. Johnson, and R. P. Davies-Jones, 1987: Observations related to the rotational dynamics of the 20 May 1977 tornadic storms. *Mon. Wea. Rev.*, **115**, 2463–2478.

Jorgensen, D. P., T. Matejka, and J. D. DuGranrut, 1996: Multi-beam techniques for deriving wind fields from airborne Doppler radars. *J. Meteor. Atmos. Phys.*, **59**, 83–104.

Kanak, K. M., and D. K. Lilly, 1996: The linear stability and structure of convection in a mean circular shear. *J. Atmos. Sci.*, **53**, 2578–2593.

Kennedy, P. C., N. E. Westcott, and R. W. Scott, 1993: Single-Doppler radar observations of a mini-supercell tornadic thunderstorm. *Mon. Wea. Rev.*, **121**, 1860–1870.

Kessler, E., Ed., 1986: *Thunderstorm Morphology and Dynamics*. 2d ed. University of Oklahoma Press, 411 pp.

Klemp, J. B., 1987: Dynamics of tornadic thunderstorms. *Ann. Rev. Fluid Mech.*, **19**, 369–402.

———, and R. Rotunno, 1983: A study of the tornadic region within a supercell thunderstorm. *J. Atmos. Sci.*, **40**, 359–377.

———, R. B. Wilhelmson, and P. S. Ray, 1981: Observed and numerically simulated structure of a mature supercell thunderstorm. *J. Atmos. Sci.*, **38**, 1558–1580.

Kuo, H. L., 1966: On the dynamics of convective atmospheric vortices. *J. Atmos. Sci.*, **23**, 25–42.

———, 1967: Note on the similarity solutions of the vortex equations in an unstably stratified atmosphere. *J. Atmos. Sci.*, **24**, 95–97.

Laroche, S., and I. Zawadsky, 1994: A variational analysis method for the retrieval of three-dimensional wind field from single-Doppler data. *J. Atmos. Sci.*, **51**, 2664–2682.

Lee, B. D., and R. B. Wilhelmson, 1997: The numerical simulation of nonsupercell tornadogenesis. Part II: Evolution of a family of tornadoes along a weak outflow boundary. *J. Atmos. Sci.*, **54**, 2387–2415.

Lemon, L. R., and C. A. Doswell III, 1979: Severe thunderstorm evolution and mesocyclone structure as related to tornadogenesis. *Mon. Wea. Rev.*, **107**, 1184–1197.

———, D. W. Burgess, and R. A. Brown, 1978: Tornadic storm airflow and morphology derived from single-Doppler radar measurements. *Mon. Wea. Rev.*, **106**, 48–61.

Leslie, F. W., 1977: Surface roughness effects on suction vortex formation: A laboratory simulation. *J. Atmos. Sci.*, **34**, 1022–1027.

Leslie, L. M., 1971: The development of concentrated vortices: A numerical study. *J. Fluid Mech.*, **48**, 1–21.

Lewellen, D. C., W. S. Lewellen, and J. Xia, 2000: The influence of a local swirl ratio on tornado intensification near the surface. *J. Atmos. Sci.*, **57**, 527–544.

Lewellen, W. S., 1976: Theoretical models of the tornado vortex. *Proc. Symp. on Tornadoes: Assessment of Knowledge and Implications for Man*, Lubbock, TX, Texas Tech University, 107–143.

———, 1993: Tornado vortex theory. *The Tornado: Its Structure, Dynamics, Prediction, and Hazards, Geophys. Monogr.*, No. 79, Amer. Geophys. Union, 19–39.

———, and Y. P. Sheng, 1980: Modeling tornado dynamics. U.S. Nuclear Regulation Committee Rep. NUREG/CR-2585, Washington, DC.

———, D. C. Lewellen, and R. I. Sykes, 1997: Large-eddy simulation of a tornado's interaction with the surface. *J. Atmos. Sci.*, **54**, 581–605.

Lilly, D. K., 1969: Tornado dynamics. NCAR Manuscript 69-117. [Available from National Center for Atmospheric Research, P.O. Box 3000 Boulder, CO 80307-3000.]

———, 1976: Sources of rotation and energy in the tornado. *Proc. Symp. on Tornadoes: Assessment of Knowledge and Implications for Man*, Lubbock, TX, Texas Tech University, 145–150.

———, 1982: The development and maintenance of rotation in convective storms. *Intense Atmospheric Vortices*, L. Bengtsson and J. Lighthill, Eds., Springer-Verlag, 149–160.

———, 1983: Dynamics of rotating thunderstorms. *Mesoscale Meteorology—Theories, Observations and Models*, D. K. Lilly and T. Gal-Chen, Eds., Reidel, 531–543.

———, 1986: The structure, energetics and propagation of rotating convective storms. Part I: Energy exchange with the mean flow. *J. Atmos. Sci.*, **43**, 113–125.

Long, R. R., 1958: Vortex motion in a viscous fluid. *J. Meteor.*, **15**, 108–112.

Maddox, R. A., J. R. Hoxit, and C. F. Chappell, 1980: Study of tornadic thunderstorm interactions with thermal boundaries. *Mon. Wea. Rev.*, **108**, 322–336.

Magsig, M. A., and J. T. Snow, 1998: Long-distance debris transport by tornadic thunderstorms. Part I: The 7 May 1995 supercell thunderstorm. *Mon. Wea. Rev.*, **126**, 1430–1449.

Markowski, P. M., 2000: Surface thermodynamic characteristics of RFDs as measured by a mobile mesonet. Preprints, *20th Conf. on Severe Local Storms*, Orlando, FL, Amer. Meteor. Soc., 251–254.

———, J. M. Straka, and E. N. Rasmussen, 1998a: A preliminary investigation of the importance of helicity location in the hodograph. Preprints, *19th Conf. on Severe Local Storms*, Minneapolis, MN, Amer. Meteor. Soc., 230–233.

———, E. N. Rasmussen, and J. M. Straka, 1998b: The occurrence of tornadoes in supercells interacting with boundaries during VORTEX-95. *Wea. Forecasting*, **13**, 852–859.

Maxworthy, T., 1972: On the structure of concentrated columnar vortices. *Astronaut. Acta*, **17**, 363–374.

———, 1973: Vorticity source for large scale dust devils and other comments on naturally occurring vortices. *J. Atmos. Sci.*, **30**, 1717–1720.

———, 1982: The laboratory modelling of atmospheric vortices: A critical review. *Intense Atmospheric Vortices*, L. Bengtsson and J. Lighthill, Eds., Springer-Verlag, 229–246.

McCaul, E. W., 1993: Observations and simulations of hurricane-spawned tornadic storms. *The Tornado: Its Structure, Dynam-*

ics, Prediction, and Hazards, Geophys. Monogr. No. 79, Amer. Geophys. Union, 119–142.

Moller, A., 1978: The improved NWS storm spotters' training program at Ft. Worth, Tex. *Bull. Amer. Meteor. Soc.*, **59,** 1574–1582.

———, C. Doswell, J. McGinley, S. Tegtmeier, and R. Zipser, 1974: Field observations of the Union City tornado in Oklahoma. *Weatherwise,* **27,** 68–77.

Morton, B. R., 1966: Geophysical vortices. *Progr. Aeronaut. Sci.*, **7,** 145–193.

———, 1969: The strength of vortex and swirling core flows. *J. Fluid Mech.*, **38,** 315–333.

Mullen, J. B., and T. Maxworthy, 1977: A laboratory model of dust devil vortices. *Dyn. Atmos. Oceans,* **1,** 181–214.

Newton, C. W., and H. R. Newton, 1959: Dynamical interactions between large convective clouds and environment with vertical shear. *J. Meteor.*, **16,** 483–496.

Novlan, D. J., and W. M. Gray, 1974: Hurricane-spawned tornadoes. *Mon. Wea. Rev.*, **102,** 476–488.

Pauley, R. L., 1989: Laboratory measurements of axial pressure in two-celled tornado-like vortices. *J. Atmos. Sci.*, **46,** 3392–3399.

———, and J. T. Snow, 1988: On the kinematics and dynamics of the 18 June 1986 Minneapolis tornado. *Mon. Wea. Rev.*, **116,** 2731–2736.

———, C. R. Church, and J. T. Snow, 1982: Measurements of maximum surface pressure deficits in modeled atmospheric vortices. *J. Atmos. Sci.*, **39,** 369–377.

Peterson, R. E., Ed., 1976: *Proc. Symp. on Tornadoes: Assessment of Knowledge and Implications for Man,* Lubbock, TX, Texas Tech University, 696 pp.

Pfost, R. L., and A. E. Gerard, 1997: "Bookend vortex" induced tornadoes along the Natchez Trace. *Wea. Forecasting,* **12,** 572–580.

Proctor, F. H., 1988: Numerical solution of an isolated microburst. Part I: Dynamics and structure. *J. Atmos. Sci.*, **45,** 3137–3160.

Qui, C.-J., and Q. Xu, 1992: A simple adjoint method of wind analysis for single-Doppler radar. *J. Atmos. Oceanic Technol.*, **9,** 588–598.

Rasmussen, E. N., 1995: VORTEX operations plan. 141 pp. [Available from the National Severe Storms Laboratory, 1313 Halley Circle, Norman, OK 73069.]

———, and R. B. Wilhelmson, 1983: Relationships between storm characteristics and 1200 GMT hodographs. low-level shear, and stability. Preprints, *13th Conf. on Severe Local Storms,* Tulsa, OK, Amer. Meteor. Soc., J5–J8.

———, and J. M. Straka, 1996: Mobile mesonet observations of tornadoes during VORTEX-95. Preprints, *18th Conf. on Severe Local Storms,* San Francisco, CA, Amer. Meteor. Soc., 1–5.

———, and ———, 1998: Variations in supercell morphology. Part I: Observations of the role of upper-level storm-relative flow. *Mon. Wea. Rev.*, **126,** 2406–2421.

———, ———, R. Davies-Jones, C. A. Doswell, F. H. Carr, M. D. Eilts, and D. R. MacGorman, 1994: Verification of the origins of rotation in tornadoes experiment: VORTEX. *Bull. Amer. Meteor. Soc.*, **75,** 995–1006.

———, S. Richardson, J. M. Straka, P. M. Markowski, and D. O. Blanchard, 2000: The association of significant tornadoes with a baroclinic boundary on 2 June 1995. *Mon. Wea. Rev.*, **128,** 174–191.

Ray, P. S., and M. Stephenson, 1990: Assessment of the geometric and temporal errors associated with airborne Doppler radar measurements of a convective storm. *J. Atmos. Oceanic Technol.*, **7,** 206–217.

———, C. L. Ziegler, W. Bumgarner, and R. J. Serafin, 1980: Single- and multiple-Doppler radar observations of tornadic storms. *Mon. Wea. Rev.*, **108,** 1607–1625.

———, B. C. Johnson, K. W. Johnson, J. S. Bradberry, J. J. Stephens, K. K. Wagner, R. B. Wilhelmson, and J. B. Klemp, 1981: The morphology of several tornadic storms on 20 May 1977. *J. Atmos. Sci.*, **38,** 1643–1663.

Rayleigh, Lord, 1916: On the dynamics of revolving fluids. *Proc. Roy. Soc. London A,* **93,** 148–154.

Rothfusz, L. P., and D. K. Lilly, 1989: Quantitative and theoretical analysis of an experimental helical vortex. *J. Atmos. Sci.*, **46,** 2265–2279.

Rott, N., 1958: On the viscous core of a line vortex. *Z. Angew. Math. Physik,* **96,** 543–553.

Rotunno, R., 1977: Numerical simulation of a laboratory vortex. *J. Atmos. Sci.*, **34,** 1942–1956.

———, 1978: A note on the stability of a cylindrical vortex sheet. *J. Fluid Mech.*, **87,** 761–771.

———, 1979: A study in tornado-like vortex dynamics. *J. Atmos. Sci.*, **36,** 140–155.

———, 1981: On the evolution of thunderstorm rotation. *Mon. Wea. Rev.*, **109,** 577–586.

———, 1984: An investigation of a three-dimensional asymmetric vortex. *J. Atmos. Sci.*, **41,** 283–298.

———, 1986: Tornadoes and tornadogenesis. *Mesoscale Meteorology and Forecasting,* P. S. Ray, Ed., Amer. Meteor. Soc., 414–436.

———, and J. B. Klemp, 1982: The influence of the shear-induced pressure gradient on thunderstorm motion. *Mon. Wea. Rev.*, **110,** 136–151.

———, and ———, 1985: On the rotation and propagation of simulated supercell thunderstorms. *J. Atmos. Sci.*, **42,** 271–292.

Saffman, P. G., 1992: *Vortex Dynamics.* Cambridge University Press, 311 pp.

Schlesinger, R. E., 1978: A three-dimensional model of an isolated thunderstorm: Part I. Comparative experiments for variable ambient wind shear. *J. Atmos. Sci.*, **35,** 690–713.

Schlichting, H., 1960: *Boundary Layer Theory.* 4th ed. McGraw-Hill, 647 pp.

Scorer, R. S., 1978: *Environmental Aerodynamics.* Ellis Horwood, 488 pp.

Shapiro, A. H., 1972: Vorticity. *Illustrated Experiments in Fluid Mechanics, The National Committee for Fluid Mechanics Films Book of Film Notes,* The MIT Press, 63–74.

Shapiro, A., S. Ellis, and J. Shaw, 1995: Single-Doppler retrievals with Phoenix II data: Clear air and microburst wind retrievals in the planetary boundary layer. *J. Atmos. Sci.*, **52,** 1265–1287.

Smith, D. R., 1987: Effect of boundary conditions on numerically simulated vortices. *J. Atmos. Sci.*, **44,** 648–656.

Smith, R. K., and L. M. Leslie, 1978: Tornadogenesis. *Quart. J. Roy. Meteor. Soc.*, **104,** 189–199.

———, and ———, 1979: A numerical study of tornadogenesis in a rotating thunderstorm. *Quart. J. Roy. Meteor. Soc.*, **105,** 107–127.

Smith, R. L., and D. W. Holmes, 1961: Use of Doppler radar in meteorological observations. *Mon. Wea. Rev.*, **89,** 1–7.

Snow, J. T., 1982: A review of recent advances in tornado vortex dynamics. *Rev. Geophys. Space Phys.*, **20,** 953–964.

———, 1984: The Tornado. *Sci. Amer.*, **250** (4), 56–66.

———, and R. L. Pauley, 1984: On the thermodynamic method for estimating tornado windspeeds. *J. Climate Appl. Meteor.*, **23,** 1465–1468.

———, C. R. Church, and B. J. Barnhart, 1980: An investigation of the surface pressure fields beneath simulated tornado cyclones. *J. Atmos. Sci.*, **37,** 1013–1026.

———, A. L. Wyatt, A. K. McCarthy, and E. K. Bishop, 1995: Fallout of debris from tornadic thunderstorms: An historical perspective and two examples from VORTEX. *Bull. Amer. Meteor. Soc.*, **76,** 1777–1790.

Sreenivasan, K. R., 1985: Transition and turbulence in fluid flows and low-dimensional chaos. *Frontiers in Fluid Mechanics,* S. H. Davis and J. L. Lumley, Eds., Springer-Verlag. 41–67.

Straka, J. M., E. N. Rasmussen, and S. E. Fredrickson, 1996: A mobile mesonet for finescale meteorological observations. *J. Atmos. Oceanic Technol.*, **13,** 921–936.

Stumpf, G. J., A. Witt, E. D. Mitchell, P. L. Spencer, J. T. Johnson, M. D. Eilts, K. W. Thomas, and D. W. Burgess, 1998: The National Severe Storms Laboratory mesocyclone detection algorithm for the WSR-88D. *Wea. Forecasting,* **13,** 304–326.

Sullivan, R. D., 1959: A two-cell vortex solution of the Navier-Stokes equations. *J. Aerospace Sci.,* **26,** 767–768.

Sun, J., and N. A. Crook, 1997: Dynamical and microphysical retrieval from Doppler radar observations using a cloud model and its adjoint. Part I: Model development and simulated data experiments. *J. Atmos. Sci.,* **54,** 1642–1661.

———, and ———, 1998: Dynamical and microphysical retrieval from Doppler radar observations using a cloud model and its adjoint. Part II: Retrieval experiments of an observed Florida convective storm. *J. Atmos. Sci.,* **55,** 835–852.

Taylor, E. S., 1972: Secondary flow. *Illustrated Experiments in Fluid Mechanics, The National Committee for Fluid Mechanics Films Book of Film Notes,* The MIT Press, 97–104.

Trapp, R. J., 1999: Observations of nontornadic low-level mesocyclones and attendant tornadogenesis failure during VORTEX. *Mon. Wea. Rev.,* **127,** 1693–1705.

———, 2000: A clarification of vortex breakdown and tornadogenesis. *Mon. Wea. Rev.,* **128,** 888–895.

———, and B. H. Fiedler, 1995: Tornado-like vortexgenesis in a simplified numerical model. *J. Atmos. Sci.,* **52,** 3757–3778.

———, and R. Davies-Jones, 1997: Tornadogenesis with and without a dynamic pipe effect. *J. Atmos. Sci.,* **54,** 113–133.

———, E. D. Mitchell, G. A. Tipton, D. A. Effertz, A. I. Watson, D. L. Andra, and M. A. Magsig, 1999: Descending and nondescending tornadic vortex signatures detected by WSR-88D's. *Wea. Forecasting,* **14,** 625–639.

Truesdell, C., 1954: *The Kinematics of Vorticity.* Indiana University Press, 232 pp.

Tuttle, J. D., and G. B. Foote, 1990: Determination of the boundary-layer airflow from a single Doppler radar. *J. Atmos. Oceanic Technol.,* **7,** 218–232.

Wakimoto, R. M., and J. W. Wilson, 1989: Non-supercell tornadoes. *Mon. Wea. Rev.,* **117,** 1113–1140.

———, and B. E. Martner, 1992: Observations of a Colorado tornado. Part II: Combined photogrammetric and Doppler radar analysis. *Mon. Wea. Rev.,* **120,** 522–543.

———, and N. T. Atkins, 1996: Observations on the origins of rotation: The Newcastle tornado during VORTEX 94. *Mon. Wea. Rev.,* **124,** 384–407.

———, and C. Liu, 1998: The Garden City, Kansas, storm during VORTEX 95. Part II: The wall cloud and tornado. *Mon. Wea. Rev.,* **126,** 393–408.

———, and H. Cai, 2000: Analysis of a nontornadic storm during VORTEX 95. *Mon. Wea. Rev.,* **128,** 565–592.

———, W.-C. Lee, H. B. Bluestein, C.-H. Liu, and P. H. Hildebrand, 1996: ELDORA observations during VORTEX 95. *Bull. Amer. Meteor. Soc.,* **77,** 1465–1481.

———, C. Liu, and H. Cai, 1998: The Garden City, Kansas, storm during VORTEX 95. Part I: Overview of the storm's life cycle and mesocyclogenesis. *Mon. Wea. Rev.,* **126,** 372–392.

Walko, R. L., 1988: Plausibility of substantial dry adiabatic subsidence in a tornado core. *J. Atmos. Sci.,* **45,** 2251–2267.

———, 1993: Tornado spin-up beneath a convective cell: Required basic structure of the near-field boundary layer winds. *The Tornado: Its Structure, Dynamics, Prediction, and Hazards, Geophys. Monogr.,* No. 79, Amer. Geophys. Union, 89–95.

Ward, N. B., 1972: The exploration of certain features of tornado dynamics using a laboratory model. *J. Atmos. Sci.,* **29,** 1194–1204.

———, and A. B. Arnett Jr., 1963: Some relations between surface wind fields and radar echoes. *Conf. Review, Third Conf. on Severe Local Storms,* Urbana, IL, Amer. Meteor. Soc.

Weisman, M. L., and J. B. Klemp, 1982: The dependence of numerically simulated convective storms on vertical wind shear and buoyancy. *Mon. Wea. Rev.,* **110,** 504–520.

———, and ———, 1984: The structure and classification of numerically simulated convective storms in directionally varying wind shears. *Mon. Wea. Rev.,* **112,** 2479–2498.

Weygandt, S. S., A. Shapiro, and K. K. Droegemeier, 1998: The use of wind and thermodynamic retrievals to create initial forecast fields from single-Doppler observations of a supercell thunderstorm. Preprints, *16th Conf. on Weather Analysis and Forecasting,* Phoenix, AZ, Amer. Meteor. Soc., 286–288.

Wicker, L. J., 1996: The role of near surface wind shear on low-level mesocyclone generation and tornadoes. Preprints, *18th Conf. on Severe Local Storms,* San Francisco, CA, Amer. Meteor. Soc., 115–119.

———, and R. B. Wilhelmson, 1995: Simulation and analysis of tornado development and decay within a three-dimensional supercell thunderstorm. *J. Atmos. Sci.,* **52,** 2675–2703.

Wiin-Nielsen, A., 1973: *Compendium of Meteorology for Class I and II Personnel.* Vol. 1, Part 1, *Dynamic Meteorology,* World Meteorological Organization, Geneva, 334 pp.

Wilczak, J. M., T. W. Christian, D. E. Wolfe, R. J. Zamora, and B. Stankov, 1992: Observations of a Colorado tornado. Part I: Mesoscale environment and tornadogenesis. *Mon. Wea. Rev.,* **120,** 497–520.

Wilhelmson, R. B., and J. B. Klemp, 1978: A numerical study of storm splitting that leads to long-lived storms. *J. Atmos. Sci.,* **35,** 1974–1986.

Wilkins, E. M., 1988: Influence of Neil Ward's simulator on tornado research. CIMMS Rep. 87, Cooperative Institute for Mesoscale Meteorological Studies, 64 pp.

———, and C. J. Diamond, 1987: Effects of convection cell geometry on simulated tornadoes. *J. Atmos. Sci.,* **44,** 140–147.

Wilson, J. W., G. B. Foote, N. A. Crook, J. C. Fankhauser, C. G. Wade, J. D. Tuttle, and D. K. Mueller, 1992: The role of boundary-layer convergence zones and horizontal rolls in the initiation of thunderstorms: A case study. *Mon. Wea. Rev.,* **120,** 1785–1815.

Wilson, T., and R. Rotunno, 1986: Numerical simulation of a laminar end-wall vortex and boundary layer. *Phys. Fluids,* **29,** 3993–4005.

Winn, W. P., S. J. Hunyady, and G. D. Aulich, 1999: Pressure at the ground within and near a large tornado. *J. Geophys. Res.,* **104** (D18), 22 067–22 082.

Witt, A., M. D. Eilts, G. J. Stumpf, E. D. Mitchell, J. T. Johnson, and K. W. Thomas, 1998: Evaluating the performance of the WSR-88D severe storm detection algorithms. *Wea. Forecasting,* **13,** 513–518.

Wurman, J., and S. Gill, 2000: Finescale radar observations of the Dimmitt, Texas (2 June 1995), tornado. *Mon. Wea. Rev.,* **128,** 2135–2164.

———, J. M. Straka, and E. N. Rasmussen, 1996: Fine-scale Doppler radar observations of tornadoes. *Science,* **272,** 1774–1777.

———, ———, ———, M. Randall, and A. Zahrai, 1997: Design and deployment of a portable, pencil-beam, pulsed, 3-cm Doppler radar. *J. Atmos. Oceanic Technol.,* **14,** 1502–1512.

Zhang, J., and T. Gal-Chen, 1996: Single-Doppler wind retrieval in the moving frame of reference. *J. Atmos. Sci.,* **53,** 2609–2623.

Ziegler, C. L., E. N. Rasmussen, T. R. Shepherd, A. I. Watson, and J. M. Straka, 2001: Evolution of low-level rotation in the 29 May 1994 Newcastle–Graham, Texas, storm complex during VORTEX. *Mon. Wea. Rev.,* **129,** 1339–1368.

Zrnić, D. S., and R. J. Doviak, 1975: Velocity spectra of vortices scanned with a pulse-Doppler radar. *J. Appl. Meteor.,* **14,** 1531–1539.

———, and M. Istok, 1980: Wind speeds in two tornadic storms and a tornado, deduced from Doppler spectra. *J. Appl. Meteor.,* **19,** 1405–1415.

———, R. J. Doviak, and D. W. Burgess, 1977: Probing tornadoes with a pulse Doppler radar. *Quart. J. Roy. Meteor. Soc.,* **103,** 707–720.

———, D. W. Burgess, and L. Hennington, 1985: Doppler spectra and estimated windspeed of a violent tornado. *J. Climate Appl. Meteor.,* **24,** 1068–1081.